UNIVERSITA' DEGLI STUDI DI PADOVA

DIPARTIMENTO DI SCIENZE CHIMICHE

CORSO DI LAUREA MAGISTRALE IN CHIMICA

TESI DI LAUREA MAGISTRALE

Synthesis, characterization, and photoremediation properties of copper(I) iodide hybrid materials ($Cu_xI_yL_n$)

Relatore: Prof.ssa Lidia Armelao

Controrelatore: Prof. Mirco Zerbetto

LAUREANDO: Mario Monaco

ANNO ACCADEMICO 2022/2023

Alla mia famiglia

Index

Acronyms and abbreviations

AI	Azure I
AIE	Aggregation induced emission
AIO	All-In-One
BEYE	Blue-excitable yellow-emitting
BHMTA	N-benzylhexamethylenetetramine bromide
CBM	Conduction Band Minimum
CC	Cluster-Centered charge transfer
CCDC	Cambridge Crystallographic Data Centre
CQD	Carbon quantum dot
CuPc	Copper phthalocyanine
DABCO	1,4-diazabicyclo[2.2.2]octane
dpp	1,3-di(4-pyridyl)-propane
deDABCO	N,N′-diethyl-1,4-diazabicyclo[2.2.2] octane
DFT	Density Function Theory
DMP	Dimethyl phthalate
DMSO	Dimethyl sulfoxide
EBT	3-ethyl-1,3-benzothiazole-2-thione
ED	Erioglaucine Disodium salt
EDG	Electron donating group
EWG	Electron withdrawing group
EY	Eosin Y
FWHM	Full width at half maximum
GO	Graphene oxide
HMTA	Hexamethylenetetramine
IQY	Internal Quantum Yield
LBB	Layered bismuth-based
LDH	Layered double hydroxide
LED	Light-Emitting Diode
LMCT	Ligand-to-Metal Charge Transfer

LSC	Luminescent solar concentrator
LUMO	Lowest Unoccupied Molecular Orbital
MB	Methylene Blue
MCWE	Multicomponent white-emitting
MG	Malachite Green
MLCT	Metal-to-Ligand Charge Transfer
MO	Methyl Orange
MOF	Metal Organic Framework
(M + X)LCT	(Metal + Halide)-to-Ligand Charge Transfer
NR	Neutral Red
PCE	Power Conversion Energy
PL	Photoluminescence
PLQE	Photoluminescence Quantum Emission
PLQY	Photoluminescence Quantum Yield
PV	Photovoltaic
REE	Rare-Earth Elements
RhB	Rhodamine B
RISC	Reverse intersystem crossing
sc-XRD	Single-crystal X-ray diffraction
SCWE	Single-component white-emitting
SSL	Solid-State Lighting
TADF	Thermally-activated delayed fluorescence
TC	Tetracycline
TCP	2,4,6-trichlorophenol
Tpp	Triphenylphosphine
TRPL	Time-resolved photoluminescence
VBM	Valence Band Maximum
WLED	White-Light-Emitting Diode
XLCT	Halide-to-Ligand Charge Transfer

Compounds

|	
MM0	0D-$Cu_4I_4(py)_4$
MM1L	(me-DABCO)I
MM2	0D-Cu_4I_6(me-DABCO)$_2$
MM3L	(Bz-HMTA)Cl
MM4	1D-Cu_2I_3(Bz-HMTA) single crystals
MM5L	(2-Nf-DABCO)Br
MM6L	(1-Nf-DABCO)Cl
MM7	1D-Cu_xI_y(Bz-HMTA)$_z$ fine powder
MM8	0D-Cu_3I_4(2-Nf-DABCO)$_2$
MM9	0D-Cu_xI_y(1-Nf-DABCO)$_z$
MM10L	(2-Nf-HMTA)Br
MM11L	(1-Nf-HMTA)Cl
MM12	1D-Cu_xI_y(2-Nf-HMTA)$_z$
MM13	1D-Cu_xI_y(1-Nf-HMTA)$_z$ single crystals
MM14L	(mePy-DABCO)Br
MM16	0D-Cu_xI_y(mePy-DABCO)$_z$
MM19L	(meCaf)I
MM22	[meCaf][CuI_2]
MM23	1D-Cu_xI_y(1-Nf-HMTA)$_z$ single crystals (different solvents)
MM24L	(Pyrn-DABCO)Br
MM25	0D-Cu_xI_y(Pyrn-DABCO)$_z$
MM26L	(Pyrn-HMTA)Br
MM27	1D-Cu_xI_y(Pyrn-HMTA)$_z$
MM28L	(H-DABCO)Br
MM29	[CuI_3(H-DABCO)]K

Chapter 1

Introduction

1.1. Copper(I) iodide hybrid materials

Crystalline inorganic-organic hybrid semiconductors represent an important class of functional materials. They are synthesised by self-assembly of inorganic semiconductor motifs and organic ligands to form crystal structures of various dimensions in the nanometer scale[1,2].

This class of materials has been extensively explored over the past several decades[3,4,5]. They are both fundamentally and technologically important because of their very rich structural chemistry and their interesting, sometimes unique, properties. Conventional inorganic semiconductors are best known for their superior physical properties and chemical robustness; however, they have some major drawbacks such as poor solubility and/or solution processability. On the other hand, organic semiconductors materials offer a simpler device structure, easier fabrication, lower cost, lighter weight, and a greater flexibility; despite these optimal characteristics, they suffer from lower durability and poor power conversion efficiency (PCE). The integration of both inorganic and organic modules in a single crystal lattice enables the combination of the features of inorganic compounds (superior electronic, magnetic, optical, thermal, and mechanical properties) with those of organic molecules (excellent structural flexibility, processability, lightweight, and functionalisability) in the resulting hybrid structures, with greatly enhanced and improved structural, chemical, and physical properties[6,7,8,9,10].

One well-studied class of hybrid semiconductors is hybrid perovskites: alongside the superior electrical, optical, transport properties and structural robustness, they show excellent solubility and solution-processability. However, perovskite-based hybrid materials rely heavily on toxic elements and are generally lack of resistance towards moisture, heat and harsh environment[1]. In order to overcome these issues, a new hybrid material family has been recently developed. These compounds consist of covalently bonded anionic copper(I) halide (CuX, where X = F, Cl, Br, I)

inorganic modules that form coordinative and ionic bonds with cationic organic ligands, designated as All-In-One (AIO) structures. All the AIO-type compounds are constituted of cuprous ions (Cu(I)), with an electronic configuration of (d^{10}): they possess very different properties from those of hybrid cupric halides, in which Cu(II) has the electronic configuration (d^9).
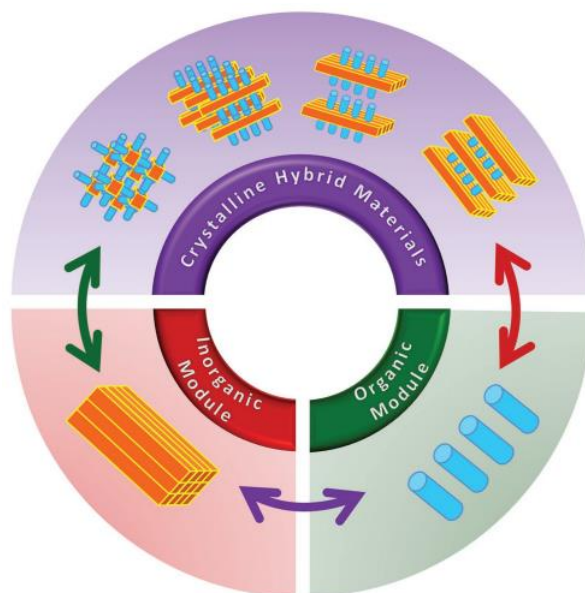
Figure 1.1 *Schematic illustration of the incorporation of inorganic and organic components into single crystal lattice of hybrid structures. Yellow rod: inorganic module; blue cylinder: organic ligand[2].*

The investigation of CuX-based inorganic-organic hybrid semiconductors can be dated back to the 1970s. One of the most studied structures, $0D$-Cu_4I_4pyridine $(py)_4$, was first identified as a cubane tetramer by Raston and White in 1976[11] (Fig. 1.2).
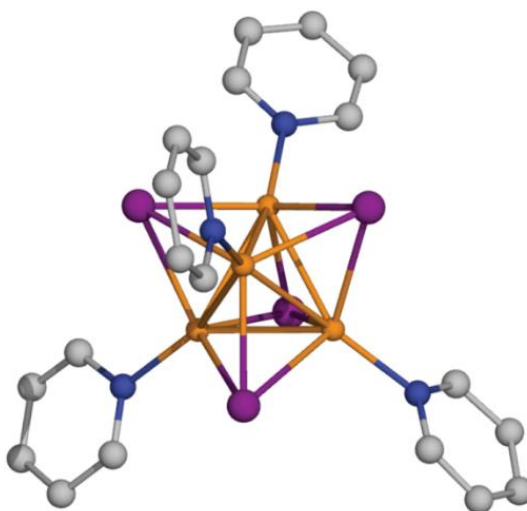
Figure 1.2 *Structure of the $Cu_4I_4py_4$ cluster. Colour scheme: Cu, orange; I, purple; N, blue; C, gray[12].*

Since then, a large number of CuX-based hybrid materials were synthesised, showing different chemical composition and structural types[13,14,15]; over 1000 CuI-based hybrid structures have been reported in the Cambridge Crystallographic Data Centre (CCDC) database.

The vast majority of phosphors currently used in white-light-emitting diodes (WLEDs) are rare-earth elements (REEs) based inorganic materials. Their dependence on these elements (especially europium, terbium, and yttrium) brings to potential cost and supply risks, as well as environmental issues. CuI cluster based hybrid materials belong to the I-VII binary semiconductors class and represent a promising REE-free alternative to common phosphors, due to their earth abundance, low cytotoxicity, structural diversity, and high luminescence efficiency (thanks to the strong spin-orbit coupling in the cluster)[16,17,18,19]. Several other groups of REE-free inorganic phosphors have been reported previously, such as ZnS and CdSe based nanocrystals or quantum dots. Unfortunately, their practical usages are limited by some issues: complicated synthetic procedures, relatively low quantum efficiency, and strong particle size dependence[20,21]. Another possible alternative is constituted by organic phosphors, but efficiency, cost, and stability are the main cons of these systems[22]. The integration of both the inorganic and the organic species into a single crystal lattice has allowed effective combination, modification, and enhancement of good features of the individual components in the resulting hybrid structures. Among the various developed hybrid material classes, one of the most extensively investigated is lead//tin halide based hybrid perovskites. The interactions between the inorganic and the organic species in this class of compounds is essentially ionic, sometimes accompanied by relatively weak hydrogen bonds or van der Waals interactions[23]. Hybrid perovskites exhibits interesting optical properties, which let them be potentially useful for photovoltaics (PVs). Another peculiar new family of crystalline inorganic-organic hybrid materials is based on II-VI binary semiconductors: typically made of inorganic semiconductor nanomodules and N-containing organic ligands, they interact via covalent/coordinate bonds between Group IIB metals (e.g., Zn, Cd) and nitrogen atoms. Different compounds of extended network structures have been obtained by varying the composition and dimensionality of the inorganic component and by using different organic amine molecules. These compounds show very interesting optical absorption and emission properties; moreover, most of them exhibit strong structure-induced quantum confinement due to the perfectly ordered and alternating inorganic and organic motifs at nanometer or subnanometer scale[24].

Despite their intriguing properties, the performances of both perovskite based and II-VI based hybrid materials are not suitable for commercial application. In order to face this issue, a new family of hybrid materials with comparable performance to the commercial phosphors was needed. The solution has been found in crystalline hybrid compounds based on I-VII binary semiconductors

(Group-I elements: Cu, Ag; Group-VII elements: Cl, Br, I). Among them, particularly interesting is copper(I) iodide (CuI). CuI, as well as the other I-VII binary compounds, exists in several structure forms; below 390°C, it adopts a zinc blende structure (γ-CuI). Bulk γ-CuI is the only I-VII binary compound to show a weak photoluminescence (PL) under UV excitation at room temperature (λ_{em} = 420 nm, violet), with an optical bandgap of around 2.9 eV[25]. However, I-VII based hybrid structures can have greatly enhanced optical emission. Such hybrid materials have the general formula $Cu_xI_y(L)_z$, where L is a N, S, or P based organic ligand. The incorporation of CuI inorganic nanomodules and organic ligands in a single crystal lattice can be achieved via covalent/coordinate bonds or ionic bonds, or a combination of the two. This class of hybrid materials shows a great structural variety: the inorganic part can be a discrete molecular cluster (0D), an infinite chain (1D), or a layer (2D) and, by the combination of organic ligands of different types (e.g., aliphatic, aromatic, monodentate, multidentate), crystalline structures of various dimensionalities are obtained, ranging from 0D to 3D.

1.2.   Crystal structure of CuI(L) hybrid materials

As stated previously, CuI(L) hybrid materials have a remarkable structural diversity thanks to the vast variety of available inorganic modules and organic ligands, as well as many possible coordination modes between them. While their crystal structure can be classified by different ways, it is useful to group them based on the nature of chemical bonding. In doing so, 3 subgroups of CuI(L) hybrid materials can be effectively identified: type I structures are those built on dative Cu-N bonds, so both the inorganic CuX module and organic ligands are charge neutral[19]; type II structures are those made of anionic inorganic modules and cationic organic ligands via pure ionic bonds (without direct coordinative bonds between the two)[26]; type III structures are those in which both coordinate and ionic bonds exist between the anionic inorganic module and the cationic organic ligand[1,2,27]. More specifically, type III compounds can be seen as the combination of type I and type II structures and are noted as All-In-One (AIO) structures since all three types of chemical bonds (namely covalent bonds, coordinative bonds, and ionic bonds) coexist in these chemical species (Fig. 1.3). Each subgroup contains materials of different dimensionality (namely 0D, 1D, 2D, and 3D), due to the nature of both the type of bonds and the inorganic and organic components.

4
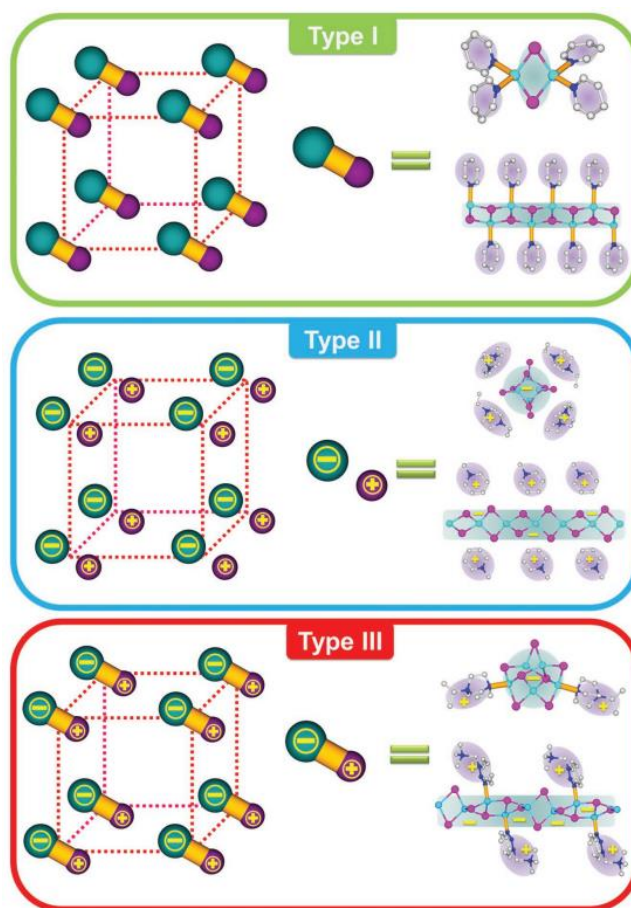
Figure 1.3 *Conceptual representation of Type I, Type II, and Type III (AIO-Type) structures. Colour scheme: green ball: inorganic module; purple ball: organic ligand; yellow rod: coordinative bond. Type I structures are neutral $CuI(L)_n$ species made of Cu-L dative bonds only. Type II structures are ionic $CuI(L)_n$ compounds built upon ionic bonds only. Type III structures are AIO $CuI(L)_n$ species possesing both ionic and dative bonds[2].*

- Type I structures

The Type I structure is the most extensively studied class so far and accounts more than 90% of all the CuI-based hybrid materials. CuI takes various forms, ranging from discrete clusters to 1D extended chains and 2D layers, thus granting an appreciable structural diversity (Fig. 1.4).

There are four modules prevailing among them: CuI monomer (Fig. 1.4a), Cu_2I_2 rhomboid dimer unit (Fig. 1.4b), Cu_4I_4 cubane tetramer ((Fig. 1.4d), and 1D-(CuI) staircase chain. Some other common modules are Cu_3I_3 trimer (Fig. 1.4c), Cu_4I_4 staircase tetramer (Fig. 1.4e), Cu_6I_6 eared cubane hexamer (Fig. 1.4f), 1D-(CuI) split staircase chain (Fig. 1.4g), 1D-(Cu_2I_2) fused staircase chain (Fig. 1.4i), 2D-(CuI) layer (Fig. 1.4j)[2]. In these structures, Cu(I) atoms adopt coordination numbers of three or four: the coordination geometries are trigonal or tetrahedral, respectively[14].

5
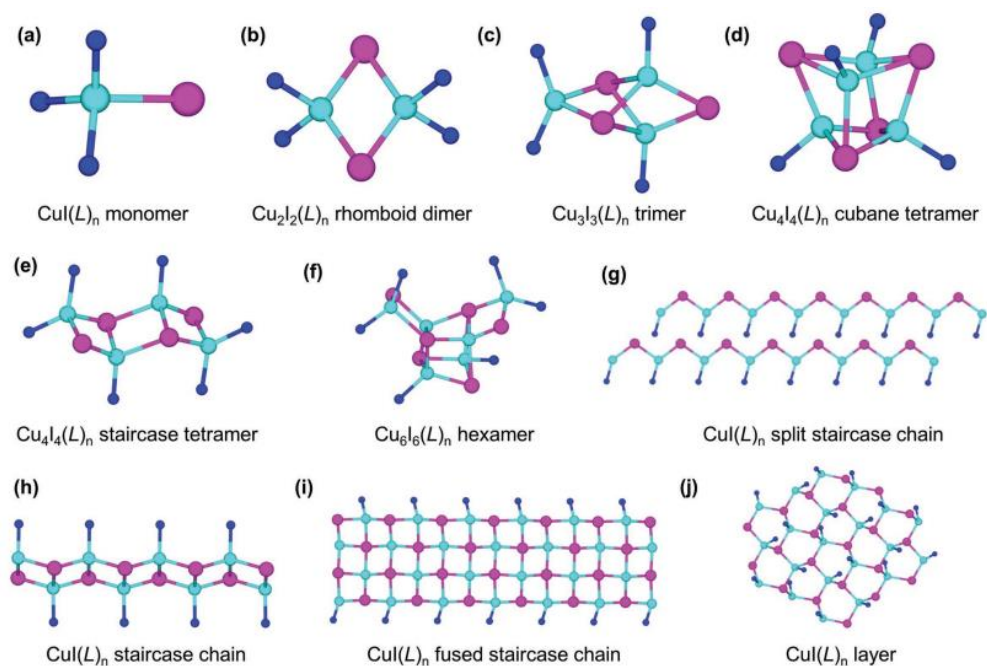
Figure 1.4 a-j) Examples of common inorganic motifs for Type I structures. Colour Scheme: Cu, cyan; I, purple; organic ligands, blue[2].
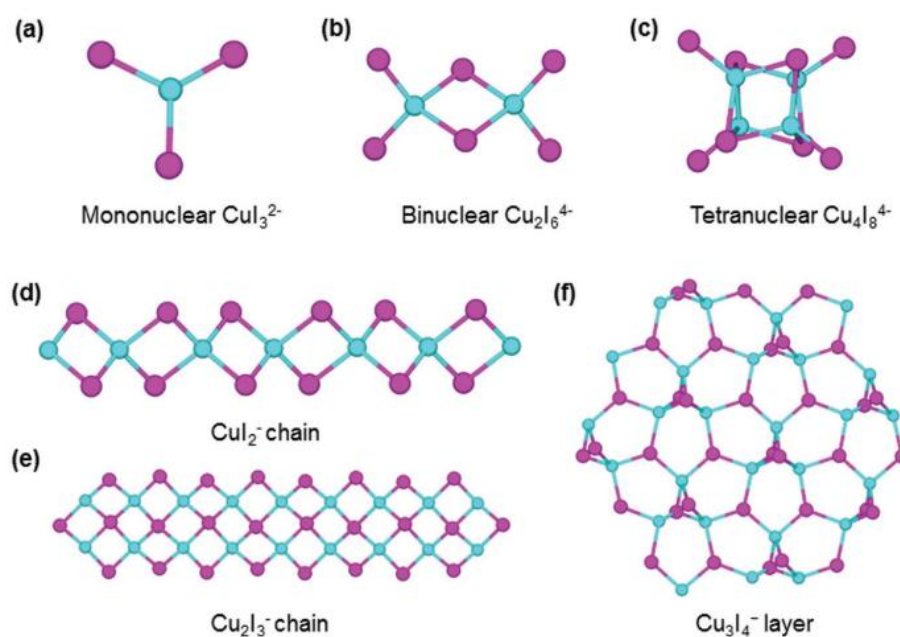
- **Type II structures**

Type II structures are based on ionic pairs (i.e., cationic ligands, anionic $(Cu_xI_{x+n})^{n-}$ modules) held together by electrostatic interactions. From a structural point of view, they resemble hybrid perovskites since there are no direct coordination bonds between the organic and the inorganic components. Type II subgroup is far less large than the type I subgroup; despite that, diverse inorganic motifs are found in these structures, ranging from discrete clusters to extended chains and layers (Fig. 1.5).

In $(Cu_xI_{x+n})^{n-}$ anion clusters, Cu(I) atoms are usually tetrahedrally (or in some cases trigonally) coordinated to I atoms; the most common species of anionic clusters are mononuclear 0D-CuX_3^{2-} (Fig. 1.5a), binuclear 0D-$Cu_2X_6^{2-}$ (Fig. 1.5b), and tetranuclear 0D-$Cu_4I_8^{4-}$. Anionic chain modules show two common structures: 1D-CuI_2^- (Fig. 1.5d) and 1D-$Cu_2I_3^-$ (Fig. 1.5e). Both can be considered as infinite step-laddered chains built on edge-sharing CuI_4 tetrahedra. Few are the known 2D structures constructed on anionic layers: one example is the 2D-$Cu_3I_4^-$ layer, which can be considered as a built of a trimeric Cu_3I_8 unit where each Cu atom is tetrahedrally coordinated to four I atoms[2].

The formation of anionic $(Cu_xI_{x+n})^{n-}$ is often determined by reaction kinetics and organic cationic species[28,29]. The latters are typically obtained via in situ alkylation of N-ligands[30]: due to their

6

charge, size, and shape they have both a structure direction templating and a charge balancing role, thus largely affecting the final structure of the hybrid materials.


Figure 1.5 a-f) Examples of common anionic inorganic motifs for Type II structures. Colour Scheme: Cu, cyan; I, purple[2].

- Type III structures (AIO)

Type III structures are the newer sub-class of CuI-based hybrid materials in which the Cu_xI_y inorganic anionic modules and the cationic organic ligands are connected by Cu-N (or Cu-S, Cu-P) coordination bonds. The inorganic modules can range from 0D discrete molecular clusters to extended 1D chains (Fig. 1.6). The organic ligands can be either aliphatic or aromatic and are designed in order to contain both cationic centres (e.g., quaternary N or P) and free active binding sites for the subsequent coordination to Cu atoms. Such variety of both components, including the fact that a number of anionic inorganic modules have been obtained using similar ligands[31], suggests the potential structural vastity that this class of hybrid materials can achieve.

The first synthesised AIO-type structures were predominantly molecular clusters, ranging from dimeric units (Cu_2) to the hexameric ones (Cu_6) (Fig. 1.6a-g)[31]. Cu atoms can be tetrahedrally coordinated (with iodine atoms or a combination of iodine atoms and ligand molecules) or coordinatively unsaturated, being bonded to only three iodine atoms. This class of materials has a great degree of diversity, also thanks to the presence of isomers and structures with identical inorganic modules coordinated to diverse organic ligands. For what concerns 1D infinite anionic

chain structures, three types have been obtained so far. 1D-$Cu_2I_3^-$ (Fig. 1.6h) shows two kinds of coordination, one being bonded to three I atoms while the other to three I atoms and a ligand. On the other hand, both 1D-$Cu_4I_6^{2-}$ and 1D-$Cu_6I_8^{2-}$ possess tetrahedrally coordinated Cu atoms, either to four iodine atoms or three iodine atoms and one ligand (Fig. 1.6i-j). All tetrahedra in 1D chain structures share an edge[2].
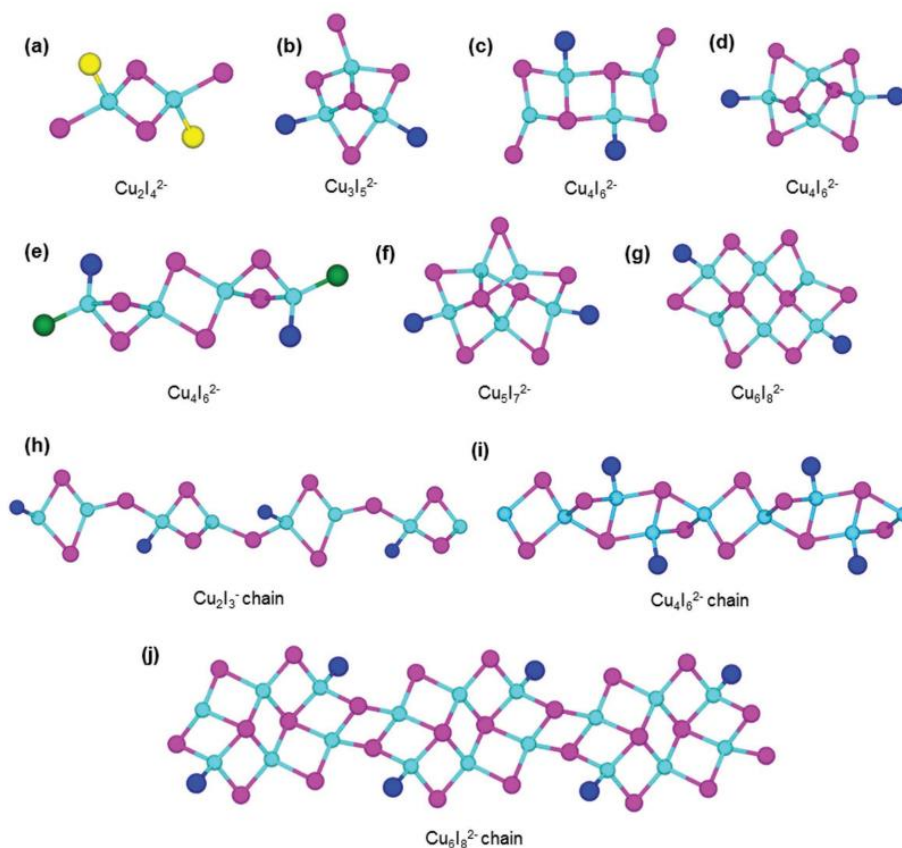
Figure 1.6 a-j) Examples of anionic inorganic motifs for Type III structures. C and H atoms are omitted for clarity. Colour scheme: Cu, cyan; I, purple; N, blue; P, green; S, yellow[2].

Over 30 AIO-type CuX(L) hybrid materials have been obtained so far, ranging from molecular species (zero-dimensional, 0D) to two-dimensional (2D) networks[1]; some of them are reported in Figure 1.7. The first group of these structures were discovered in 2017[31]: seven molecular species based on aliphatic ligands were synthesised, with the Cu-N distances similar to the typical Cu-N bond lengths of type I CuX-based hybrid structures (2.0-2.2 Å)[17,18]. Moreover, these compounds share similar organic ligands: a one-side alkylated triethylenediamine, also known as 1,4-diazabicyclo[2.2.2]octane (DABCO). Another commonly employed organic ligand is hexamethylenetetramine (HMTA), which is able to coordinate to more Cu atoms thanks to the higher number of N atoms in its structure, paving the way to 1D and 2D hybrid materials.

8
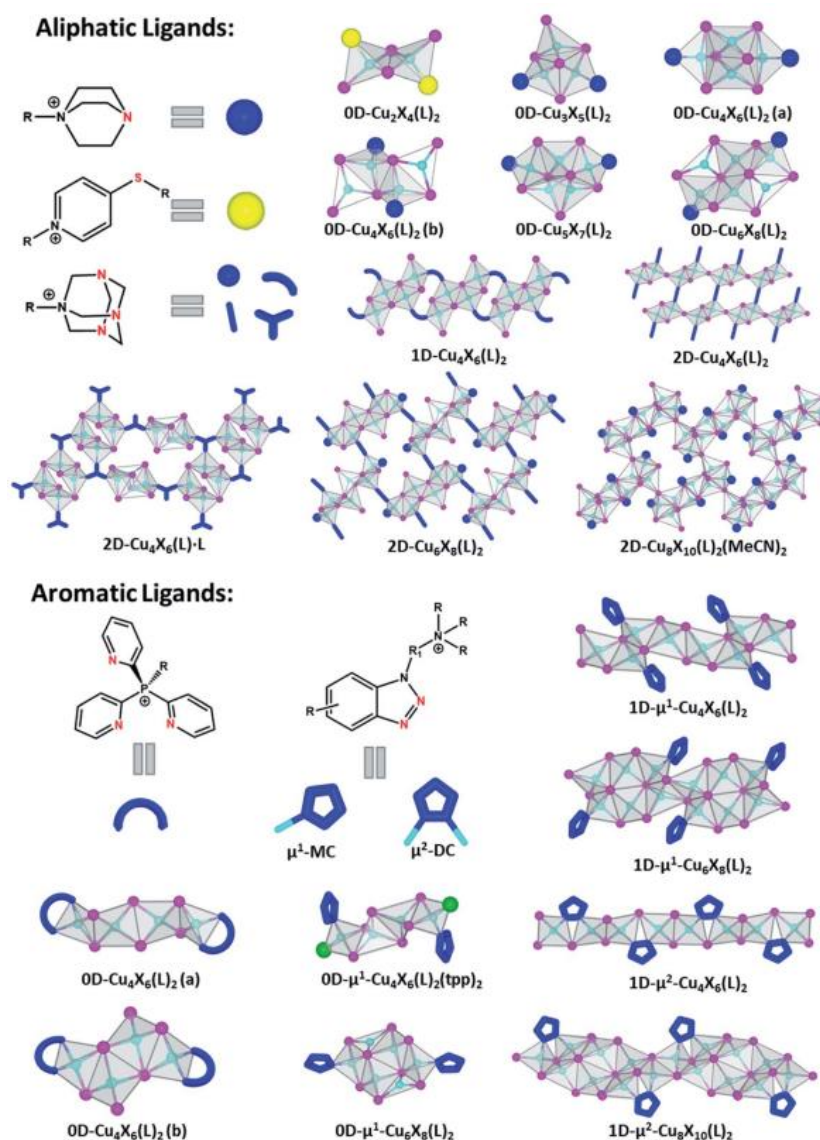
Figure 1.7 Representative structures of AIO-type compounds. Colour scheme: Cu, cyan; X, purple; P, green. Active coordination sites of the ligands (N and S) are marked in red[1].

A more interesting parameter is the Cu···Cu distance: in all aliphatic ligand based AIO compounds, it ranges from 2.56 to 2.72 Å, a shorter distance than twice the Cu vdW radius (2.80 Å)[32]. Such a result suggests the possibility of cuprophilic interactions, which are the main reason for cluster centred (CC) optical emission. In 1D and 2D compounds, the chemical structures and topology are notably influenced by the nature of substituent R groups in the monoalkylated ligands, but Cu-N, Cu-I bond lengths and Cu···Cu distances are similar to those of the 0D AIO molecular structures.

Speaking of aromatic ligands, six AIO-type molecular (0D) species have been reported so far. Three different inorganic CuX modules have been observed: 0D-$Cu_4X_6(L)_2$ (a), 0D- $Cu_4X_6(L)_2$ (b),

and μ^1-0D-$Cu_6X_8(L)_2$ (Fig. 1.7)[31,33]. In all of these 0D-AIO compounds, relatively bulky ligands were employed[1]. An important difference between AIO molecular clusters with aliphatic ligands and those with aromatic ligands are the Cu⋯Cu distances in the inorganic modules: in the latter they are much longer than in the former (3.01-3.36 Å with respect to the already mentioned 2.54-2.72 Å)[1].

In the ligand choice, both the coordinating atom(s)-containing organic molecule and the alkyl substituent play an important role. For example, by using benzotriazole derived cationic ligands, the dimensionality of AIO compounds was successfully expanded from molecular (0D) to infinite chains (1D), resulting in an enhanced framework stability and photoluminescence quantum yield (PLQY). Each ligand has two N atoms that are available to bind with Cu (Fig. 1.8): two different coordination modes are possible, so four different $Cu_xI_{x+2}^{2-}$ anionic chains can be obtained, due to the fact that benzotriazole molecules can adopt a monocoordination mode (μ^1-MC) or a dicoordination mode (μ^2-DC) (Fig. 1.7)[1]. The determining factor for this distinct coordination behaviour was found to be the alkyl chain length of the cationic ligands.
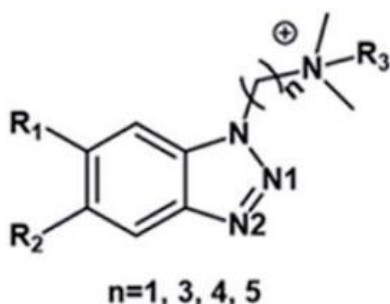
Figure 1.8 Example of benzotriazole derived cationic ligands employed in 1D-AIO compounds synthesis[1].

When the distance between the benzotriazole and ammonium centre is very short, electronic effects prevail over steric ones: the electron density on N1 can be reduced by inductive effect[34], thus inhibiting Cu-N1 coordination and favouring μ^1-MC compounds. In the presence of elongated alkyl chains, instead, steric effects strongly prevail over electronic ones: μ^2-DC are obtained, and the ligand disposition in space has a structural directing effect on the final hybrid materials[35]. Being N1 more affected by NR_4^+ inductive effect than N2, longer Cu-N1 bonds with respect to Cu-N2 bonds are expected: this length difference leads to distorted 1D-Cu_mX_{m+2} chains, resulting in a "zig-zag" form with "cis"-oriented ligands. If the inductive effect is considerably reduced and Cu-N bonds lengths are quite similar, "flattened" inorganic backbones with "trans"-oriented ligands are obtained[1].

10

Moreover, the size of alkyl substituents in the ligands can be determining for the formation of AIO-type compounds. An interesting example is given by a series of triphenylphosphine (tpp) derivative cationic ligands: Pr-tpp, Bu-tpp, and Bn-tpp (Bn = benzyl group) lead to AIO-type compounds, while me-tpp favours the formation of a type II ionic complex[33].

1.3. Chemical and physical properties of CuI(L) hybrid materials

Besides their structural features, CuX-based hybrid materials and in particular the AIO compounds possess really interesting chemical and physical properties.

- Solubility and solution processability

The high-end devices markets are actually dominated by conventional inorganic semiconductors, thanks to their well-known superior physical properties and stability[36,37,38]. Nevertheless, these species show some inherent limitations with respect to stringent material/processing requirements (e.g., high purity, high temperature or high vacuum) and poor solution processability, resulting in a high fabrication cost. In order to face nowadays environmental and energetic problems, solution-processed semiconductors represent a possible new paradigm in optoelectronic device industries[39]. Some techniques for the synthesis of various solution processable semiconductor materials have already been developed, though they are largely limited to pure ionic compounds and some not-so-versatile organic polymers. An alternative is given by colloidal quantum-dots based materials, but their synthesis is usually challenging and expensive[1].

The AIO approach constitutes a different and promising way to obtain solution processable hybrid materials containing covalent/coordinative bonds, including but not limited to CuX-based compounds[27]. While most of type I charge neutral Cu_mI_m structures are totally insoluble in any common solvent, especially those with extended networks[2,19,40], the AIO-type compounds show remarkably high solubility in ordinary polar aprotic solvents, despite they have coordinate networks and are often composed of infinite inorganic modules (Fig. 1.9).
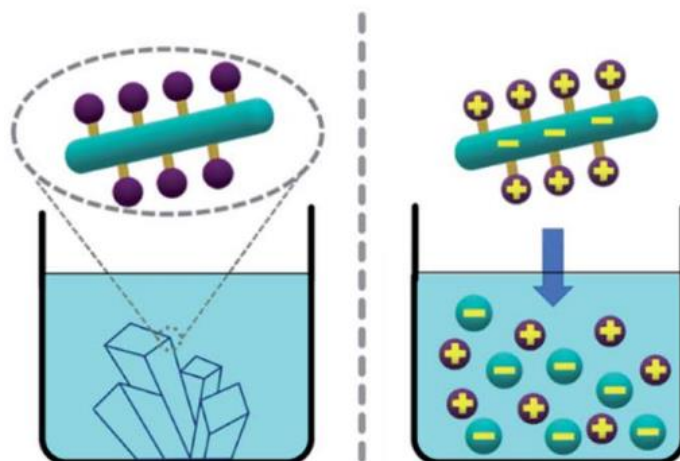
Figure 1.9 Structure similarity and solubility difference of charge-neutral 1D-CuI(L) (left, Insoluble) and 1D-AIO-$(Cu_mX_{m+2})L_2$ (right, soluble) compounds[1].

AIO hybrid materials can be readily dissolved in organic solvents such as DMSO and then be recovered/recrystallized upon addition of antisolvent or by slow cooling of the preheated saturated organic solvent solution. Moreover, the solvation behaviour of AIO-type compounds resulted to be similar to that of hybrid perovskites: all 1D-$(Cu_mX_{m+2})L_2$ compounds show enhanced solubility in organic solvents than CuI and neutral CuI(L) compounds, probably thanks to the complexation of the anionic and cationic fragments[1].

- Chemical and thermal properties

In order to meet the requirement for practical applications, semiconductor materials must possess not only a cost-effective facile synthesis and solution processability, but also high stability towards moisture, light, and heat[26].

An optimal thermal/photo stability is crucial for high performance lighting phosphors, which has been a major obstacle for the vast majority of hybrid phosphors synthesised so far. In the case of Type I CuI(L) species, the instability of the materials is due to the relatively weak Cu-ligand bonds, which breakdown under harsh conditions. Held by both ionic and coordinate bonds between the ligand and the inorganic module, type III (AIO) hybrid materials grant a notably enhanced framework stability compared to those of neutral type I compounds (built only upon coordinate bonds) or hybrid perovskites (exclusively made of ionic bonds).

However, moving towards AIO-type compounds is not the only way to improve CuI(L) hybrid materials stability: there are other two possibilities. The first one is to incorporate the usually

12

strongly emissive inorganic core to build extended networks. Molecular clusters (0D compounds) typically decompose below 100 °C; they are not soluble in water and would quickly decompose in the air. By using them as precursors to construct higher dimensional extended networks through ligand exchange, thermal and photo stability can be greatly enhanced, following the general trend: 0D < 1D < 2D < 3D[31]. The second one is to select organic ligands that form particularly strong Cu-ligand bonds. For example, in Cu_2I_2 dimer based structures including a triphenylphosphine (*tpp*) coligand leads to the formation of stronger Cu-P bonds, while in Cu_4I_4 cubane tetramer based structures employing imidazole derivatives instead of pyridine derivatives results in stronger Cu-N bonds and more robust materials.

On the other hand, the stability of AIO compounds can be further improved too. A first approach is to select multidentate ligands in order to obtain higher connectivity structures, due to chelate effect[41]. A second approach is to build extended networks: the thermal and photo stability enhancements achieved by AIO-type structures follow the same trend as the neutral CuI(L) structures[31]. An example of this feature is given by the greater stability of μ^2-DC structures with respect to μ^1-MC structures, thanks to the higher connectivity in their networks.

All the AIO structures reported so far show good resistance to heat: with just some exception, most of them do not decompose until above about 200 °C; in a few cases, the decomposition temperature exceeds 300 °C. It has also been observed that the thermal stability of AIO compounds with the same inorganic motifs follows the same trend as the binding strength of their Cu-N dative bonds. Moreover, both the aliphatic and aromatic ligand-based AIO hybrid materials exhibit excellent long-term photostability[1].

- Electronic, luminescence, and optical properties

In Solid-State Lighting (SSL) technology, the light-emitting materials must exhibit not only an excellent photo/thermal stability, but also a high luminescence efficiency and, eventually, optical tunability. CuI-based hybrid materials have proved to be a promising REE-free alternative to common inorganic phosphors[13,15,17].

Generally, CuI(L) hybrid materials are strong light absorbers; under ambient conditions, their emissions feature a single broad band, with a full width at half maximum (FWHM) of about 100 nm, and can be tuned in order to cover the entire visible spectrum[1,2]. However, luminescence behaviour in the three structure subgroups is different due to the various emission mechanisms determining the process: Cluster-Centered charge transfer (CC), Metal-to-Ligand Charge Transfer

(MLCT), Halide-to-Ligand Charge Transfer (XLCT), and an overall charge transfer from the inorganic module to the organic ligands ((M+X)LCT). Type I structures show relatively high luminescence Internal Quantum Yields (IQYs) (about 60-90%)[17,18,19]. The presence of covalent bonds between the inorganic and organic components allows MLCT, XLCT, and (M+X)LCT. Type II structures have very poor luminescence: given their ionic nature, neither MLCT nor LMCT (Ligand-to-Metal Charge Transfer) exist; only CC is possible[28,31]. As a combination of type I and type II structures, type III (AIO) structures have high luminescence IQYs (generally exceeding 90%)[2,16] since they can achieve all the aforementioned emission mechanisms.

Cuprophilic interactions play a leading role in determining the emission mechanism. AIO compounds are of paramount importance with regard to the study of the correlation between Cu···Cu distances and optical properties due to their systematic tunability. Short Cu···Cu distances (meaning notable cuprophilic interactions) is essential in granting strong CC transitions[42,43]. On the contrary, when cuprophilic interactions are weak (meaning Cu···Cu distances longer than 2.80 Å, twice the vdW radius of Cu) MLCT and XLCT or (M+X)LCT are observed[17,18,19,27,44]. When Cu···Cu distances are around 2.80 Å, both CC and (M+X)LCT can occur simultaneously and show a responsive dual emission as a function of excitation energy and/or temperature[1,45]. A more intuitive and visual explanation of this phenomenon is given by the qualitative energy diagrams is Figure 1.10.
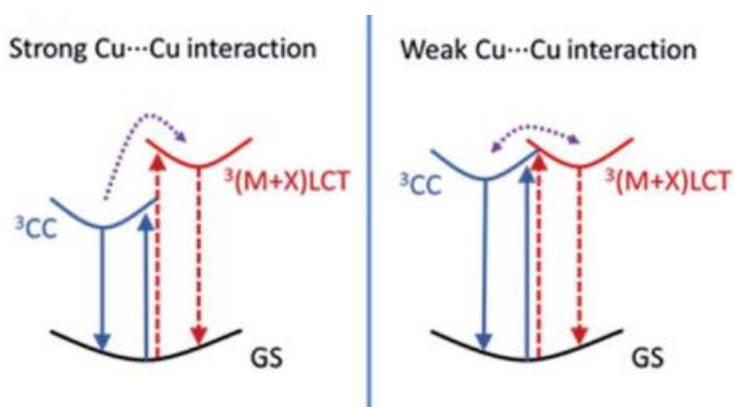
Figure 1.10 Qualitative energy diagrams for the ^{3}CC and ^{3}(M + X)LCT excited states for compounds with strong Cu···Cu interactions (left) and weak Cu···Cu interactions (right). GS, ground state. CC, cluster-centred charge transfer. (M + X)LCT, (metal + halogen)-to-ligand charge transfer[45].

Generally, AIO compounds made of aliphatic ligands have shorter Cu···Cu distances than those built upon aromatic ligands, thus showing pure CC emission mechanism: the emission energies in this case are mainly determined by the inorganic cores; the effect of the ligands is negligible. All

14

the 0D-AIO structures made of aliphatic ligands reported so far follow the CC emission mechanism[1]. Another important parameter is the structural rigidity. When CuX-based hybrid materials are promoted to the CC excited state, a decrease in Cu···Cu distances may occur[46]: the more flexible the structure, the more enhanced the CC emission is, due to the better accommodation of the associated structure change. So, rigid frameworks tend to diminish such changes, leading to worst luminescent hybrid materials. In aliphatic ligand based AIO extended networks, both CC and (M + X)LCT are possible, as confirmed by calculations: the conduction band minimum (CBM) is composed by either inorganic and organic modules molecular orbitals[45]. Anyway, one or both processes play a dominating role depending on Cu···Cu distances and structural rigidity; as an example, structures with short Cu···Cu distances and high flexibility show a comparable emission from both pathways.

AIO-type compounds built upon aromatic ligands usually have longer Cu···Cu distances, so their main emission mechanism is (M + X)LCT. The CBM of these hybrid materials is populated mainly by the ligands lowest unoccupied molecular orbitals (LUMO), as confirmed by spectroscopic studies: their bandgaps are generally in trend with the calculated LUMO energies[2]. Hence, by adding electron withdrawing group (EWG) or electron donating group (EDG) to the ligand, the original LUMO can be stabilized or destabilized: the alteration of its energy level results in a modification of the hybrid material bandgap.

A more detailed analysis on the AIO-type structures exhibiting chromism behaviour via temperature- and excitation-dependent solid state photoluminescence spectroscopy suggests that ^{3}CC and ^{3}(M+X)LCT could be poorly coupled, and higher energy is required to populate the higher laying state (Fig. 1.10). Density Function Theory (DFT) calculations showed that the valence band maximum (VBM) of the copper iodide AIO compounds is essentially constituted by the inorganic atomic states, specifically Cu 3d and I 5p orbitals, and the CBM is populated either by organic components (i.e., C and N 2p orbitals) or a combination of organic and inorganic components. In the latter case, a small energy difference was noticed between their energy levels, suggesting the poor coupling of the two excitation states[1]. Therefore, the relative intensity of higher laying state based emission can be tuned by varying temperature or excitation wavelength (i.e., the energy applied to the process), resulting in responsive dual emitters materials towards temperature and excitation energy[45].

Thermochromism is an effective experimental feature in order to study the emission mechanisms of AIO hybrid materials. Thermochromic behaviour is typical of AIO compounds that undergo CC emission mechanism, especially in those with a high degree of structural rigidity at lower

temperatures: a reduced structural torsion brings to a better localization of states, so the blue shift in the emission energy is accompanied by a peak width narrowing[31]. On the other hand, the excited state of AIO compounds following the (M+X)LCT emission mechanism leaves the structure relatively unperturbed[47], leading to little or no thermochromism on these class of hybrid materials.

Other differences between the two emission pathways emerge from time-resolved photoluminescence (TRPL). In AIO compounds following CC emission (Fig. 1.11a), the PL lifetimes show very little temperature dependence and are best fit with a single (first-order) exponential decay function, with average values are typically several microseconds (μs): the emission is then attributed to phosphorescence, arising from spontaneous radiative decay from the lowest excited triplet state (T_1) to the ground state (S_0). In AIO compounds exhibiting (M+X)LCT emission (Fig. 1.11b), the PL lifetimes show very strong temperature dependence and can be best fit by a double exponential decay functions, thus suggesting their emission arise from two different processes with comparable contributions: phosphorescence, with average values of several μs, and thermally activated delayed fluorescence (TADF), with average values of tenth of a μs. The latter process is due to the small energy barrier between the lowest excited singlet state (S_1) and T_1, so that a fraction of electrons can undergo reverse intersystem crossing (RISC) from T_1 to S_1 and then follow radiative recombination from S_1 to S_0[1].
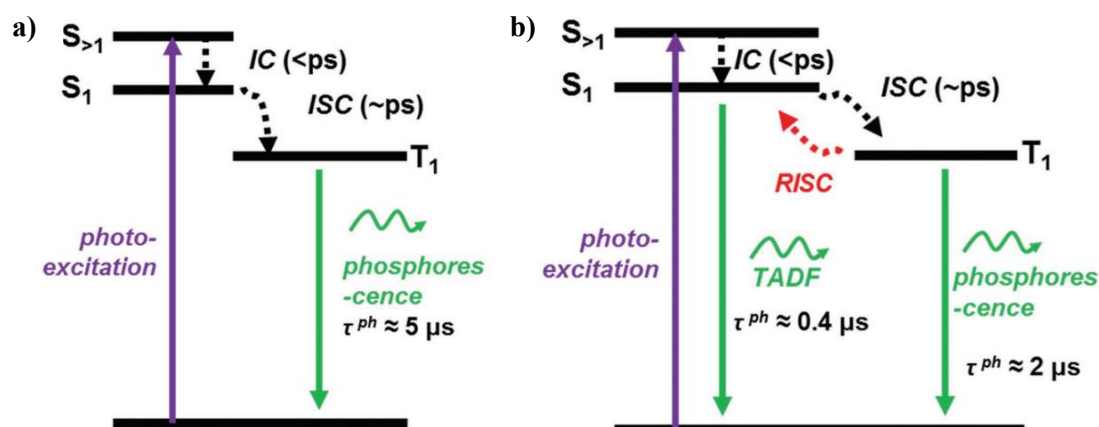
Figure 1.11 *Energy diagrams of a) CC emitting compounds, indicating phosphorescence, and b) (M+ X)LCT emitting compounds, indicating TADF and phosphorescence emission processes[1].*

Moreover, very different IQYs are observed between μ^1-MC and μ^2-DC, despite their similar emission energies and PL mechanism. Compared to the μ^1-MC structures, the μ^2-DC structures

possess much stronger binding strength and significantly reduced ligand rotation and vibration: these features lead to an effectively suppressed nonradiative decay and higher IQYs[27].

1.4. General synthetic approaches

The synthesis of CuI-based hybrid materials is generally ligand templated and, in most cases, by one-pot solution process at different temperatures. Copper and iodide ions are very labile, so that different inorganic modules might form. These inorganic cores can be affected by reaction conditions and ligand choice: the resulting hybrid product can vary depending on the structure and the amount of organic ligands employed in the synthetic procedure. The synthesis of CuI-based hybrid materials is influenced by a large number of factors, including starting materials, solvents, reaction time, temperature, and pressure[2]. More specifically, reaction time is crucial for achieving kinetic phases, while temperature is fundamental for the synthesis of thermodynamically stable phases; depending on the solvent choice, different products may be interconverted one into the other.

Different synthetic routes can be followed in order to obtain type I, type II, or type III structures. Type I and type III (AIO) structures are usually synthesised by reactions of Cu(I) salts and ligands in solution at room temperature. A common method to obtain thermodynamically stable phases that would form at higher temperatures is solvothermal reaction[48,49]. For what concerns type II structures, solvothermal reactions is the main synthetic pathway to obtain them; cationic organic species are usually formed through in situ alkylation of the solvents (e.g., alcohols) with N-ligands[14,50]. The choice of a determined synthetic pathway is also influenced by the crystallinity degree required for the resulting hybrid material.

- **Ligands design, synthesis, and effects**

Being an integral part of the resulting materials, ligand choice, modification and effects have to be taken into account, especially depending on the desired type of structure.

Most of the neutral N-ligands in type I structures are pyridine, pyrazine, or imidazole derivatives. A useful approach for the synthesis and functionalization of these ligands is the reaction of the starting organic molecules (e.g., imidazole) with alkyl halides (Fig. 1.12a)[17].

The organic N-ligands in type II structures are generally synthesised in situ under solvothermal conditions in acidic environment, in order to obtain positively charged cationic species. Alkylation occurs on all N atoms possessing lone pair electrons, so that coordination towards Cu atoms is not possible, and only ionic bonds with the inorganic modules would form (Fig. 1.12b)[29]. Appropriate solvents for these reactions are alcohols because they function as both the solvent and the alkylating agent.

In type III (AIO) structures, specifically designed cationic ligands are needed. They must have either alkylated and free N (or S) atoms: the formers are necessary to give to the resulting material its ionic character, while the latters enable their direct coordination to Cu atoms via coordinate bonds[31]. There are three types of reactions (I, II, and III) for the synthesis of this class of ligands (Fig. 1.12c). In reaction I, one of the tertiary N atoms of a bidentate N-ligand is alkylated, leaving the other one as a binding site for the Cu atoms. In reaction II, the aromatic N is alkylated while S atom functions as the binding site for Cu. The alkylation of the organic ligands in reaction III is a two-step process: only the NH site of an N-heterocyclic ring is attacked by the alkylating reagent, leaving the aromatic N atom available for binding to Cu atoms[2].
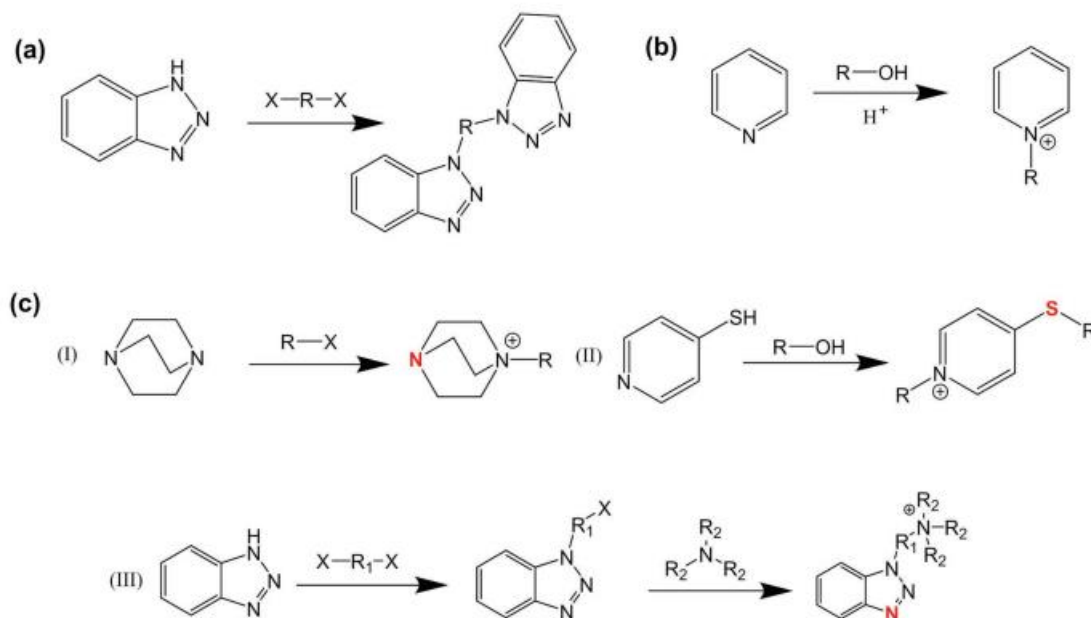

Figure 1.12 Synthetic approaches for the preparation of organic ligands for a) Type I, b) Type II, and c) Type III structures. The free binding sites in cationic ligands are marked in red[2].

Moreover, Cu:L ratio plays a significant role in the formation of hybrid structures with specific stoichiometries. By varying the amount of ligand used with respect to the Cu quantity, different hybrid structures may be generated.

- Slow diffusion method

Slow diffusion method is an extremely useful approach for single crystal growth of CuI-based hybrid structures at room temperature. The inorganic and organic reactants are dissolved in two different solvents and then loaded in a reaction container as two distinct layers, usually separated by a third solvent (Fig. 1.13). The latter acts as a buffer layer between the inorganic and the organic layers: the slow and controlled diffusion of the reactants into the intermediate phase hinders the nucleation process while favouring the single crystal growth of the already formed hybrid material nuclei. When needed, the vials are kept slightly open to let the solvents to evaporate slowly, thus favouring the precipitation of the desired product.
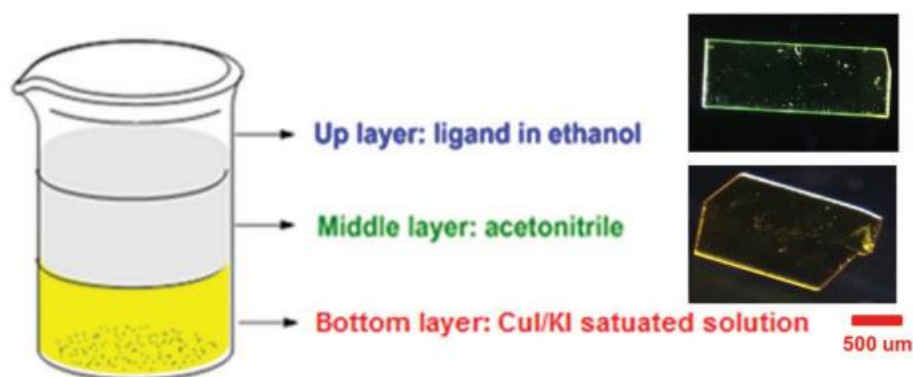
Figure 1.13 *Left. Illustration of slow diffusion process. Right: single crystals of 2D-CuI(pm)0.5 (top) and 2D-CuI(pz)0.5 (bottom) obtained by slow diffusion[2,19,51].*

Common solvents used in slow diffusion method are: an aqueous solution saturated in KI for CuI, acetonitrile for the interphase, ethanol for the organic ligands: this means the inorganic species diffuse from the bottom layer while the ligand penetrate slowly from the top layer into the middle one. To grant an efficient synthesis of the desired material, solvents density and miscibility have to be taken in account. As an example, for certain types of structures, the direct mixing of CuI in

saturated solution with the organic ligand only results in powder formation, thanks to the fast reaction rate.

A major drawback of this method is that it is limited to products obtainable at room temperature.

- **Precursor approach**

A problem in conventional reactions involving CuI/KI solutions with the organic ligand is the possibility to obtain distinct phases that are difficult to separate: so, the targeted compound is not always isolable. A way to achieve a single-phase product is a bottom-up process called precursor approach: the desired Cu_mI_m core is pre-synthesised in the form of a molecular cluster, which is then used as a precursor to form hybrid structures by simple ligand exchange. The presynthesised molecular clusters is employed as the reagent instead of CuI and its molecular identity and structure are retained in the final products (Fig. 1.14).
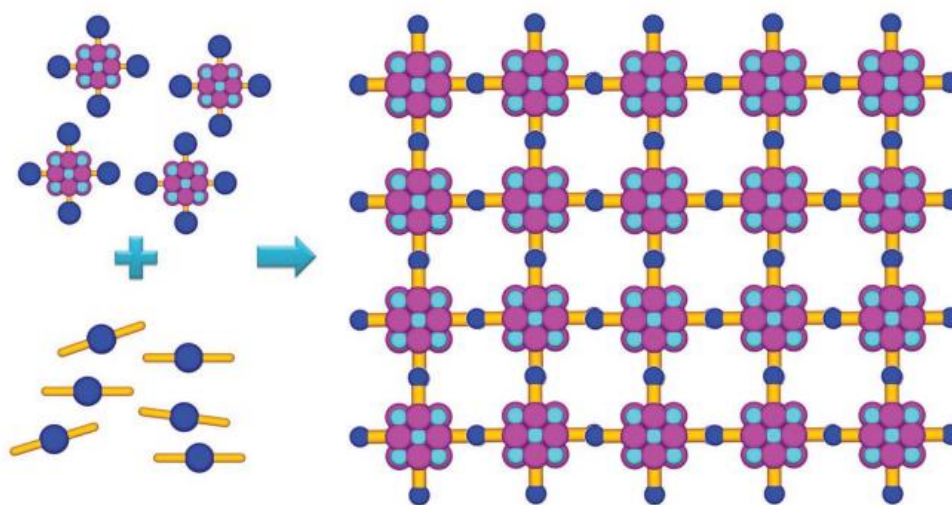

Figure 1.14 *Schematic representation of precursor approach for the synthesis of extended structures. Colour scheme: Cu, cyan; I, purple; organic N-ligand, blue; coordination bond, yellow rod[2].*

Precursor approach has some important pros: it preserves the targeted inorganic motifs and their optical properties, it enhances framework stability by generating various extended network structures, and it ensures a high purity of the final product by eliminating the impurity phases. The main con is the necessity to synthesise the adequate precursor molecular cluster.

20

- **Mechanochemical synthesis**

A third approach, more followed in industrial synthetic processes rather than in laboratory procedures, is mechanochemical synthesis. This method has several advantages (high reaction yields, low pollution, shorter reaction times), as well as different synthetic pathways (manual grinding and ball milling) (Fig. 1.15). Such a technique is greener and low cost with respect to other methods, but also really energy efficient: it represents a valid choice in large scale preparation of various materials (e.g., phosphors)[52].
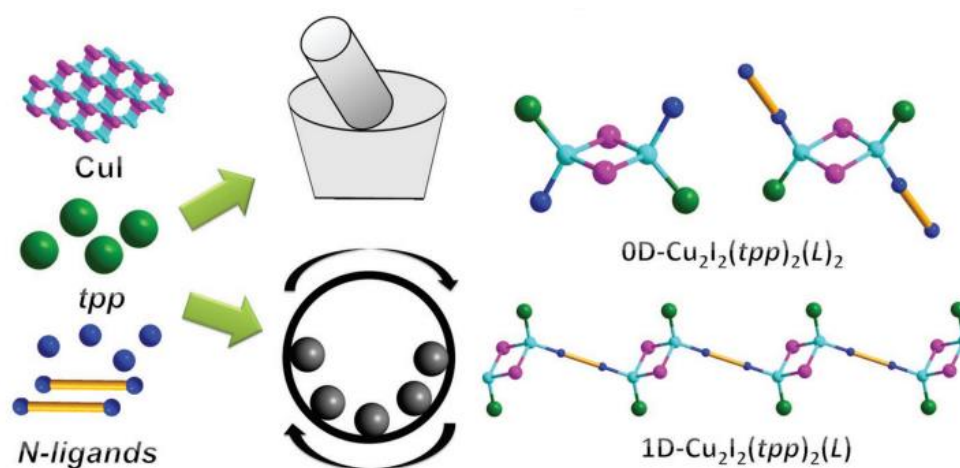
Figure 1.15 *Illustration of synthesis by mechanochemical approaches, including manual grinding (top) and ball milling (bottom). Colour scheme: Cu, cyan; I, purple; organic N-ligand, blue; coordination bond, yellow rod*[2].

The main problem arising with this method is the difficulty in isolating targeted phases, as diverse types of structures are produced simultaneously by simple grinding. Moreover, washing and separation procedures are usually needed to remove unreacted starting materials, resulting in the use of additional solvent and a lowering of the final products yields[53]. For these reasons, mechanochemical synthesis has not been well established for CuI-based hybrid materials yet.

A way to address these issues is by adopting a rational choice of ligands, stoichiometric ratios, and physical forms of the reagents in order to favour the formation of single-phase products. For example, a stoichiometric addition of a liquid form ligand can allow the complete conversion of the solid starting materials into the phase-pure product; any excess can simply evaporate, leaving the system without the need of purification procedures[2,54].

- Other synthetic routes

As already mentioned, CuI-based hybrid materials can be obtained following other synthetic routes. Direct mixing of the inorganic and organic reactants usually brings to powder products: this method is very simple and is useful when crystalline phases are not needed. Solvothermal reactions are good to synthesise thermodynamic products; it is a largely diffuse technique in the synthesis of type II structures.

Another interesting procedure is microemulsion synthesis. This technique is particularly relevant when the desired product needs to be in form of nanoparticles, such as in the case of aggregation-induced emission (AIE) inks. The microemulsion approach can be employed for the direct synthesis of hybrid materials or in combination with other methods, namely the precursor approach[16,55].

In the first case, a long chain polymer generating micelles in solution is able to solubilize and confine CuI units, forming a stable dispersion due to steric hindrance. At this point, the cationic organic ligand is added to the solution: it diffuses into the micelle and react with CuI, generating confined crystalline nanoparticles of the targeted product (Fig. 1.16)[16].
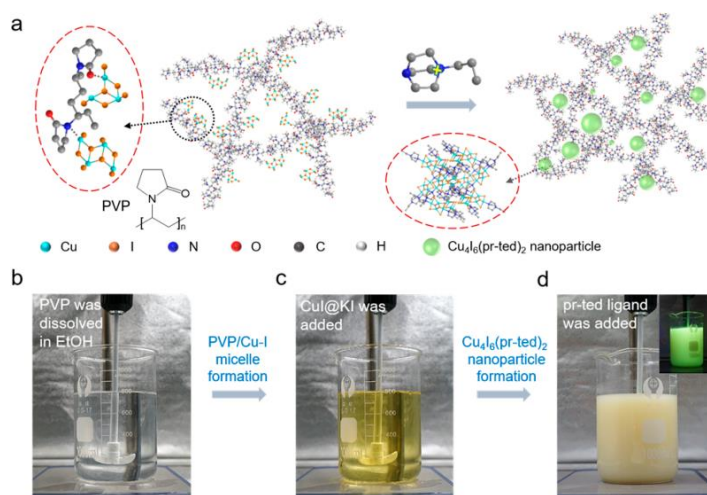
Figure 1.16 a) Schematic representation of polyvinylpyrrolidone (PVP) stabilized coordination process of CuI inorganic units and cationic ligands for the formation of luminescent nanocrystals. b) A colourless clear solution formed by dissolving PVP in the ethanol. c) A pale yellow clear solution of saturated solution of CuI added into the previously prepared solution. d) A white colloidal nanoparticle suspension obtained after the addition of the propyl-triethylenediamine (pr-ted) to the CuI precursor solution. Inset: photograph of the resulting colloidal nanoparticle suspension under the irradiation of ultraviolet light (365 nm)[16].

In the second case, a pre-synthesised hybrid molecular cluster is used as the initial building block, due to its greater stability with respect to other Cu_mI_m-based cluster species. The cluster is dissolved with the desired organic ligand and a ligand exchange occurs. The targeted compound is obtained

as a powder: by confining it into micelles, its mobility is restricted, and the aggregation of the hybrid clusters is favoured; the subsequent demulsification process grants the possibility to isolate the obtained nanoparticles (Fig. 1.17)[55].
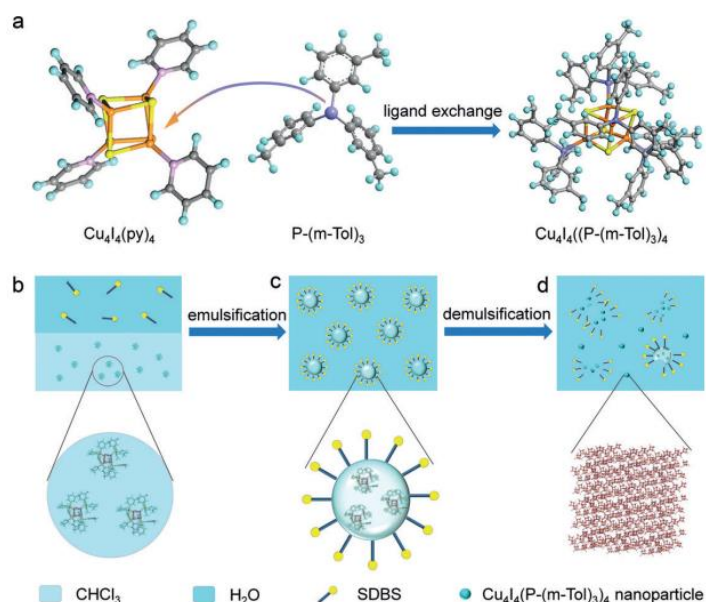
Figure 1.17 a) Schematic illustration of the synthesis of $Cu_4I_4(P$-$(m$-$Tol)_3)_4$ from the precursor $Cu_4I_4(py)_4$. Colour scheme: Cu, orange; I, yellow; N, purple; C, gray; H, light blue; P, dark purple. b) Sodium dodecyl benzene sulfonate (SDBS) dissolved in aqueous phase (top) and $Cu_4I_4(P$-$(m$-$Tol)_3)_4$ powder dissolved in $CHCl_3$ phase (bottom). c) $Cu_4I_4(P$-$(m$-$Tol)_3)_4$ emulsion formed from the mixed two phases under stirring and ultrasonication. d) Demulsification process to obtain $Cu_4I_4(P$-$(m$-$Tol)_3)_4$ AIE nanoparticles[55].

1.5. Applications of AIO hybrid materials

The main applications of CuI-based hybrid materials rely on the optical properties of these compounds, as well as their optical tunability.

- Lighting phosphors for LEDs

In solid-state lighting (SSL), light-emitting diodes (LEDs) are used to convert electricity into light. Current white LED (WLED) technologies are predominantly phosphor-converted WLEDs (pc-WLEDs). They can be assembled in two ways: by coating a blue LED chip with yellow or a multicomponent phosphors; by coating a UV LED chip with white or multicomponent phosphors[2,56,57]. The phosphors in pc-WLED type must be blue excitable, and the white phosphor has to show a balanced emission over the entire visible spectrum (400-700 nm)[2]. However, the vast

majority of commercial pc-WLED phosphors relies on rare-earth elements (REEs), which face not only environmental issues but also potential supply and cost risks[58].

AIO compounds constitute a suitable candidate as alternative phosphors for clean energy lighting devices, due to their: high solubility and dispersibility, excellent quantum yield, robustness towards moisture and heat, well tunable emission energy, and low cost and easily scalable synthesis. So, by taking into account the great features of these hybrid materials, different types of phosphors have been assembled (Fig. 1.18)[2].

Single component blue-excitable yellow-emitting (BEYE) phosphors are excited by a blue-emitting LED chip (≈ 450 nm); their optical bandgap is lower than ≈ 2.6 eV. The operating emission mechanism is MLCT. 1D-CuI(L) staircase chain based structures and AIO structures with aromatic ligands are representative of BEYE phosphors[2].

Single component white-emitting (SCWE) phosphors emit over the entire visible light region. They are generally composed of CuI(L) hybrid materials doped with a second organic ligand, resulting in a broader and well balanced white emission[2].

Multicomponent white-emitting (MCWE) phosphors are obtained by physically mixing two phosphors with complementary colour emission to generate white light. The light quality of MCWE phosphors can be tuned by varying the ratio of the two hybrid materials. Commonly employed AIO structures are Cu_2I_2 dimer and Cu_4I_4 cubane based compounds[2].


Figure 1.18 Illuminating LED light bulbs (110 V, 2W) coated by selected AIO-type phosphors[31].

24

- **Luminescent solar concentrators**

Luminescent solar concentrators are devices used to provide higher optical concentration to solar cells to increase their electrical power: they do so by collecting radiation, converting it to luminescence, and directing the generated radiation into an output target. In conventional solar concentrators, large mirrors track the Sun and yield high optical intensities on solar cells at the focal point[1]. Some issues of these devices are the undesired heating effect on the solar cells, and the costs of deploying and maintainance[59]. On the other hand, luminescent solar concentrators (LSCs) are able to grant a high optical concentration without generating excess heat.

LSCs are built by dispersing a luminescent material in a highly transparent waveguide substrate, with the solar cells at its sides. The physical processes in LSCs are quite simple: at first, the sunlight is absorbed by the luminescent material; then, it is reemitted and directed to the solar cells at the sides by internal reflection thanks to the waveguide effect (Fig. 1.19)[1,60].
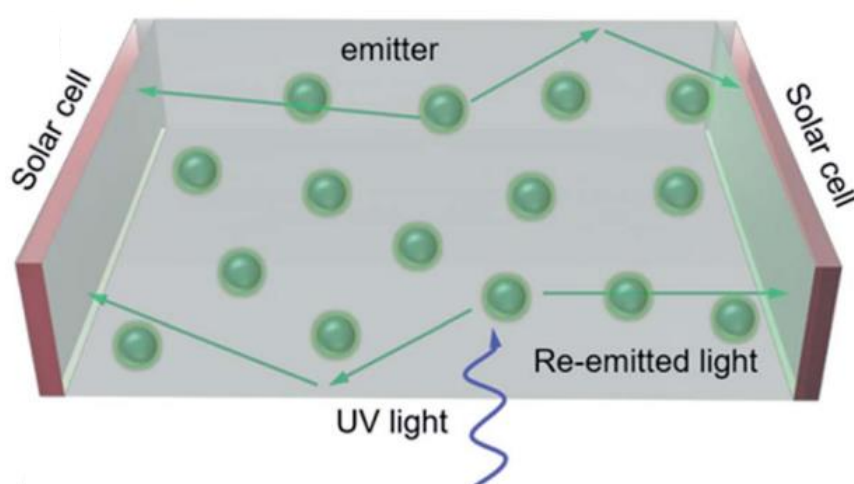
Figure 1.19 Schematic representation of an LSC device. Green balls indicate the luminescent material nanoparticles[1].

One of the greatest limitations of LSCs is the significant luminescence reabsorption loss[61]. AIO hybrid compounds constitute an effective material choice to address this issue. Due to their lower extinction coefficients, CuI(L)-based structures are better suited in LSCs with respect to common perovskites, such as $CsPbBr_3$[1]. Moreover, they possess unique properties, such as: high PLQYs, appreciable Stokes shifts, excellent solution-processability, and a strong absorption in the UV region[1].

- **Luminescent inks**

Environmental-friendly and highly luminescent inks are in diverse demand for a series of applications including art paintings, anticounterfeiting printings, and functional coatings[16]. A conspicuous number of luminescent inks has already been synthesised, ranging from organic dyes to rare-earth doped compounds[62-65]. However, these materials suffer of various problems, including difficult synthetic processes, high cost and environmental issues (e.g., REEs), photo bleaching and low photoluminescence quantum efficiency (PLQE) (e.g., carbon dots)[16].

An alternative phosphors class is that of CuI-based hybrid materials: they are earth abundant, possess a notable structural diversity, have high luminescence efficiencies, and manifest low cytotoxicity. Moreover, AIO-type structures are particularly suitable for this kind of applications due to their enhanced structural stability and efficient luminescence.

Figure 1.20 A picture painted by the $Cu_4I_6(pr-ted)_2$/PVP ink under natural light (left) and 365 nm ultraviolet light (right)[16].

A good example of AIO compounds suitable to be used in inks is $Cu_4I_6(pr-ted)_2$ (pr-ted = propyl-triethylenediamine), obtained in form of nanoparticles by microemulsion approach (Fig.1.20). These nanoparticles show a very strong absorption to the light with a wavelength lower than 400 nm, a wide Stokes shift (the emission peak is centred at 526 nm), and a very high PLQE (98.6%)[16].

- **Photodegradation of organic pollutants**

The progress of science and technology have improved people's living standards alongside with the development of serious environmental problems, especially water pollution. In order to face these issues, an environmental purification strategy is seriously needed. One of the possible answers has been found in photocatalytic degradation of pollutants via hybrid materials. Different kinds of materials have been studied so far: among them, there are graphene oxide (GO)-TiO₂ nanomaterials[66,67,68], semiconductors based on Cd[69,70], and layered bismuth-based (LBB) semiconductors[71]. Despite their intriguing properties, these materials suffer from major drawbacks such as nanoparticles agglomeration, use of REEs, not scalable synthetic procedures, or rapid recombination of photogenerated carriers in the bulk.

Being low toxic, based on earth abundant elements, highly stable, easily processable and possessing excellent IQYs, AIO hybrid materials represent a promising class of environmental-friendly photocatalysts. They do not show many of the aforementioned issues, can be easily synthesised and tuned in order to match the needed features for specific pollutants degradation. Several copper-containing photocatalysts have been developed and studied so far, either with Cu as the only metal and in combination with other elements[50,72-77].

For what concerns CuI-based hybrid materials, a considerable number of photocatalysts can be obtained due to the great variety of both the inorganic clusters and the coordinating ligands. [Cu₄I₄(EBT)₅] (EBT = 3-ethyl-1,3-benzothiazole-2-thione) (UJN-Cu) is a promising tetranuclear copper(I) iodine cluster with excellent water stability and enhanced visible light absorption, as well as better organic dye photodegradation capabilities than nitrogen-doped TiO₂ under visible-light irradiation[75]. UJN-Cu solves two major problems of CuI as a p-type semiconductor: the lowering of the band gap from 3.1 eV to 2.58 eV, so that the material can absorb the visible light to photocatalyse the reaction; the decrease in electron-hole recombination, which previously hindered the efficient transfer of photogenerated electrons to the photocatalyst surface[75]. UJN-Cu efficiency as catalyst was evaluated with the photodegradation of RhB: after 100 minutes of irradiation, up to 86% of the organic dye was degraded. The performance of UJN-Cu was far superior to that of N-TiO₂, for which the degradation rate was only 48%. Moreover, is also promising for its recyclability: after four runs, no significant decrease in photoactivity has been observed[75]. A second example of CuI-based organic-inorganic hybrid material is {[BHMTA][Cu₂I₃]}ₙ (BHMTA = N-benzylhexamethylenetetramine bromide), employed in the degradation of tetracycline (TC): after 220 minutes under visible light irradiation, the degradation rate of TC in the presence of the photocatalyst was 96.6%[76]. This photocatalyst has also the best performances under very mild conditions (pH = 7, T = 35°C) and showed a slightly decrease of 6.0% in its degradation efficiency after three consecutive cycles[76]. (deDABCO)₂(meDABCO)Cu₁₁I₁₇ (deDABCO = N,N′-diethyl-

1,4-diazabicyclo[2.2.2] octane; meDABCO = N-methyl-N′-ethyl-1,4-diazabicyclo[2.2.2]octane) can be solvothermally synthesised as two different polymorphs by varying the working conditions[50]. Both of them have absorption response to UV light (bandgaps of 3.2 and 3.1 eV, respectively) and follow a ^{3}CC charge transfer mechanism. The two isomers possess a high UV-light-driven photocatalytic efficiency: the first application for this feature has been the photocatalytic degradation of a series of dyes (Methylene Blue, MB; Neutral Red, NR; Erioglaucine Disodium salt, ED; Azure I, AI; Methyl Orange, MO; Malachite Green, MG; Eosin Y, EY). The performances of the two isomers were nearly the same in the case of MB and NR (the ratio of degradation was about 97%) while with other dyes, such as ED, the second polymorph was definitely more efficient (the degradation rate for the first isomer was 32%, for the second one was 85%); anyway, the degraded rate became almost similar after prolonged irradiation[50]. To prove the versatility of these compounds, the first isomer was put in a purple solution obtained by mixing an ED solution (light-blue) and a NR solution (light-red). After only 30 minutes of light irradiation, the solution turned light blue and essentially came to the colour of the residual ED, thus demonstrating the high selectivity of the photocatalyst[50]. Another example is given by di-pyridyl propyl hybrid cuprous halogenides, obtained by solvothermal reaction of 1,3-di(4-pyridyl)-propane (dpp) and CuI/CuBr[77]: dpp acted as template or structure-directing agent and the different products were synthesised by varying reagents stoichiometric ratios, solutions, or reaction conditions. $[H_2dpp]_2Cu_{11}I_{15}$ and $[H_2dpp]_2Cu_{11}Br_{15}$, with a respective bandgap of 1.48 eV and 2.21 eV, were employed for the photodegradation of Rhodamine B (RhB) under visible light irradiation. With $[H_2dpp]_2Cu_{11}I_{15}$, the degradation ratio of RhB reached 90% after 180 minutes and nearly 100% after 200 minutes of irradiation; on the other hand, $[H_2dpp]_2Cu_{11}Br_{15}$ showed a much faster photodegradation speed, decomposing about 98% of RhB after 30 minutes irradiation[77]. Further experiments on $[H_2dpp]_2Cu_{11}I_{15}$ also revealed almost no loss of its photodecomposition rates and efficiency after three cycles, underlying its photostability[77].

1.6.   Research work structure and goals

The goal of this thesis is to explore the synthesis, characterization, photophysical, and photochemical properties of AIO hybrid materials. In particular, the first step is the synthesis of new organic ligands in order to obtain new type III compounds, followed by the structural characterization of the hybrid species; then photodegradation of common organic dyes, such as Methylene Blue (MB) and Rhodamine B (RhB), as organic pollutants solution model systems with the new hybrid compounds is studied.

The first part of the work (Chapter 2) relies on the synthesis and characterisation of functionalised ligands and the relative hybrid materials prepared from them. Target ligands are obtained through alkylation reaction of caffeine (used for type II hybrid compounds), DABCO and HMTA (employed for type III hybrid species); successful formation of the functionalised ligands has been assessed via NMR spectroscopy and sc-XRD. The synthesis of CuI-based hybrid materials has been performed mainly via slow diffusion method, in order to obtain single crystals: sc-XRD measurements were conducted to determine the success of the syntheses but also for structural characterisation of the hybrid materials.

The second part of the study (Chapter 3) revolves around the exploration of photophysical and functional properties of 1D-Cu_2I_3(Bz-HMTA) (MM4), chosen as the model catalyst for photoremediation applications. Rhodamine B (RhB) and Methylene Blue (MB) were the two molecules of choice for the role of organic pollutants in solution. Following a specific protocol for the preparation of a fine dispersion of catalyst powder into the dye solutions, two organic pollutants removal processes have been observed: an effective photodegradation of RhB and a strong physical adsorption of MB onto MM4 fine powder. In both cases, the residual concentration of the dyes at the end of the experiments is less than 10%.

Conclusions and perspectives are reported in Chapter 4, followed by the experimental part (Chapter 5).

1.7. References

1. Hei, X & Li, J. All-in.one: a new approach towards robust and solution-processable copper halide hybrid semiconductors by integrating covalent, coordinate and ionic bonds in their structures. *Chem. Sci.* **12**, 3805-3817 (2021).

2. Liu, W., Fang, Y., Li, J. Copper Iodide Based Hybrid Phosphors for Energy-Efficient General Lighting Technologies. *Adv. Funct. Mater.* **28**, 1705593 (2018).

3. Kagan, C. R., Mitzi, D. B., Dimitrakopoulos, C. D. Organic-Inorganic Hybrid Materials as Semiconducting Channels in Thin-Film Field-Effect Transistors. *Science* **286**, 945-947 (1999).

4. Schubert, U. Cluster-based inorganic-organic hybrid materials. *Chem. Soc. Rev.* **40**, 575-582 (2011).

5. Shi, Z., Guo, J., Chen, Y., Li, Q., Pan, Y., Zhang, H., Xia, Y., Huang, W. Lead-Free Organic–Inorganic Hybrid Perovskites for Photovoltaic Applications: Recent Advances and Perspectives. *Adv. Mater.* **29**, 1605005 (2017).

6. Brenner, T. M., Egger, D. A., Kronik, L., Hodes, G., Cahen, D. Hybrid organic-inorganic perovskites: low-cost semiconductors with intriguing charge-transport properties. *Nat. Rev. Mater.* **1**, 15007 (2016).

7. Cariati, E., Macchi, R., Roberto, D., Ugo, R., Galli, S., Casati, N., Macchi, P., Sironi, A., Bogani, L., Caneschi, A., Gatteschi, D. Polyfunctional Inorganic-Organic Hybrid Materials: An Unusual Kind of NLO Active Layered Mixed Metal Oxalates with Tunable Magnetic Properties and Very Large Second Harmonic Generation. *J. Am. Chem. Soc.* **129**, 9410-9420 (2007).

8. Yang, S., Niu, W., Wang, A.-L., Fan, Z., Chen, B., Tan, C., Lu, Q., Zhang, H. Ultrathin Two-Dimensional Organic–Inorganic Hybrid Perovskite Nanosheets with Bright, Tunable Photoluminescence and High Stability. *Angew. Chem.* **129**, 4316-4319 (2017).

9. Deng, W., Liang, X., Kubiak, P. S., Cameron, P. J. Molecular Interlayers in Hybrid Perovskite Solar Cells. *Adv. Energy Mater.* **8**, 1701544 (2018).

10. Li, Y. Molecular Design of Photovoltaic Materials for Polymer Solar Cells: Toward Suitable Electronic Energy Levels and Broad Absorption. *Acc. Chem. Res.* **45**, 723-733 (2012).

11. Raston, C. L., White, A. H. Crystal structure of the copper(I) iodide-pyridine (1/1) tetramer. *J. Chem. Soc., Dalton Trans.*, 2153-2156 (1976).

12. Parmeggiani, F., Sacchetti, A. Preparation and Luminescence Thermochromism of Tetranuclear Copper(I)−Pyridine−Iodide Clusters. *J. Chem. Educ.* **89**, 946-949 (2012).

13. Yam, V. W.-W., Au, V. K.-M., Leung S. Y.-L. Light-Emitting Self-Assembled Materials Based on d^8 and d^{10} Transition Metal Complexes. *Chem. Rev.* **115**, 7589-7728 (2015).

14. Peng, R., Li, M., Li, D. Copper(I) halides: A versatile family in coordination chemistry and crystal engineering. *Coord. Chem. Rev.* **254**, 1-18 (2010).

15. Tsuge, K., Chishina, Y., Hashiguchi, H., Sasaki, Y., Kato, M., Ishizaka, S., Kitamura, N. Luminescent copper(I) complexes with halogenido-bridged dimeric core. *Coord. Chem. Rev.* **306**, 636-651 (2016).

16. Wang, J.-J., Chen, C., Chen, W.-G., Yao, J.-S., Yang, J.-N., Wang, K.-H., Yin, Y.-C., Yao, M.-M., Feng, L.-Z., Ma, C., Fan, F.-J., Yao, H.-B. Highly Luminescent Copper Iodide Cluster Based Inks with Photoluminescence Quantum Efficiency Exceeding 98%. *J. Am. Chem. Soc.* **142**, 3686-3690 (2020).

17. Fang, Y., Liu, W., Teat, S. J., Dey, G., Shen, Z., An, L., Yu, D., Wang, L., O'Carroll, D. M., Li, J. A Systematic Approach to Achieving High Performance Hybrid Lighting Phosphors with Excellent Thermal and Photostability. *Adv. Funct. Mater.* **27**, 1603444 (2017).

18. Liu, W., Fang, Y., Wei, G. Z., Teat, S. J., Xiong, K., Hu, Z., Lustig, W. P., Li, J. A Family of Highly Efficient CuI-Based Lighting Phosphors Prepared by a Systematic, Bottom-up Synthetic Approach. *J. Am. Chem. Soc.* **137**, 9400-9408 (2015).

19. Zhang, X., Liu, W., Wei, G. Z., Banerjee, D., Hu, Z., Li, J. Systematic Approach in Designing Rare-Earth-Free Hybrid Semiconductor Phosphors for General Lighting Applications. *J. Am. Chem. Soc.* **136**, 14230-14236 (2014).

20. Zhang, N.-N., Sun, C., Jiang, X.-M., Xing, X.-S., Yan, Y., Cai, L.-Z., Wang, M.-S., Guo G.-C. Single-component small-molecule white light organic phosphors. *Chem. Comm.* **53**, 9269-9272 (2017).

21. Sharma, V. K., Guzelturk, B., Erdem, T., Kelestemur, Y., Demir, H. V. Tunable White-Light-Emitting Mn-Doped ZnSe Nanocrystals. *ACS Appl. Mater. Interfaces* **6**, 3654-3660 (2014).

22. Jin, L.-H., Li S.-M., Kwon, B.-J., Cho, Y.-H. Quenching dynamics in CdSe/ZnS core/shell quantum dots gold nanoparticle conjugates in aqueous solution. *J. Appl. Phys.* **109**, 124310 (2011).

23. Saparov, B., Mitzi D. B. Organic−Inorganic Perovskites: Structural Versatility for Functional Materials Design. *Chem. Rev.* **116**, 4558-4596 (2016).

24. Huang, X., Li, J., Zhang, Y., Mascarenhas, A. From 1D Chain to 3D Network: Tuning Hybrid II-VI Nanostructures and Their Optical Properties. *J. Am. Chem. Soc.* **125**, 7049-7055 (2003).

25. Ahn, D., Park, S.-H. Cuprous halides semiconductors as a new means for highly efficient light-emitting diodes. *Sci. Rep.* **6**, 20718 (2016).

26. Liu, W., Lustig, W. P., Li, J. Luminescent inorganic-organic hybrid semiconductor materials for energy-saving lighting applications. *EnergyChem* **1**, 100008 (2019).

27. Hei, X., Liu, W., Zhu, K., Teat, S. J., Jensen, S., Li, M., O'Carroll, D. M., Wei, K., Tan, K., Cotlet, M., Thonhauser, T., Li, J. Blending Ionic and Coordinate Bonds in Hybrid Semiconductor Materials: A General Approach toward Robust and Solution-Processable Covalent/Coordinate Network Structures. *J. Am. Chem. Soc.* **142**, 4242-4253 (2020).

28. Li, S.-L., Zhang, F.-Q., Zhang, X.-M. An organic-ligand-free thermochromic luminescent cuprous iodide trinuclear cluster: evidence for cluster centered emission and configuration distortion with temperature. *Chem. Comm.* **51**, 8062 (2015).

29. Zhang, X.-M. Hydro(solvo)thermal in situ ligand syntheses. *Coord. Chem. Rev.* **249**, 1201-1219 (2005).

30. Hou, J.-J., Li, S.-L., Li, C.-R. In situ alkylation of N-heterocycles in organic templated cuprous halides. *Dalton Trans.* **39**, 2701 (2010).

31. Liu, W., Zhu, K., Teat, S. J., Dey, G., Shen, Z., Wang, L., O'Carroll, D. M., Li, J. All-in-One: Achieving Robust, Strongly Luminescent and Highly Dispersible Hybrid Materials by Combining Ionic and Coordinate Bonds in Molecular Crystals. *J. Am. Chem. Soc.* **139**, 9281-9290 (2017).

32. Bondi, A. van der Waals Volumes and Radii. *J. Phys. Chem.* **68**, 441-451 (1964).

33. Artem'ev, A. V., Pritchina, E. A., Rakhmanova, M. I., Gritsan, N. P., Bagryanskaya, I. Y., Malysheva, S. F., Belogorlova, N. A. Alkyl-dependent self-assembly of the first red-emitting zwitterionic $\{Cu_4I_6\}$ clusters from [alkyl-P(2-Py)$_3$]+ salts and CuI: when size matters. *Dalton Trans.* **48**, 2328-2337 (2019).

34. Albert, I. D. L., Marks, T. J., Ratner, M. A. Large Molecular Hyperpolarizabilities. Quantitative Analysis of Aromaticity and Auxiliary Donor-Acceptor Effects. *J. Am. Chem. Soc.* **119**, 6575-6582 (1997).

35. Hei, X., Teat, S. J., Liu, W., Li, J. Eco-friendly, solution-processable and efficient low-energy lighting phosphors: copper halide based hybrid semiconductors $Cu_4X_6(L)_2$ (X = Br, I) composed of covalent, ionic and coordinate bonds. *J. Mater. Chem. C* **8**, 16790-16797 (2020).

36. Tian, B., Zheng, X., Kempa, T. J., Fang, Y., Yu, N., Yu, G., Huang, J., Lieber, C. M. Coaxial silicon nanowires as solar cells and nanoelectronic power sources. *Nature* **449**, 885-889 (2007).

37. Morkoç, H., Strite, S., Gao, G. B., Lin, M. E., Sverldlov, B., Burns, M. Large-band-gap SiC, III-V nitride, and II-VI ZnSe-based semiconductor device technologies. *J. Appl. Phys.* **76**, 1363-1398 (1994).

38. Szeles, C. CdZnTe and CdTe materials for X-ray and gamma ray radiation detector applications. *Phys. Status Solidi B* **241**, 783-790 (2004).

39. Nie, W., Tsai, H., Asadpour, R., Blancon, J.-C., Neukirch, A. J., Gupta, G., Crochet, J. J., Chhowalla, M., Tretiak, S., Alam, M. A., Wang, H.-L., Mohite, A. D. High-efficiency solution-processed perovskite solar cells with millimeter-scale grains. *Science* **347**, 522 (2015).

40. Fang, Y., Sojdak, C. A., Dey, G., Teat, S. J., Li, M., Cotlet, M., Zhu, K., Liu, W., Wang, L., O'Carroll, D. M., Li, J. Highly efficient and very robust blue-excitable yellow phosphors built on multiple-stranded one–dimensional inorganic–organic hybrid chains. *Chem. Sci.* **10**, 5363-5372 (2019).

41. Schwarzenbach, G. Der Chelateffekt. *Helv. Chim. Acta* **35**, 2344-2359 (1952).

42. Ford, P. C., Cariati, E., Bourassa, J. Photoluminescence Properties of Multinuclear Copper(I) Compounds. *Chem. Rev.* **99**, 3625-3647 (1999).

43. Perruchas, S., Le Goff, X. F., Maron, S., Maurin, I., Guillen, F., Garcia, A., Gacoin, T., Boilot, J.-P. Mechanochromic and Thermochromic Luminescence of a Copper Iodide Cluster. *J. Am. Chem. Soc.* **132**, 10967-10969 (2010).

44. Liu, W., Banerjee, D., Lin, F., Li, J. Strongly luminescent inorganic–organic hybrid semiconductors with tunable white light emissions by doping. *J. Mater. Chem. C* **7**, 1484-1490 (2019).

45. Artem'ev, A. V., Davydova, M. P., Hei, X., Rakhmanova, M. I., Samsonenko, D. G., Bagryanskaya, I. Yu., Brylev, K. A., Fedin, V. P., Chen, J.-S., Cotlet, M., Li, J. Family of Robust and Strongly Luminescent CuI-Based Hybrid Networks Made of Ionic and Dative Bonds. *Chem. Mater.* **32**, 10708-10718 (2020).

46. Benito, Q., Le Goff, X. F., Nocton, G., Fargues, A., Garcia, A., Berhault, A., Kahlal, S., Saillard, J.-Y., Martineau, C., Trébosc, J., Gacoin, T., Boilot, J.-P., Perruchas, S. Geometry Flexibility of Copper Iodide Clusters: Variability in Luminescence Thermochromism. *Inorg. Chem.* **54**, 4483-4494 (2015).

47. Liu, Z., Djurovich, P. I., Whited, M. T., Thompson, M. E. Cu_4I_4 Clusters Supported by P^N-type Ligands: New Structures with Tunable Emission Colors. *Inorg. Chem.* **51**, 230-236 (2012).

48. Chen, X.-M., Tong, M.-L. Solvothermal in Situ Metal/ Ligand Reactions: A New Bridge between Coordination Chemistry and Organic Synthetic Chemistry. *Acc. Chem. Res.* **40**, 162-170 (2007).

49. Lu, J. Y. Crystal engineering of Cu-containing metal–organic coordination polymers under hydrothermal conditions. *Coord. Chem. Rev.* **246**, 327-347 (2003).

50. Li, S.-L., Zhang, X.-M. Cu_3I_7 Trimer and Cu_4I_8 Tetramer Based Cuprous Iodide Polymorphs for Efficient Photocatalysis and Luminescent Sensing: Unveiling Possible Hierarchical Assembly Mechanism. *Inorg. Chem.* **53**, 8376-8383 (2014).

51. Blake, A. J., Brooks, N. R., Champness, N. R., Cooke, P. A., Deveson, A. M., Fenske, D., Hubberstey, P., Li, W.-S., Schröder, M. Controlling copper(I) halide framework formation using N-donor bridging ligand symmetry: use of 1,3,5-triazine to construct architectures with threefold symmetry. *J. Chem. Soc., Dalton Trans.*, 2103-2110 (1999).

52. James, S. L, Adams, C. J., Bolm, C., Braga, D., Collier, P., Friščić, Grepioni, F., Harris, K. D. M., Hyett, G., Jones, W., Krebs, A., Mack, J., Maini, L., Orpen, A. G., Parkin, I. P., Shearhouse, W. C., Steed, J. W., Waddell, D. C. Mechanochemistry: opportunities for new and cleaner synthesis. *Chem. Soc. Rev.* **41**, 413 (2012).

53. Kobayashi, A., Hasegawa, T., Yoshida, M., Kato, M. Environmentally Friendly Mechanochemical Syntheses and Conversions of Highly Luminescent Cu(I) Dinuclear Complexes. *Inorg. Chem.* **55**, 1978-1985 (2016).

54. Liu, W., Zhu, K., Teat, S. J., Deibert, B. J., Yuan, W., Li, J. A mechanochemical route toward the rational, systematic, and cost-effective green synthesis of strongly luminescent copper iodide based hybrid phosphors. *J. Mater. Chem. C* **5**, 5962 (2017).

55. Chen, C., Li, R.-H., Zhu, B.-S., Wang, K.-H., Yao, J.-S., Yin, Y.-C., Yao, M.-M., Yao, H.-B., Yu, S.-H. Highly Luminescent Inks: Aggregation-Induced Emission of Copper–Iodine Hybrid Clusters. *Angew. Chem. Int. Ed.* **57**, 7106-7110 (2018).

56. Huang, X. Red phosphor converts white LEDs. *Nat. Photonics* **8**, 748-749 (2014).

57. Kim, Y. H., Arunkumar, P., Park, S. H., Yoon, H. S., Im, W. B. Tuning the diurnal natural daylight with phosphor converted white LED – Advent of new phosphor blend composition. *Mater. Sci. Eng. B* **193**, 4-12 (2015).

58. Dutta, T., Kim, K.-H., Uchimiya, M., Kwon, E. E., Jeon, B.-H., Deep, A., Yun, S.-T. Global demand for rare earth resources and strategies for green mining. *Environ. Res.* **150**, 182-190 (2016).

59. Currie, M. J., Mapel, J. K., Heidel, T. D., Goffri, S., Baldo, M. A. High-Efficiency Organic Solar Concentrators for Photovoltaics. *Science* **321**, 226-228 (2008).

60. Meinardi, F., McDaniel, H., Carulli, F., Colombo, A., Velizhanin, K. A. Makarov, N. S., Simonutti, R., Klimov, V. I., Brovelli, S. Highly efficient large-area colourless luminescent solar concentrators using heavy-metal-free colloidal quantum dots. *Nat. Nanotechnol.* **10**, 878-885 (2015).

34

61. Tummeltshammer, C., Taylor, A., Kenyon, A. J., Papakonstantinou, I. Losses in luminescent solar concentrators unveiled. *Sol. Energy Mater. Sol. Cells* **144**, 40-47 (2016).

62. Liu, J., Zhuang, Y., Wang, L., Zhou, T., Hirosaki, N., Xie, R.-J. Achieving Multicolor Long-Lived Luminescence in Dye-Encapsulated Metal-Organic Frameworks and Its Application to Anticounterfeiting Stamps. *ACS Appl. Mater. Interfaces* **10**, 1802-1809 (2018).

63. Atchudan, R., Edison, T. N. J. I., Aseer, K. R., Perumal, S., Karthik, N., Lee, Y. R. Highly fluorescent nitrogen-doped carbon dots derived from *Phyllanthus acidus* utilized as a fluorescent probe for label-free selective detection of Fe^{3+} ions, live cell imaging and fluorescent ink. *Biosens. Bioelectron.* **99**, 303-311 (2018).

64. Xu, L., Chen, J., Song, J., Li, J., Xue, J., Dong, Y., Cai, B., Shan, Q., Han, B., Zeng, H. Double-Protected All-Inorganic Perovskite Nanocrystals by Crystalline Matrix and Silica for Triple-Modal Anti-Counterfeiting Codes. *ACS Appl. Mater. Interfaces* **9**, 26556-26564 (2017).

65. Xie, S., Gong, G., Song, Y., Tan, H., Zhang, C., Li, N., Zhang, Y., Xu, L., Xu, J., Zheng, J. Design of novel lanthanide-doped core–shell nanocrystals with dual up-conversion and down-conversion luminescence for anti-counterfeiting printing. *Dalton Trans.* **48** (20), 6971-6983 (2019).

66. Gao, Y., Pu, X., Zhang, D., Ding, G., Shao, X., Ma, J. Combustion synthesis of graphene oxide–TiO_2 hybrid materials for photodegradation of methyl orange. *Carbon* **50**, 4093-4101 (2012).

67. Fujishima, A., Zhang, X., Tryk, D. A. TiO_2 photocatalysis and related surface phenomena. *Surf. Sci. Rep.* **63** (12), 515-582 (2008).

68. Chang, M., Zou, H., Song, Y., Chen, J., Cui, L., Sheng, Y., Zheng, K. Photoluminescence and photodegradation properties of $SiO_2@TiO_2:Sm^{3+}$ with different coating effects. *J. Phys. Chem. Solids* **124**, 100-110 (2019).

69. Cui, Y. In-situ synthesis of C_3N_4/CdS composites with enhanced photocatalytic properties. *Chinese J. Catal.* **36**, 372-379 (2015).

70. Cheng, W., Wang, Y., Ge, S., Ding, X., Cui, Z., Shao, Q. One-step microwave hydrothermal preparation of Cd/Zr-bimetallic metal–organic frameworks for enhanced photochemical properties. *Adv. Compos. Mater.* **4**, 150-161 (2021).

71. Lai, J., Jiang, X., Zhao, M., Cui, S., Yang, J., Li, Y. Thickness-dependent layered $BiOIO_3$ modified with carbon quantum dots for photodegradation of bisphenol A: Mechanism, pathways and DFT calculation. *Appl. Catal. B* **298**, 120622 (2021).

72. Chang, C.-F., Man, C.-Y. Magnetic photocatalysts of copper phthalocyanine-sensitized titania for the photodegradation of dimethyl phthalate under visible light. *Colloids and Surfaces A: Physicochem. Eng. Aspects* **441**, 255-261 (2014).

73. Xia, S., Zhang, X., Zhou, X., Meng, Y., Xue, J., Ni, Z. The influence of different Cu species onto multi-copper-contained hybrid materials' photocatalytic property and mechanism of chlorophenol degradation. *Applied Catalysis B: Environmental* **214**, 78-88 (2017).

74. Liu, J.-J., Xiang, Z., Guan, Y.-F., Huang, C.-C., Lin, M.-J. Two novel donor-acceptor hybrid heterostructures with enhanced visible-light photocatalytic properties. Dalton Trans. 47, 12041-12045 (2018).

75. Zhao, R.-Y., Xu, R.-D., Liu, G.-N., Sun, Y., Li, C. Water stable tetranuclear copper(I) iodide cluster for visible-light driven photocatalytic application. *Inorganic Chemistry Communications* **105**, 135-139 (2019).

76. Qiao, X., Wang, C., Niu, Y. N-Benzyl HMTA induced self-assembly of organic-inorganic hybrid materials for efficient photocatalytic degradation of tetracycline. *Journal of Hazardous Materials* **391**, 122121 (2020).

77. Lei, X.-W., Yue, C.-Y., Wang, S., Gao, H., Wang, W., Wang, N., Yin, Y.-D. Di-pyridyl organic cation directed hybrid cuprous halogenides: syntheses, crystal structures and photochromism and photocatalysis. *Dalton Trans.* **46**, 4209-4217 (2017).

Chapter 2

Design of organic ligands and synthesis of CuI-based hybrid materials

This Chapter will discuss how ligands have been synthesised, starting from the model ligand molecules, and passing to the alkylation process with different organic species. Then, the preparation of the CuI-based hybrid materials will be treated as well, with a focus on the two main synthetic routes and the adjustment needed in the synthesis setup due to the properties of the different functionalised ligands. NMR spectroscopy (and in some cases, sc-XRD measurements) have been used to characterise the obtained ligands, while sc-XRD measurements has been chosen to characterise the obtained hybrid compounds.

2.1. *Synthetic purposes*

The preparation of new functionalised organic ligands, as well as the adjustments in the reaction conditions, are of paramount importance for the exploration of the CuI-based hybrid materials class.

In the present thesis, four are the molecules selected for the role of ligands: pyridine, caffeine, DABCO, and HMTA. Apart from pyridine (used in the synthesis of the archetypal compound $Cu_4I_4(py)_4$)[1], all the other species underwent a functionalisation process: in doing so, the molecules acquired a new set of chemical properties suitable for the needs of type II and type III hybrid

materials (cationic character, an adequate amount of binding sites, a variable steric hindrance, different electronic properties, inclusion of a π-extended system).

Regarding CuI-based hybrid compounds, although a great variety of synthetic paths for are possible (see Chapter 1.4), two main routes have been followed in the present work: the direct mixing of CuI and the specific ligand in the reaction solvent; the slow diffusion method[2], in which CuI and the selected ligand are dissolved into two different solvents and are kept separated by a third solvent, which acts as an interphase granting a controlled diffusion of reacting species. The former allows shorter reaction times (from minutes to hours); products are obtained in the form of a fine powder (nucleation process of the reaction seeds prevails over the growth one). The latter requires longer reaction times (from days to weeks); products are isolated in the form of single crystals (growth process of the reaction seeds prevails over the nucleation one). Depending on the desired physical state of the resulting hybrid material, one way has been preferred over the other.

In the following sections, the synthesis of functionalised ligands first and CuI hybrid materials then are presented , along with their respective characterisation analysis.

2.2.   Choices of ligand molecules

The choice of ligand affects hybrid materials nature (type I, type II, type III), dimensionality (0D, 1D, 2D, 3D), and photophysical properties. For what concerns the nature of the resulting hybrid compounds, the ligand can provide coordinative bonds (type I), ionic bonds (type II), or both (type III, also referred as AIO). The dimensionality of the products depends on the number of ligand binding sites[3-5]: 0D if it is one, 1D if it is two, 2D if it is three, and 3D if it is four or more. For ligands possessing more than one coordination site, it is worth underlining that steric hindrance can lead to lower dimensionality materials. Regarding the photophysical properties of the CuI-based hybrid species, the electron withdrawing or electron donating nature of the ligands influences the bond lengths with the inorganic core, thus determining the possibility to tune the resulting absorption and emission properties. Although also type I (MM0) and type II (MM22) hybrid compounds were synthesised, the present thesis focuses on type III (AIO) hybrid materials: so, the molecules chosen as ligands particularly fit this purpose.

For the synthesis of type I and type II CuI-based hybrid materials, pyridine and caffeine were chosen, respectively (Fig. 2.1). The former possesses one binding site and was used without any functionalisation reaction, leading to the formation of the archetypal $Cu_4I_4(py)_4$ tetrameric cluster

(type I); the latter was methylated in order to grant the synthesis of an ionic hybrid material (type II). Moreover, pyridine was the only aromatic molecule directly used as a ligand in the synthesis of this thesis CuI-based hybrid materials.
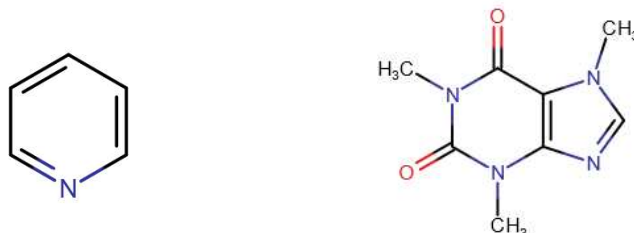
Figure 2.1 Molecular structure of pyridine (left), employed for the synthesis of type I hybrid compound, and caffeine (right), chosen for the preparation of type II hybrid material.

This thesis target AIO hybrid materials have been those obtained with functionalised aliphatic ligands. Going more into detail, the two main ligand molecules employed in the present work were 1,4-diazabicyclo[2.2.2]octane (DABCO) and hexamethylenetetramine (HMTA) (Fig. 2.2). In order to obtain AIO hybrid materials, ligands containing at least two coordinating atoms are needed, and both DABCO and HMTA fulfil this condition. The reason behind this need is related to the nature of type III compounds: given the presence of either coordinative and ionic bonds, ligand molecules must be positively charged while still possessing atoms with lone pairs capable of saturating the coordination sphere of Cu atoms in the inorganic anionic module.

Figure 2.2 Molecular structure of 1,4-diazabicyclo[2.2.2]octane (DABCO, left) and hexamethylenetetramine (HMTA, right).

DABCO and HMTA are two of the most diffuse organic species employed in the preparation of AIO hybrid materials[3-5]. As already mentioned in the chapter 1.2 (type III structure), DABCO allows the synthesis of 0D hybrid materials while HMTA enables the preparation of higher

dimensionality (1D, 2D) CuI-based hybrid compounds. Either DABCO and HMTA underwent monoalkylation reactions: in doing so, the former was left with one binding site while the latter had three atoms potentially capable of saturating Cu coordination sphere.

2.3.   Functionalisation of organic ligands

The main route for the desired molecules functionalisation was nucleophilic substitution of alkyl halides in order to perform an efficient alkylation of caffeine, DABCO, and HMTA. The starting ligand was put in a reaction flask together with the specific alkylating group: the system was then kept under stirring at the given experimental conditions since the completion of the reaction; after that, the different products were isolated and characterised.

Caffeine was methylated by direct mixing with methyl iodide (MeI), following a reaction path already present in literature[6]: the obtained methyl caffenium iodide (MM19L) has a cationic character, and no binding atoms are left (Fig. 2.3).
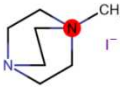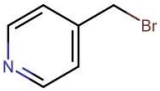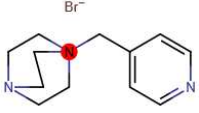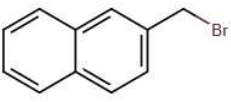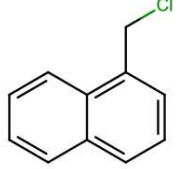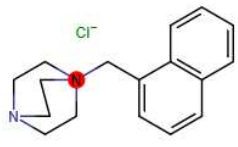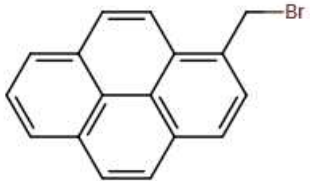
Figure 2.3 *Molecular structure of methyl caffenium iodide (MM19L). The cationic nitrogen is indicated within the red dot.*

DABCO and HMTA were reacted with a series of alkyl halides with increasing steric hindrance, starting from MeI up to 1-(bromomethyl)pyrene. DABCO was reacted with the following alkyl halides: methyl iodide (MeI), (4-methyl)pyridine (mePyBr), benzyl chloride (BzCl), (1-chloromethyl)naphthalene (1-NfCl), (2-bromomethyl)naphthalene (2-NfBr), (1-bromomethyl)pyrene (mePyrnBr). On the other hand, HMTA was functionalised with the following species: benzyl chloride (BzCl), (1-chloromethyl)naphthalene (1-NfCl), (2-bromomethyl)naphthalene (2-NfBr), (1-bromomethyl)pyrene (mePyrnBr). Functionalisation

reactions with DABCO are shown in Table 2.1 while those regarding HMTA are illustrated in Table 2.2.
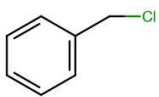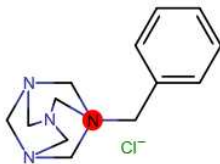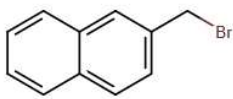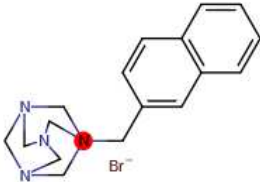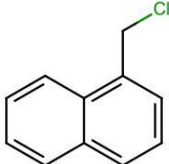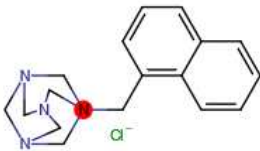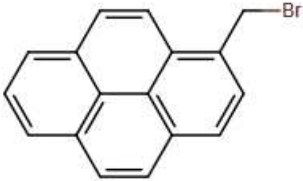
Table 2.1 *Schematic representation of the reaction between DABCO and the series of alkyl halides, along with the target ligands. Alkyl halides are abbreviated as follows: methyl iodide (MeI), (4-methyl)pyridine (mePyBr), benzyl chloride (BzCl), (1-chloromethyl)naphthalene (1-NfCl), (2-bromomethyl)naphthalene (2-NfBr), (1-bromomethyl)pyrene (mePyrnBr). The resulting functionalised ligands are indicated by their chosen acronyms.*

Starting ligand	Alkyl halide		Functionalised ligand		Obtained
	Name	**Structure**	**Name**	**Structure**	
	HBr	H——Br	MM28L		Yes
	MeI	H₃C——I	MM1L		Yes
	mePyBr		MM14L		No
DABCO	2-NfBr		MM5L		Yes
	1-NfCl		MM6L		Yes
	mePyrnBr		MM24L		No

Due to an undesired result in the preparation of 1-(4-methyl)pyridine-4-aza-1-azoniabicyclo[2.2.2]octane bromide ((mePy-DABCO)Br, MM16L), a protonation reaction of DABCO with HI was performed to obtain the same product (namely, MM28L). Apart from HI and MeI, all the other alkyl fragments contain aromatic groups: besides steric effects, the influence of

π-extended systems of different dimensions on the resulting hybrid materials wanted to be studied as well.

Table 2.2 *Schematic representation of the reaction between HMTA and the series of alkyl halides, along with the target ligands. Alkyl halides are abbreviated as follows: methyl iodide (MeI), benzyl chloride (BzCl), (1-chloromethyl)naphthalene (1-NfCl), (2-bromomethyl)naphthalene (2-NfBr), (1-bromomethyl)pyrene (mePyrnBr). The resulting functionalised ligands are indicated by their chosen acronyms.*

Starting ligand	Alkyl halide		Functionalised ligand		Obtained
	Name	**Structure**	**Name**	**Structure**	
	BzCl		MM3L		Yes
	2-NfBr		MM10L		Yes
HMTA	1-NfCl		MM11L		Yes
	mePyrnBr		MM26L		No

2.4. *Characterisation of functionalised ligands*

The as prepared ligands were characterised by ^{1}H nuclear magnetic resonance (NMR) spectroscopy and, in some cases by X-ray diffraction (XRD) analysis. Some of the NMR spectra are not clearly informative due to a series of issues (solubility, concentration, ligand purity, noise signals, etc.); for XRD measurements, there have been other major issues such as the highly deliquescent behaviour of some compounds (e.g., MM10L).

- ^{1}H-NMR spectroscopy

The successful synthesis of the functionalised ligands, precursors of the desired hybrid materials, was verified by ^{1}H-NMR spectroscopy. Peak assignation of the obtained target ligands (namely, MM1L, MM3L, MM5L, MM6L, MM19L; see Table 2.1 and Table 2.2) is reported in the experimental section, chapter 5.1 (Ligands synthesis). For what concerns MM10L and MM11L, the registered NMR spectra showed the presence of impurities: in order to obtain more detailed information, a purification process is needed. NMR spectrum of MM28L was not registered since the same protonation protocol of MM14L was followed: the ligand was used as such and the success of the synthesis is evidenced in the XRD structure of the obtained hybrid material (see Chapter 2.7). The NMR spectra of the remaining target ligands (MM14L, MM24L, MM26L) have been informative about the failure of the respective alkylation reactions.

- XRD measurements

After being recrystallised in CH$_3$CN, (2-Nf-DABCO)Cl (**MM5L**) was isolated as single crystals and structurally characterised via sc-XRD measurements.

MM5L ligand structure was resolved and refined in the orthorhombic spatial group Pca2$_1$ (Fig. 2.4). More detailed information can be found in the crystallographic table reported in the *Appendix* section (Table A.1). The asymmetric unit contains three crystallographic independent molecules, alongside with their anionic Br$^-$ counterpart that ensures charge neutrality. The packing of **MM5L** inside the crystal evidences a pattern in which columns of molecules with the DABCO

fragment pointing downwards alternate with columns of molecules with the same fragment pointing upwards.
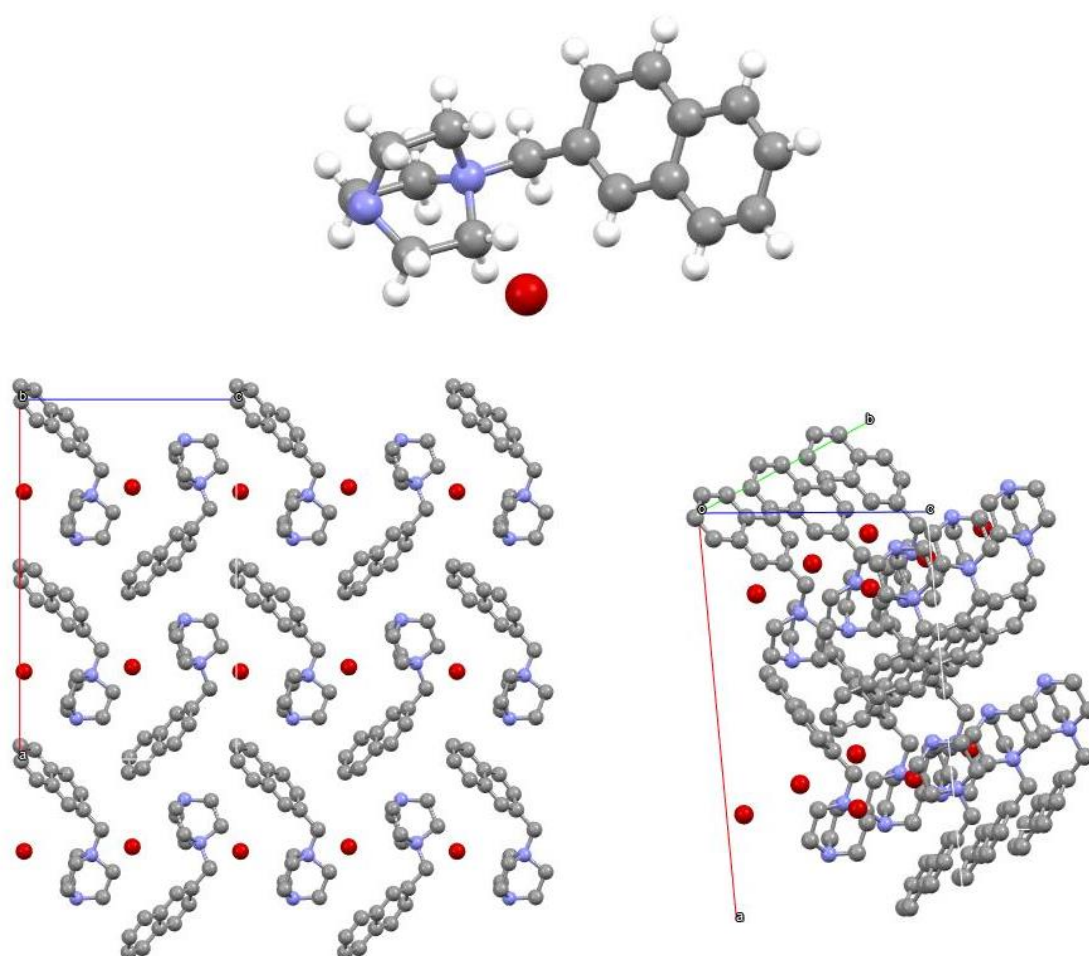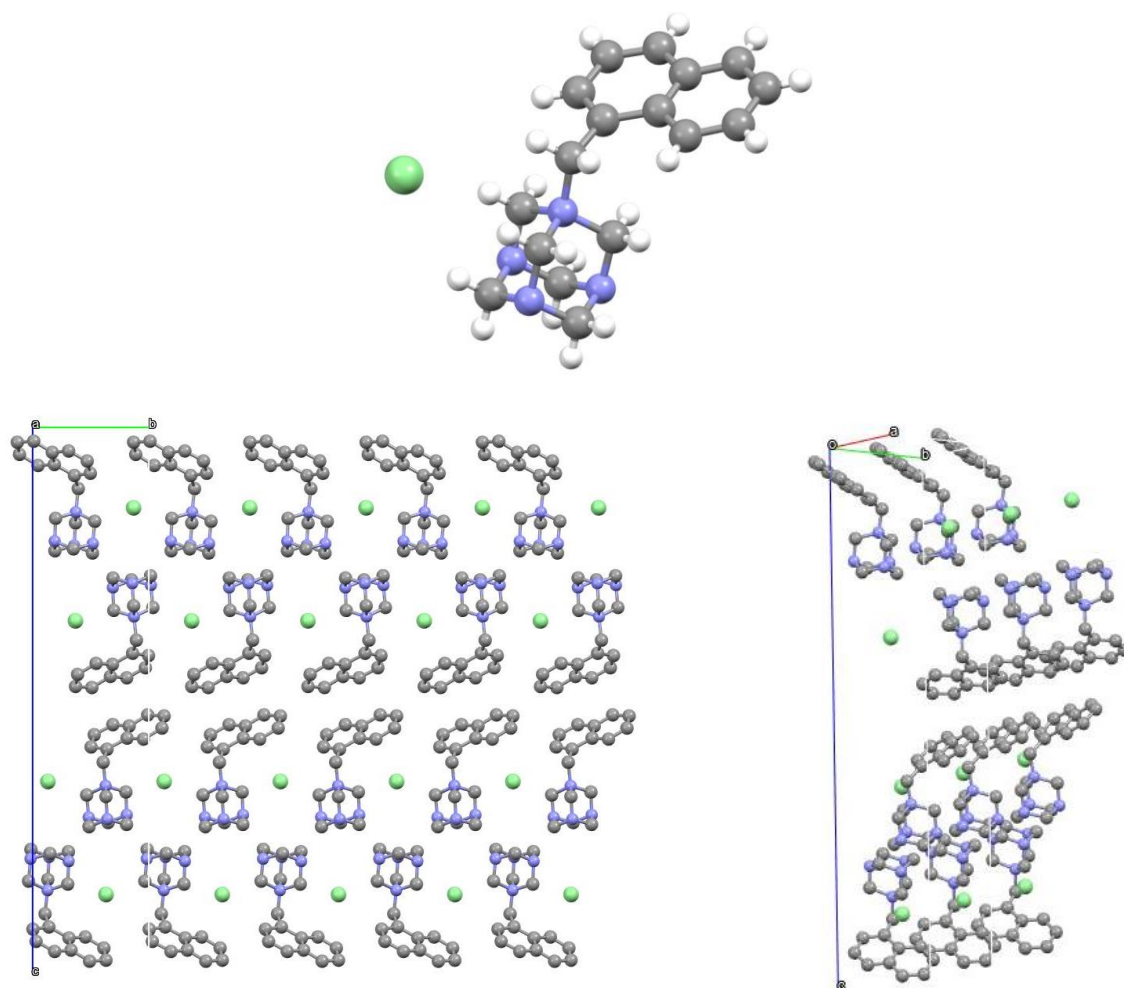

*Figure 2.4 Molecular structure of (2-Nf-DABCO)Cl (**MM5L**) (top, centre). Molecular packing of **MM5L** inside the crystal along the b axis (bottom, left), together with the packing from a different view in order to display the spatial disposition between neighbouring naphthalenes (bottom, right); hydrogens were omitted for a better visual clarity. Colour scheme: H, white; Br, dark red; C, grey; N, blue.*

XRD structure of (1-Nf-DABCO)Cl (**MM11L**) was obtained during the measurements of the corresponding CuI-based hybrid material (MM13, see Chapter 2.6), thus implying the reactions did not took the expected outcome.

MM11L ligand structure was resolved and refined in the orthorhombic spatial group P2$_1$2$_1$2$_1$ (Fig. 2.5). More detailed information can be found in the crystallographic table reported in the *Appendix* section (Table A.2). The asymmetric unit contains one crystallographic independent molecule, alongside with its anionic Cl$^-$ counterpart that ensures charge neutrality. The packing of **MM11L** inside the crystal evidences a pattern in which rows of molecules with the HMTA fragment pointing downwards alternate with rows of molecules with the same fragment pointing

44

upwards: this disposition ensures an effective π-stacking between neighbouring naphthalenes, granting a more efficient and stable packing of the molecules in the crystal.


Figure 2.5 *Molecular structure of (1-Nf-DABCO)Cl (**MM11L**) (top, centre). Molecular packing of **MM11L** inside the crystal along the a axis (bottom, left), together with the packing from a different view in order to further emphasise the π-stacking between neighbouring naphthalenes (bottom, right); hydrogens were omitted for a better visual clarity. Colour scheme: H, white; Cl, light green; C, grey; N, blue.*

2.5. Type I, type II compounds

Type III (AIO) hybrid compounds are the main focus of the present thesis; however, one CuI-based hybrid material for both type I and type II subgroups were synthesised for the seek of completion.

$Cu_4I_4(py)_4$ tetrameric cluster (MM0) was chosen as the representative of type I compounds: it was obtained following the standard synthetic protocol reported in literature[1]. It constitutes the archetype of the entire class of CuI-based hybrid materials: it was first synthesised in 1976[7] and is

one of the most studied structure. MM0 possesses a 0D structure (i.e., cluster nature; see Fig. 1.2) and is well-known for its thermochromic behaviour. Thermochromism is a property by which a substance changes its colour depending on its temperature; the characteristic luminescence for MM0 at room temperature, under a 254 nm wavelength UV irradiation, corresponds to yellow (as it can be seen in Fig. 2.6). In this specific case, the change in temperature is related to a variation in Cu···Cu distances, thus implying CC emission is the main luminescence path determining this photophysical property.
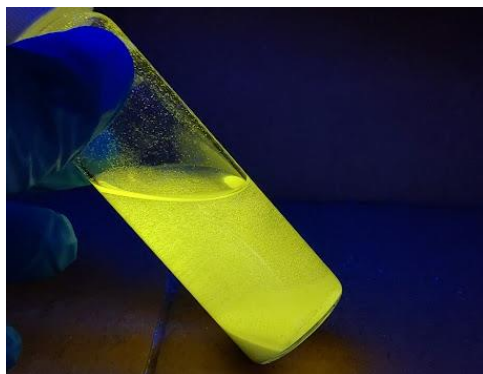
Figure 2.6 *Archetypal Cu$_4$I$_4$(py)$_4$ (MM0) characteristic yellow luminescence at room temperature, under 254 nm UV lamp irradiation.*

The successful synthesis of MM0 in the form of a fine powder was enough to let this synthetic procedure be used as the standard protocol for the preparation of the other CuI-based hybrid materials in the same physical phase.

For what concerns type II compounds, [meCaf][CuI$_2$] (MM22) was synthetised in order to include this subgroup of CuI hybrid species in the present work. MM22 was obtained in the form of a white solid (Fig. 2.7) and showed no luminescence properties, coherently to the net charge separation of ionic compounds.
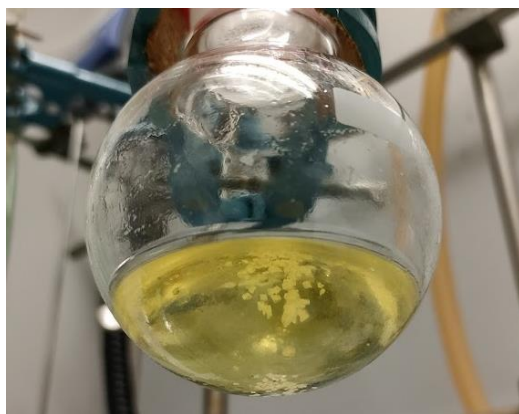
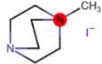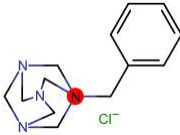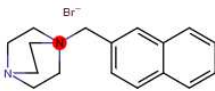*Figure 2.7* *[meCaf][CuI$_2$] (MM22) obtained in the form of a white solid.*

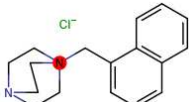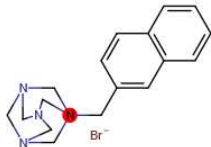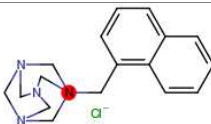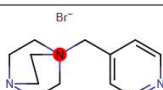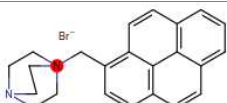## 2.6. Type III compounds (AIO)

All the functionalised ligands reported in Chapter 2.3 (with the exception of MM19L) were prepared for the sole purpose of exploring new areas of this subgroup of hybrid compounds. Going more into detail, the effects of variations in ligands nature and in reaction setups on the effective obtainment of the target hybrid species wanted to be investigated.

Despite the different synthetic routes possible (see Chapter 1.4), all the CuI-based hybrid materials have been obtained adopting the slow diffusion method. The only exception was 1D-Cu_2I_3(Bz-HMTA): it was employed as the model catalyst in the photodegradation experiments, so it was prepared either as single crystals (MM4; slow diffusion method, small quantity) and as a fine powder (MM7; direct mixing, larger quantity). The general protocol for the preparation of AIO hybrid compounds provides the following setup: 1 mL of a KI saturated aqueous solution containing CuI is added into a vial; then, 1 mL of acetonitrile (ACN) is slowly added on top of the aqueous solution in order to generate the first interface; after that, a methanol (MeOH) solution containing the ligand is slowly deposited over the ACN layer. The vial is then closed and carefully kept in a place where the reaction can proceed unperturbed. It is important to note that the three solvents are miscible and are disposed from the bottom to the top in order of decreasing density. Depending on the different ligands properties, some adjustments had to be made, such as an increase in solvent volumes or a change of solvents (and sometimes a subsequent inversion in the deposition order of CuI and the ligand). Another interesting parameter is the stoichiometric ratio between ligand and CuI (L:Cu ratio). Different L:Cu ratio have been explored, going from 5:1 to 1:5. One of the main reasons behind this choice was to verify if different L:Cu ratios lead to products with different stoichiometry. What was found is that only one stoichiometry per ligand was obtained. Furthermore, vials containing Cu in stoichiometric excess showed a considerable quantity of red luminescent impurities under UV irradiation (i.e., unreacted CuI): the issue has been solved by working with ligands stoichiometric excess. More detailed information can be found in

the *Experimental* section (Chapter 5.2). [$Cu_4I_6(me\text{-}HMTA)_2$] was not synthesised since it was already present in literature[9]. All the AIO hybrid materials synthesis are summarised in Table 2.3.

Table 2.3 Schematic representation of CuI-based hybrid materials synthesis, along with the employed functionalised ligands. Ligands are indicated by their structures and their acronyms. Acronyms in brackets are referred to a different physical phase of the product (MM7; fine powder) or to a use of different solvents (MM23).

Functionalised ligand		Target CuI-based hybrid material		Obtained
Name	Structure	Name	Stoichiometry	
MM1L		MM2	0D-Cu_4I_6(me-DABCO)$_2$	Yes
MM3L		MM4 (MM7)	1D-Cu_2I_3(Bz-HMTA)	Yes
MM5L		MM8	0D-Cu_3I_4(2-Nf-DABCO)$_2$	Yes
MM6L		MM9	0D-Cu_xI_y(1-Nf-DABCO)$_z$	No
MM10L		MM12	1D-Cu_xI_y(2-Nf-HMTA)$_z$	No
MM11L		MM13 (MM23)	1D-Cu_xI_y(1-Nf-HMTA)$_z$	No
MM14L		MM16	0D-Cu_xI_y(mePy-DABCO)$_z$	No
MM24L		MM25	0D-Cu_xI_y(mePyrn-DABCO)$_z$	No
MM26L		MM27	1D-Cu_xI_y(mePyrn-HMTA)$_z$	No
MM28L		MM29	[CuI_3(H-DABCO)]K	Yes

Regarding AIO hybrid compounds luminescence properties, the preliminary emission behaviour of each species has been examined by irradiation under a UV lamp. Each sample was irradiated

with two wavelengths, namely 256 nm and 365 nm. Luminescence properties of AIO compounds are schematically reported in Table 2.4.

Table 2.4 *Schematic representation of target CuI-based hybrid materials luminescence properties, along with the corresponding excitation wavelength.*

| Target CuI-based hybrid material		Luminescence	Intensity	Excitation wavelength (nm)
Name	Stoichiometry			
MM2	0D-Cu_4I_6(me-DABCO)$_2$	Light blue	High	254
MM4 (MM7)	1D-Cu_2I_3(Bz-HMTA)	Green	High	254
		Green	High	365
MM8	0D-Cu_3I_4(2-Nf-DABCO)$_2$	-		
MM9	0D-Cu_xI_y(1-Nf-DABCO)$_z$	-		
MM12	1D-Cu_xI_y(2-Nf-HMTA)$_z$	-		
MM13 (MM23)	1D-Cu_xI_y(1-Nf-HMTA)$_z$	Yellow	Low	254
MM16	0D-Cu_xI_y(mePy-DABCO)$_z$	-		
MM25	0D-Cu_xI_y(mePyrn-DABCO)$_z$	Light blue	Low	254
		Light blue	High	365
MM27	1D-Cu_xI_y(mePyrn-HMTA)$_z$	Yellow	Low	254
		Pale green	High	365
MM29	[CuI_3(H-DABCO)]K	-		

Luminescence patterns of MM13, MM25, MM27 reflect that of the pure ligands, thus further confirming the synthesis of the target AIO hybrid materials has not occurred.

MM2 shows a distinct light blue luminescence under 254 nm light irradiation, as it can be seen from Fig. 2.8.


Figure 2.8 *MM2 characteristic luminescence under 254 nm UV light irradiation.*

For what concerns MM4, different L:Cu ratio have been tried during the synthetic preparation of the first batch of the hybrid compound. After subsequent adjustments, two ratios proved to be the most effective: 1:3 (Fig. 2.9, left) and 3:1 (Fig. 2.9, right). Under 254 nm light irradiation, in reaction vials containing ligand and CuI in 1:3 ratio, the presence of a red luminescent solid was noted: this impurity corresponds to unreacted CuI (which has a characteristic dark red appearance under UV irradiation; Fig. 2.10); going from 1:3 to 3:1 ratio solved this issue, granting an easier and more efficient product isolation.
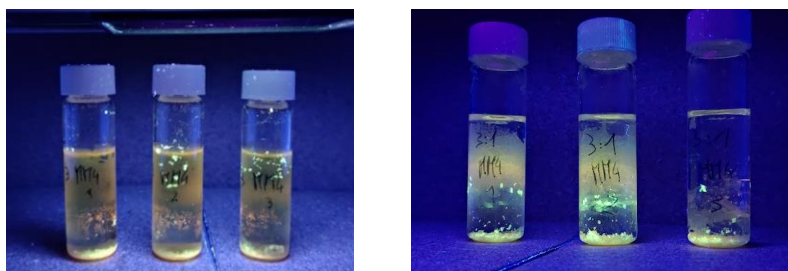

Figure 2.9 MM4 first batch 1:3 (left) and 3:1 (right) L:Cu ratio under 254 nm wavelength UV lamp irradiation.
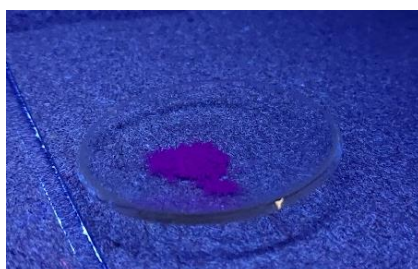
Figure 2.10 CuI dark red luminescence under UV lamp irradiation.

Due to the observations during the preparation of the first MM4 batch, no traces of excess CuI impurities were observed in the second batch. The only impurities into the vials were those of the excess ligand, which exhibits a green luminescence at 365 nm and a yellow luminescence at 254 nm (Fig. 2.11).
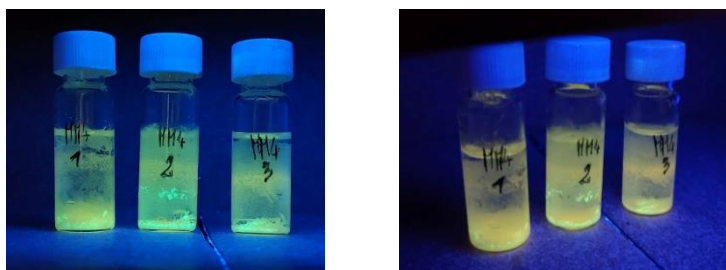
Figure 2.11 MM4 3:1 2nd batch under 365 nm (left) and 254 nm (right) wavelength UV lamp irradiation.

Thermochromic behaviour of the obtained hybrid materials have not been explored.

MM29 (equal to MM16, see Chapter 2.7) can be seen as an intermediate between type II and type III compounds: although it has a direct coordinative bond between the inorganic core and H-DABCO, its structural unit reaches neutrality thanks to the K^+ ion , thus bringing the stoichiometry of the product to that of an ionic species. Further confirmation of this statement comes from the analysis of its XRD structure, as will be better displayed in the next section. It is also important to notice that MM29 does not show luminescence, reflecting type II hybrid compounds behaviour.

2.7. X-ray structural analysis of CuI-based hybrid materials

AIO hybrid materials were isolated as single crystals and then structurally characterised by single-crystal X-ray diffraction (sc-XRD).

MM4 structure was solved and refined in the triclinic spatial group P-1 (Fig. 2.12). More detailed information can be found in the crystallographic table reported in the *Appendix* section (Table A.3). The asymmetric unit suggests the CuI-based hybrid material having the stoichiometry 1D-Cu_2I_3(Bz-HMTA). Atoms in the structural unit generated by symmetry operations are indicated by the symbol "§" (Fig. 2.12, top left) and are, namely, going from left to right: $I2^§$ (1+x, y, z), $Cu1^§$ (2-x, -y, 1-z), $I2^§$ (1-x, -y, 1-z), $Cu2^§$ (1-x, -y, 1-z), $I1^§$ (1-x, -y, 1-z), $Cu1^§$ (1-x, -y, 1-z). Bond lengths, going from left to right, are the following: $Cu1-I2^§$, 2.730 Å; $Cu1-Cu1^§$, 2.625 Å; $Cu1-I2^§$, 2.625 Å; $Cu1-Cu2^§$, 2.862 Å; Cu1-I1, 2.578 Å; Cu1-N1, 2.195 Å; Cu2-N2, 2.239 Å; $Cu2-I1^§$, 2.629 Å; $Cu2-Cu1^§$, 2.862 Å; Cu2-I2, 2.667 Å; Cu2-I3, 2.593 Å. Bond lengths suggest Cu atoms possess a distorted tetrahedral coordination geometry. The 1D polymeric linear structure of **MM4** is composed of structural unit with HMTA fragment pointing upwards and downwards, alternatively. The packing of **MM4** inside the crystal evidences a pattern in which rows of linear chains are one next to the other oriented in the same direction: this disposition ensures an effective

π-stacking between neighbouring benzyls, granting a more efficient and stable packing of the chains in the crystal.
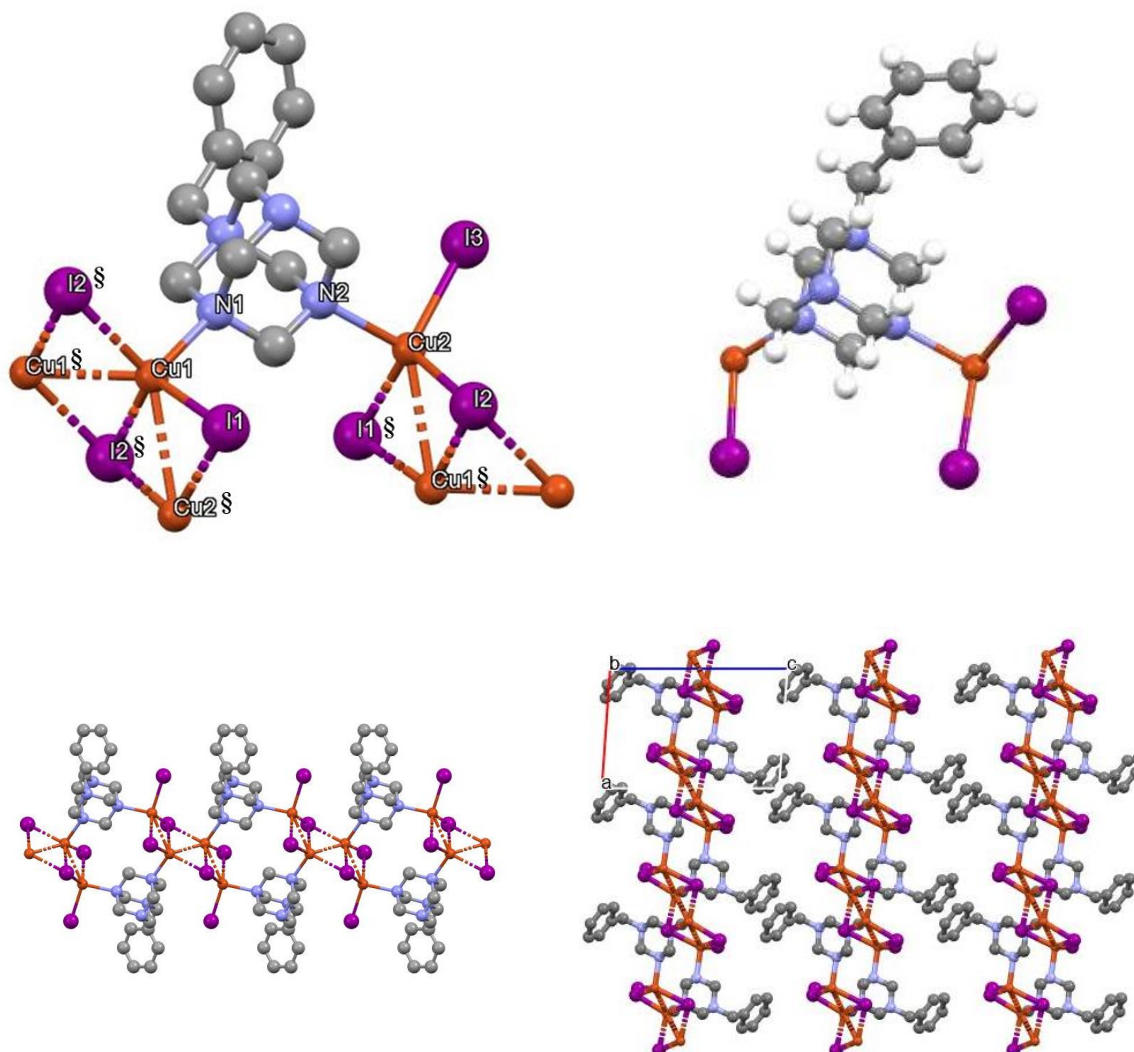
Figure 2.12 *Structural unit of 1D-Cu₂I₃(Bz-HMTA)* *(MM4)* *with labelled atoms (top, left) along with its asymmetric unit (top, right). Polymeric 1D linear chain structure of* *MM11L* *(bottom, left), together with the packing of the chains inside the crystal along the b axis in order to emphasise the π-stacking between neighbouring benzyls (bottom, right); hydrogens were omitted for a better visual clarity. Colour scheme: Cu, orange; I, purple; N, blue; C, grey; H, white.*

MM8 structure was solved and refined in the monoclinic spatial group $P2_1/n$ (Fig. 2.13). More detailed information can be found in the crystallographic table reported in the *Appendix* section (Table A.4). The asymmetric unit suggests the CuI-based hybrid material having the stoichiometry 0D-Cu₃I₅(2-Nf-DABCO)₂. Bond lengths, going from left to right, are the following: Cu1-N1, 2.071 Å; Cu1-I1, 2.547 Å; Cu1-I2, 2.804 Å; Cu1-I3, 2.756 Å; Cu1-Cu2B, 2.402 Å; Cu2B-I2, 3.173 Å; Cu2B-I3, 2.711 Å; Cu2B-I4, 2.502 Å; Cu2B-Cu3, 2.651 Å; Cu3-I3, 2.681 Å; Cu3-I4, 2.691 Å; Cu3-I5, 2.605 Å; Cu3-N2, 2.198 Å. Bond lengths suggest Cu atoms possess a distorted tetrahedral coordination geometry. **MM4** molecular clusters are spatially organised in such a way to resemble

52

a double stranded linear structure (Fig. 2.13, bottom left). The packing of **MM8** inside the crystal evidences a pattern in which columns of clusters with the DABCO fragment alternatively pointing towards left and right are organised one next to the other: this disposition ensures an effective π-stacking between neighbouring naphthalenes, granting a more efficient and stable packing of the molecules in the crystal.
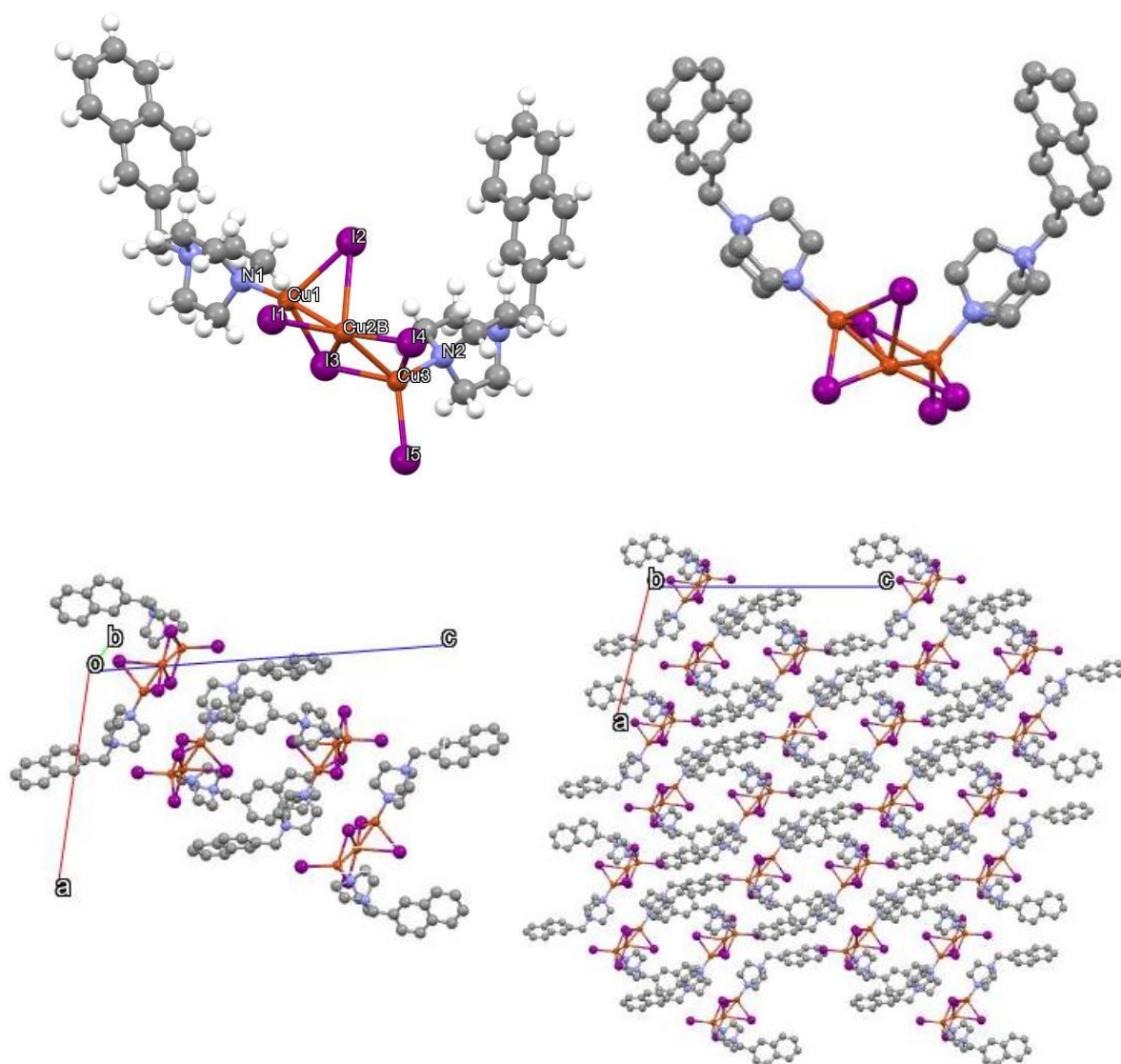
Figure 2.13 *Structural unit of 0D-Cu₃I₅(2-Nf-DABCO)₂ (**MM8**) with labelled atoms (top, left) along with its structural representation from a more comprehensive perspective (top, right). Structural and asymmetrical units coincide. Double stranded-like structure of **MM8** (bottom, left), together with the packing of the clusters inside the crystal along the b axis (bottom, right); hydrogens were omitted for a better visual clarity. Colour scheme: Cu, orange; I, purple; N, blue; C, grey; H, white.*

MM16 and **MM29** structure was solved and refined in the orthorhombic spatial group $P2_12_12_1$ (Fig. 2.14). More detailed information can be found in the crystallographic table reported in the *Appendix* section (Table A.5 and Table A.7, both present to confirm the same nature of the obtained products). The asymmetric unit contains one crystallographic independent molecule, alongside

with its cationic K^+ counterpart that ensures charge neutrality. The asymmetric unit suggests the CuI-based hybrid material having the stoichiometry [CuI$_3$(H-DABCO)]K. Bond lengths, going from left to right, are the following: Cu-I3, 2.661 Å; Cu-I2, 2.683 Å; Cu-N1, 2.118 Å; Cu-I1, 2.668 Å. Bond lengths suggest Cu atoms possess a distorted tetrahedral coordination geometry. The packing of **MM16** and **MM29** inside the crystal evidences a pattern in which inorganic modules are held together thanks to the ionic interaction between K^+ and I^- ions, with K atoms having a distorted octahedral coordination geometry and acting as centres of aggregation.
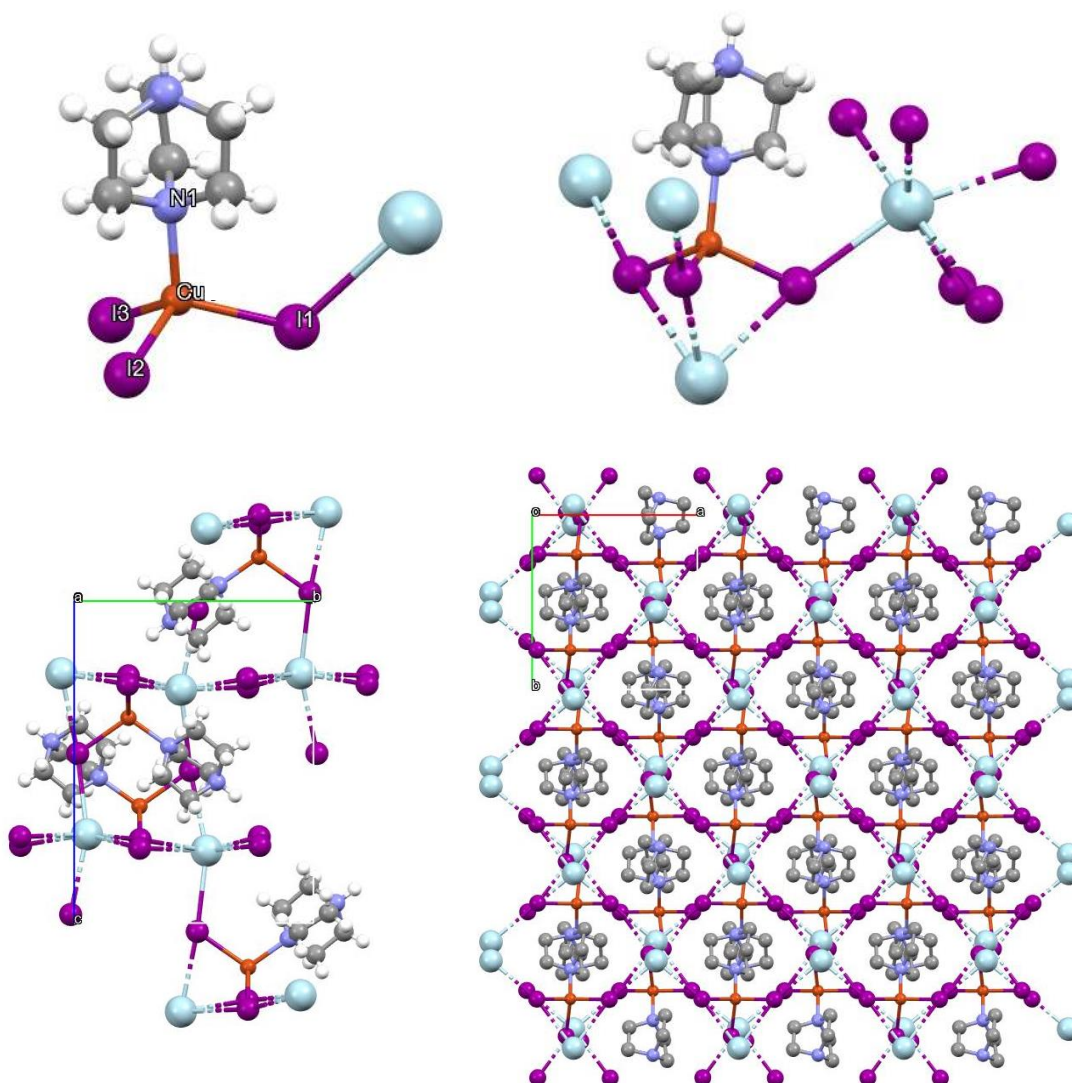
Figure 2.14 *Asymmetric unit of [CuI$_3$(H-DABCO)]K (**MM16, MM29**) with labelled atoms (top, left) along with its structural unit (top, right). Polymeric 1D linear chain-like structure of **MM16/MM29** (bottom, left), together with the packing of the structural units inside the crystal along the c axis in order to emphasise the role of K atoms as aggregation centres (bottom, right); hydrogens were omitted for a better visual clarity. Colour scheme: Cu, orange; I, purple; N, blue; C, grey; H, white.*

MM22 structure was solved and refined in the monoclinic spatial group P2$_1$/n (Fig. 2.15). More detailed information can be found in the crystallographic table reported in the *Appendix* section

(Table A.6). The asymmetric unit contains one crystallographic independent ionic pair. The asymmetric unit suggests the CuI-based hybrid material having the stoichiometry [meCaf][CuI$_2$]. Atoms in the structural unit generated by symmetry operations are indicated by the symbol "§" (Fig. 2.12, top left) and are, namely, going from left to right: I1§ (1-x, -y, 1-z), Cu1§ (1-x, -y, 1-z), I2§ (1-x, -y, 1-z). Bond lengths, going from left to right, are the following: Cu1§-I1§, 2.475 Å; Cu1§-I2, 2.606 Å; Cu1§-I2§, 2.554 Å; Cu1§-Cu1, 2.599 Å; Cu1-I2, 2.554 Å; Cu1-I2§, 2.606 Å; Cu1-I1, 2.475 Å. Bond lengths suggest Cu atoms possess a distorted planar trigonal coordination geometry. The packing of **MM22** inside the crystal evidences a pattern in which ionic pairs with the methylated caffeine molecules point alternatively left and right: this disposition grants more efficient electrostatic interaction between cationic and anionic modules in the crystal.
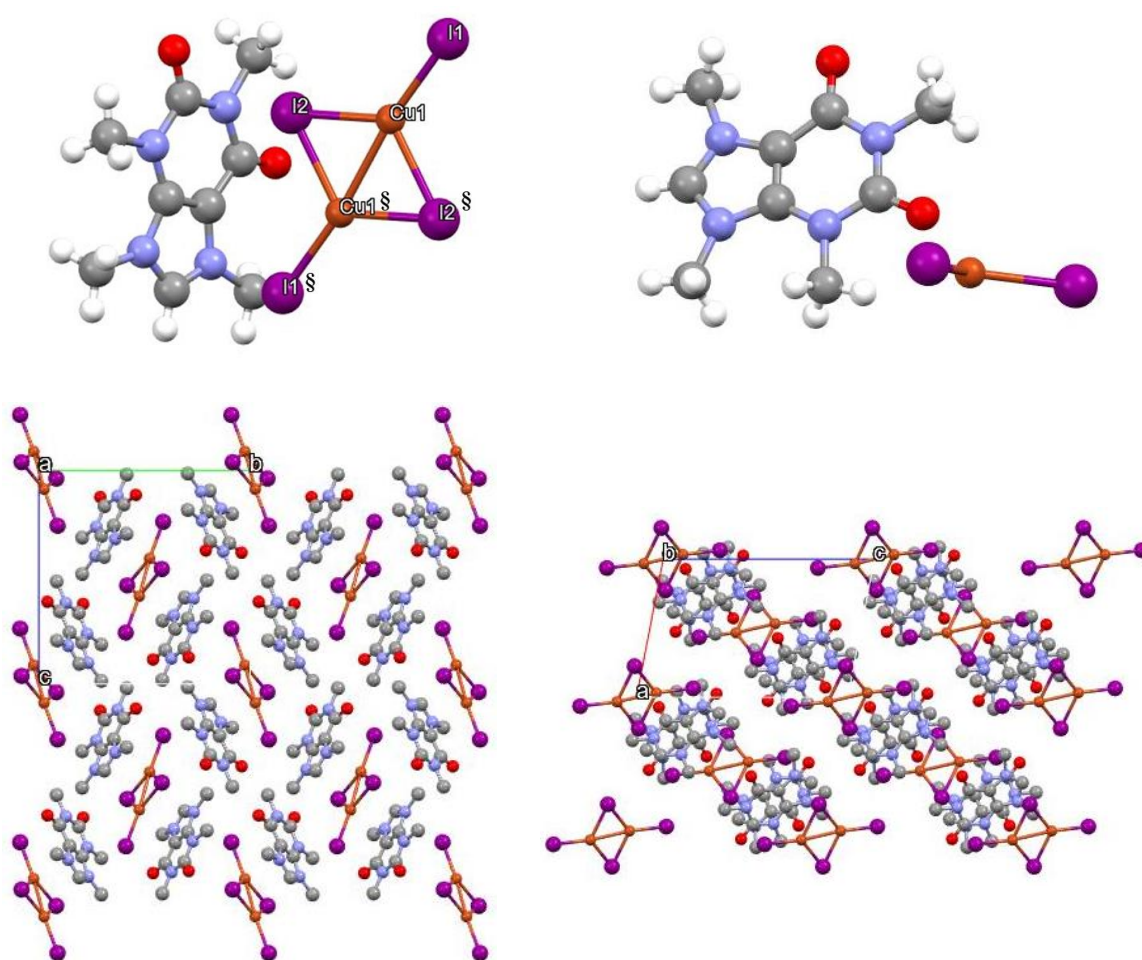
Figure 2.15 *Structural unit of [meCaf][CuI$_2$] (**MM22**) with labelled atoms (top, left) along with its asymmetric unit (top, right). Spatial disposition of **MM22** ion pairs inside the crystal along the a axis (bottom, left) and the b axis (bottom, right); hydrogens were omitted for a better visual clarity. Colour scheme: Cu, orange; I, purple; N, blue; C, grey; H, white.*

2.8. References

1. Fang, Y., Liu, W., Teat, S. J., Dey, G., Shen, Z., An, L., Yu, D., Wang, L., O'Carroll, D. M., Li, J. A Systematic Approach to Achieving High Performance Hybrid Lighting Phosphors with Excellent Thermal and Photostability. *Adv. Funct. Mater.* **27**, 1603444 (2017).

2. Liu, W., Fang, Y., Li, J. Copper Iodide Based Hybrid Phosphors for Energy-Efficient General Lighting Technologies. *Adv. Funct. Mater.* **28**, 1705593 (2018).

3. Hei, X & Li, J. All-in.one: a new approach towards robust and solution-processable copper halide hybrid semiconductors by integrating covalent, coordinate and ionic bonds in their structures. *Chem. Sci.* **12**, 3805-3817 (2021).

4. Liu, W., Zhu, K., Teat, S. J., Dey, G., Shen, Z., Wang, L., O'Carroll, D. M., Li, J. All-in-One: Achieving Robust, Strongly Luminescent and Highly Dispersible Hybrid Materials by Combining Ionic and Coordinate Bonds in Molecular Crystals. *J. Am. Chem. Soc.* **139**, 9281-9290 (2017).

5. Artem'ev, A. V., Davydova, M. P., Hei, X., Rakhmanova, M. I., Samsonenko, D. G., Bagryanskaya, I. Yu., Brylev, K. A., Fedin, V. P., Chen, J.-S., Cotlet, M., Li, J. Family of Robust and Strongly Luminescent CuI-Based Hybrid Networks Made of Ionic and Dative Bonds. *Chem. Mater.* **32**, 10708-10718 (2020).

6. Singh, G., Kaur, M., Kaur, H., Kang, T. S. Synthesis and complexation of a new caffeine based surface active ionic liquid with lysozyme in aqueous medium: Physicochemical, computational, and antimicrobical studies. *J. Mol. Liq.* **325**, 115156 (2021).

7. Raston, C. L., White, A. H. Crystal structure of the copper(I) iodide-pyridine (1/1) tetramer. *J. Chem. Soc., Dalton Trans.*, 2153-2156 (1976).

Chapter 3

Functional properties of AIO hybrid materials

This Chapter will focus on the study of the functional properties of the obtained AIO hybrid materials. Going more into detail, the present thesis work dealt with the analysis of MM4 photophysical properties, along with its application as a catalyst in the field of photodegradation of organic pollutants.

3.1.   AIO hybrid materials functional properties

As already mentioned in Chapter 1.5, AIO hybrid materials can provide a consistent number of different applications[1-4]. However, all the main application fields of these compounds revolve around their photophysical properties: thanks to their notable optical tunability, AIO hybrid species with the desired properties can be easily obtained, granting the possibility of their use even in really specific situations.

In the present work, the synthesised AIO hybrid compounds have been used for photoremediation application studies. Water pollution is one of the greatest environmental problems our society have to deal with, so the development of technologies for the degradation of water pollutants is urgently needed. The preference of CuI-based hybrid compounds over other materials resides in their low

toxicity, reliance on earth abundant elements, high stability, easy processability, and excellent IQYs: all these features make them a promising class of environmental-friendly photocatalysts.

The entire chapter will focus on the choice of an AIO compound as a model catalyst, its photophysical characterisation, and its interaction with two model organic dyes before and after light irradiation.

3.2. Photodegradation studies

After having taken into account the results of AIO hybrid materials synthesis, 1D-Cu$_2$I$_3$(Bz-HMTA) (**MM4**) was chosen for the role of model photocatalyst.

In order to use a lamp with the correct excitation wavelength, the UV-Vis absorption spectrum of MM4 powder has been measured (Fig. 5.1). MM4 showed an absorption maximum at a wavelength of 350 nm, so a 375 nm emitting LED was selected to perform the experiments.
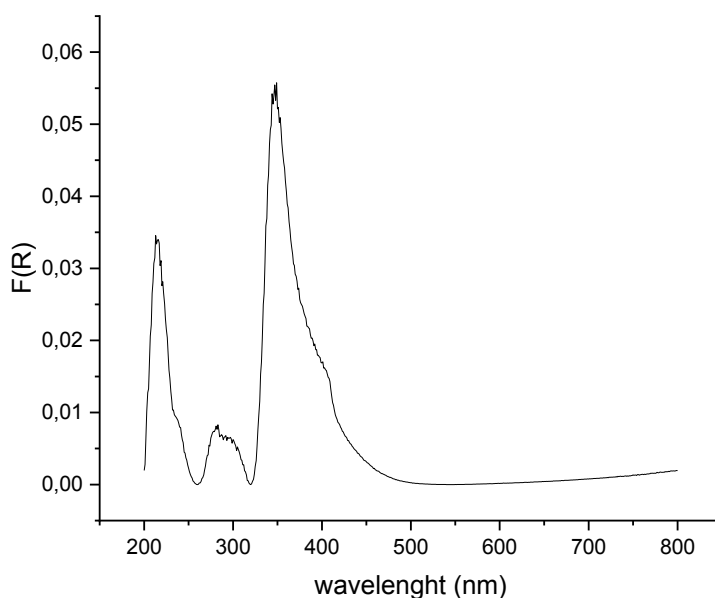

Figure 3.1 *1D-Cu$_2$I$_3$(Bz-HMTA)* *(**MM4**) UV-Vis absorption spectrum.*

On the other hand, the choice of organic molecules for the role of model pollutants fell on two well-known dyes: Rhodamine B (RhB) and Methylene Blue (MB) (Fig. 3.2).
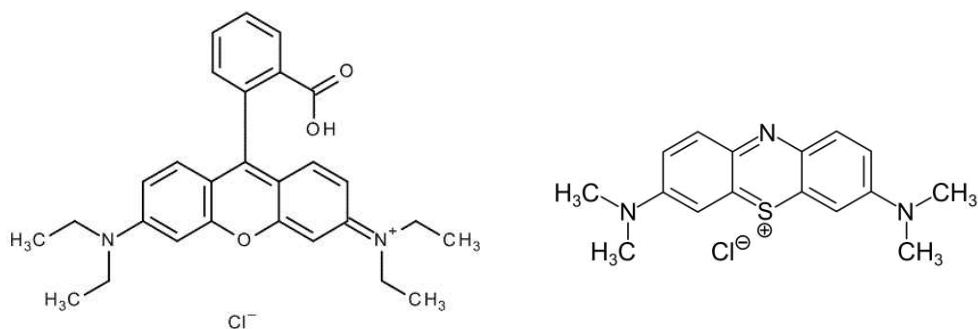
Figure 3.2 *Rhodamine B (RhB, left) and Methylene Blue (MB, right) molecular structure.*

UV-Vis spectra of those molecules showed an absorption maximum of 554 nm for RhB and of 663 nm for MB. The measurement range for the spectra were 400-700 nm for the former dye, 400-800 nm for the latter, thus ensuring minimum MM4 contribution for the experimental absorbance values.

3.2.1. Adsorption experiments

First of all, adsorption equilibria of RhB and MB on MM4 have been studied. The catalyst was finely grinded, then added to a solution of the selected dye: the mixture was sonicated to grant a more efficient powder dispersion. At this point, the beaker was covered with tinfoil, to ensure complete dark, and kept under magnetic stirring for 120 min. At given intervals, a small amount of solution was withdrawn from the mixture and absorbance spectra were measured.

- **RhB adsorption**

A plot of the normalised dye concentration percentage (i.e., $(C/C_0)\%$) over time recorded during the adsorption equilibrium between RhB and MM4 is reported in Fig. 3.3. After a rapid fall of the normalised concentration percentage in the first 10 min, the adsorption equilibrium was reached within 40 minutes from the beginning of the experiment; thereafter, a small oscillation of RhB concentration values was observed. So, MM4 effectively removes about 20-25% of the initial dye concentration simply by physical adsorption. Considering the results of the adsorption test, 40 minutes was the time chosen for the equilibration of the dye adsorption on the catalyst particles surface in the following experiments.
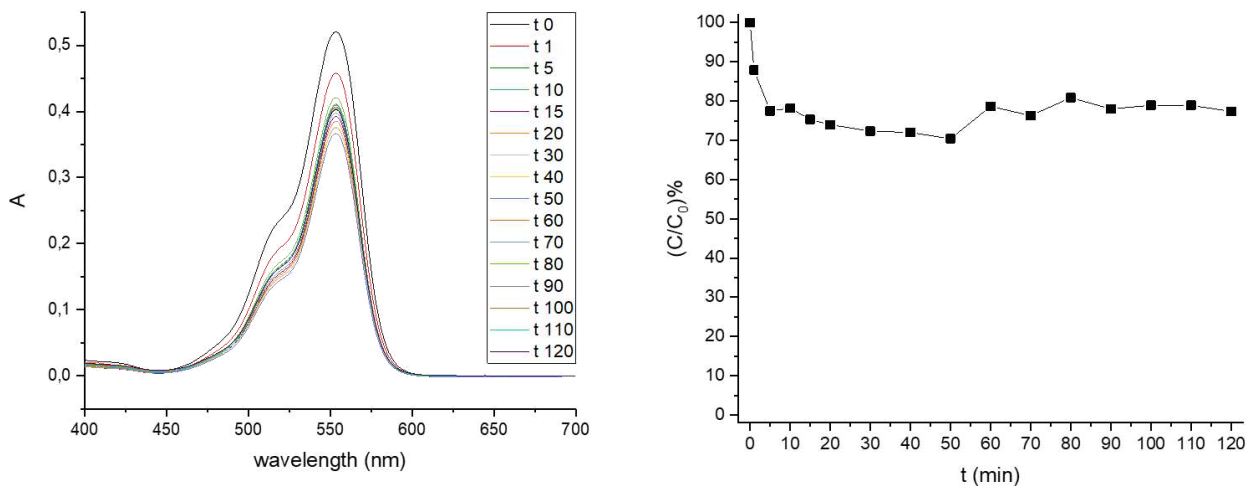
Figure 3.3 MM4-RhB adsorption test in the dark UV-Vis absorption spectra (left), alongside with the relative normalised
concentration percentage values over time (right).

- **MB adsorption**

A plot of the normalised dye concentration percentage (i.e., (C/C_0)%) over time recorded during
the adsorption equilibrium between MB and MM4 is displayed in Fig. 3.4. Results show an almost
complete adsorption of the dye on the catalyst surface (nearly 90% after 120 min). A second test
was performed to further confirm the notable adsorption tendency of MB on the AIO compound:
a coherent behaviour was observed between the two tests. Even if MB was nearly totally removed
from the solution by physical adsorption on MM4, a photodegradation experiment was still
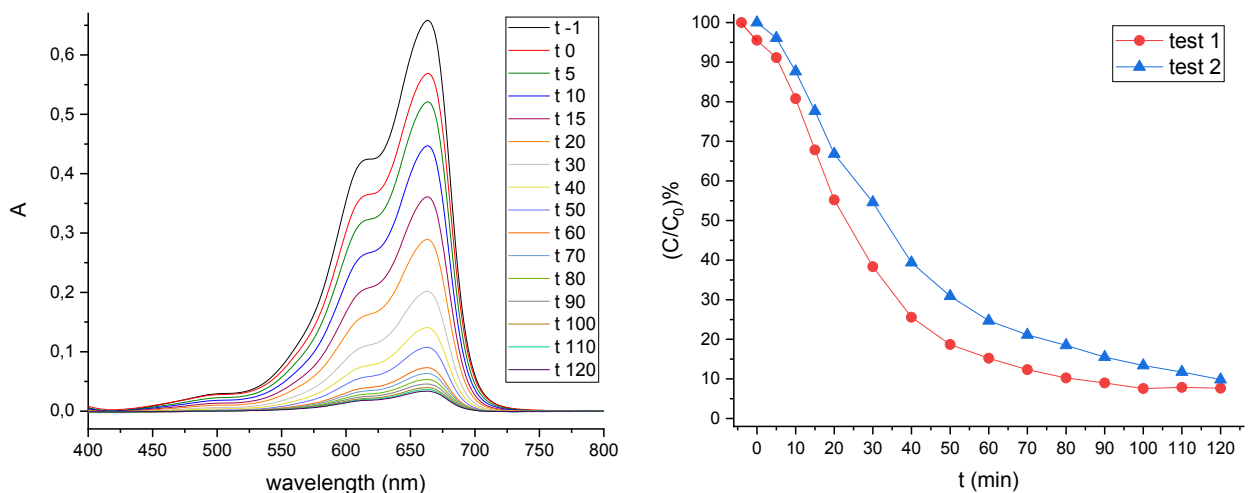performed.

Figure 3.3 MM4-MB adsorption test in the dark UV-Vis absorption spectra of test 1 (left), alongside with the relative normalised
concentration percentage values over time of test 1 and test 2 (right).

60

3.2.2. *Photodegradation experiments*

In order to evaluate the role of MM4 as an efficient photocatalyst, a prior photodegradation experiment of RhB and MB solutions without the AIO hybrid material was conducted. Then, MM4 was added into the dye solutions following the aforementioned protocol; after 40 minutes in the dark, the mixture was irradiated with a LED, and then 1 mL of the solution was withdrawn at given intervals to measure the photodegradation process. Photodegradation experiments setup are shown in Fig. 3.5.
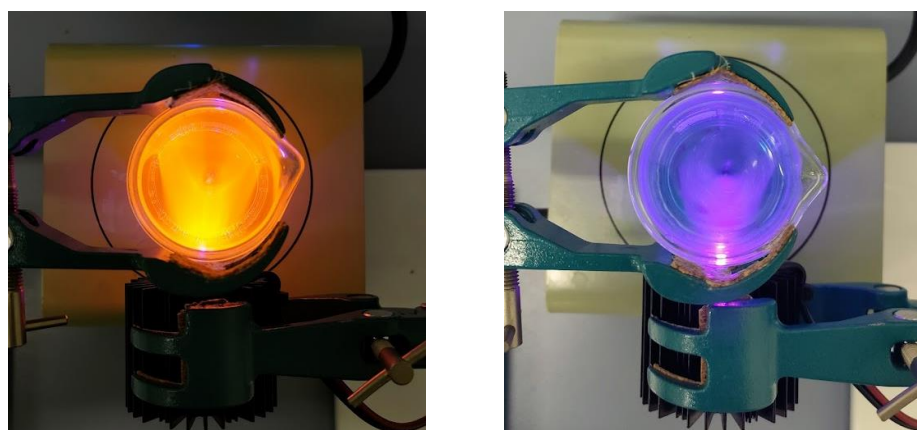

Figure 3.5 Experimental setup of the photodegradation experiment. Left: MM4-RhB solution. Right: MM4-MB solution.

- RhB photodegradation

Irradiation of RhB without catalyst showed a degradation of about 15% in 60 minutes(Fig. 3.6).
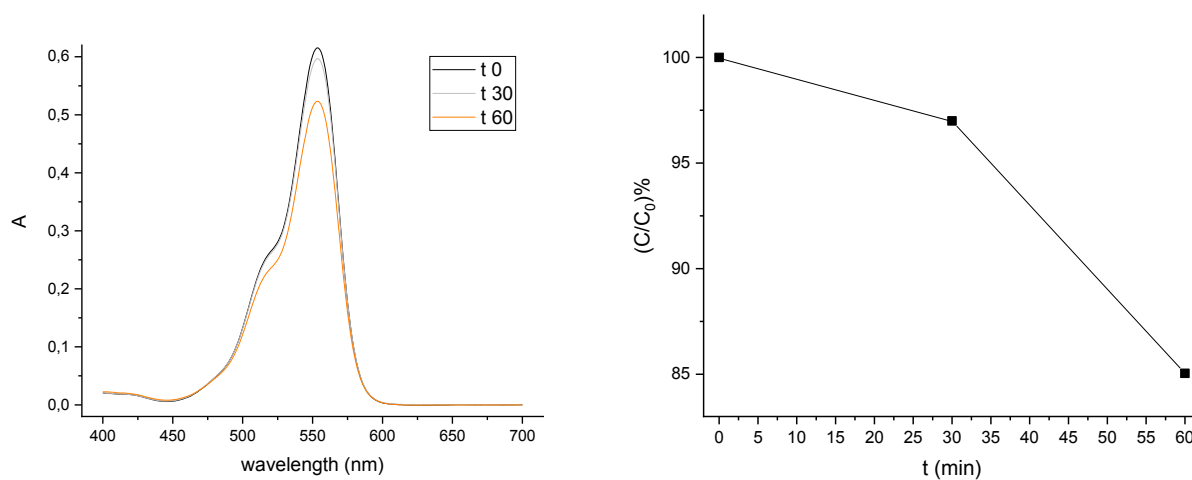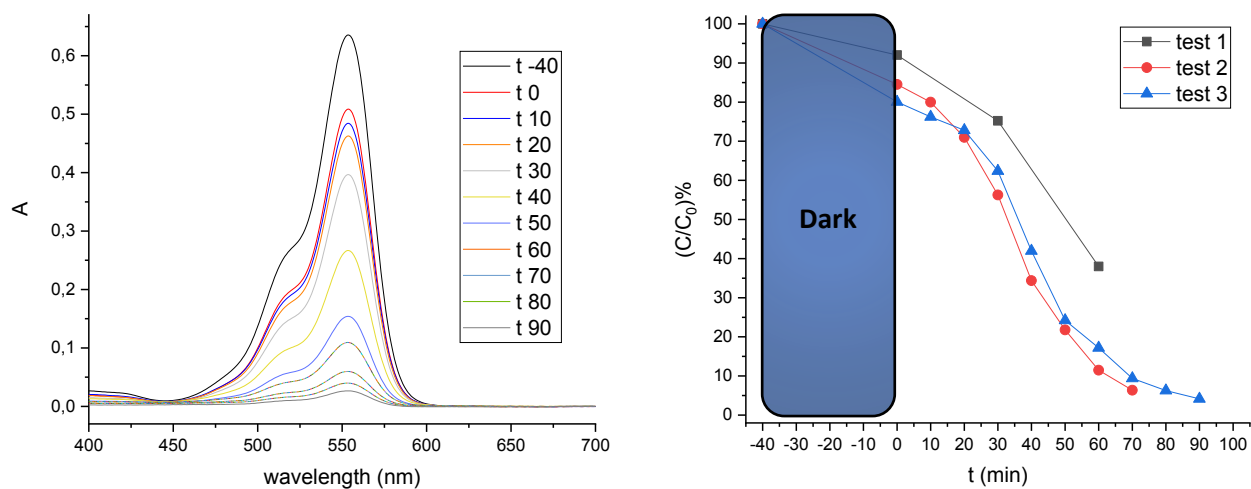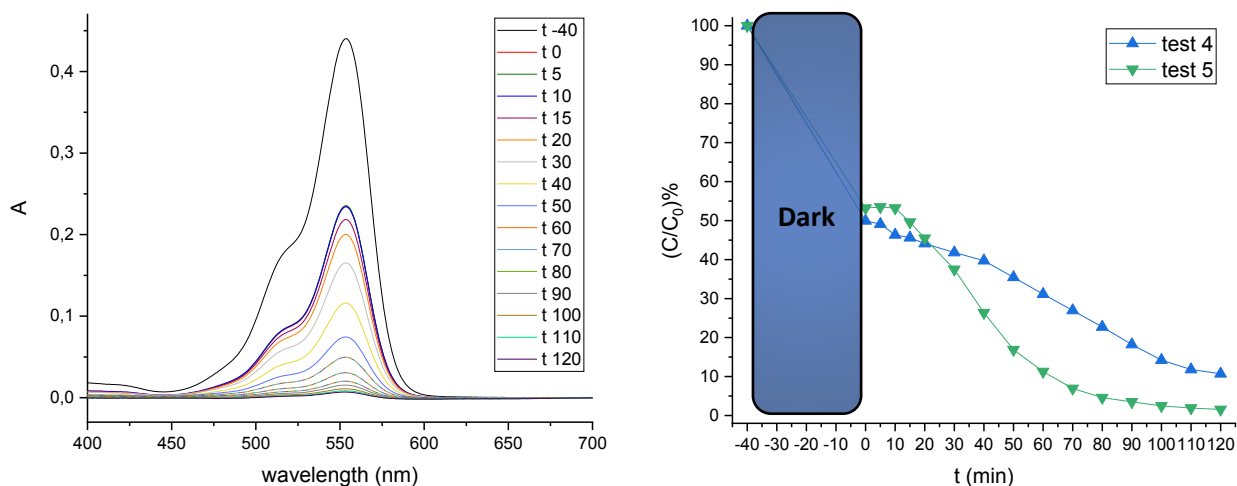

Figure 3.6 RhB photodegradation without MM4 UV-Vis absorption spectra over time (left), alongside with the relative normalised concentration percentage values over time (right).

Several photodegradation experiments were conducted with MM4. Three tests were performed with the catalyst first synthetic batch (Fig. 3.7). The irradiation time went from 60 minutes (test 1) to 90 minutes (test 3); test 1 degradation curve decades less steeply than those of test 2 and 3. The reason of this discrepancy lies on the LED alimentation value: in test 1, the LED was powered at a voltage of V = 3.6 V and a current intensity I = 0.5 A for the first 30 min, then at V = 3.6 V and I = 1.0 A until the end of the experiment; in test 2 and 3, the LED power supply was constantly kept at V = 3.6 V and I = 1.0 A. Moreover, in test 1 MM4 powder was neither grinded nor sonicated.

Two tests were instead performed with the catalyst second synthetic batch (Fig. 3.8). A remarkable difference appeared in the photodegradation curves: the adsorption value of this batch (~50%) is far higher than that of the first batch (~20%). The reason of such a diverse behaviour could be related to surface morphologic aspects: more accurate analyses of both batches powders are needed. Moreover, the different curves trend is related to the experimental setup. During the photodegradation tests, the LED was kept at a distance of about 4 cm in test 4, and at about 1 cm in test 5 (as in the case of test 1, 2, 3).


Figure 3.7 MM4-RhB 1ˢᵗ batch photodegradation UV-Vis absorption spectra of test 3 (left), alongside with the relative normalised concentration percentage values over time of test 1, test 2, and test 3 (right).

Figure 3.8 MM4-RhB 2nd batch photodegradation UV-Vis absorption spectra of test 5 (left), alongside with the relative normalised concentration percentage values over time of test 4, and test 5 (right).

A comparison between the two batches is possible taking into account test 3 and test 5, which underwent the same experimental setups: besides the initial disparity in adsorption value, in the long run the photodegradation curves overlap (Fig. 3.9).
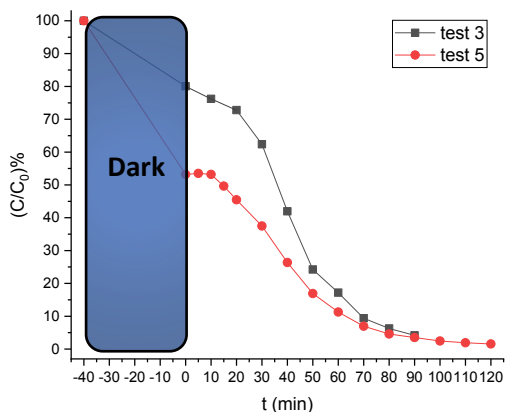
Figure 3.9 Confrontation between MM4-RhB relative normalised concentration percentage values over time of 1st batch (test 3) and 2nd batch (test 5).

After 120 minutes of light irradiation, about 5% of the starting RhB concentration was still in solution, thus indicating a very efficient photocatalytic activity of MM4. Fig. 3.10 evidences the difference in the RhB solution colour before and after the photodegradation experiment.

Figure 3.10 Cuvettes containing RhB solution without catalyst (left) and MM4-RhB solution at the end of the experiment (right).

- MB photodegradation

Irradiation of MB without catalyst showed a degradation of about 7% in 120 minutes (Fig. 3.6); without catalyst, the dye degradation is not very relevant.
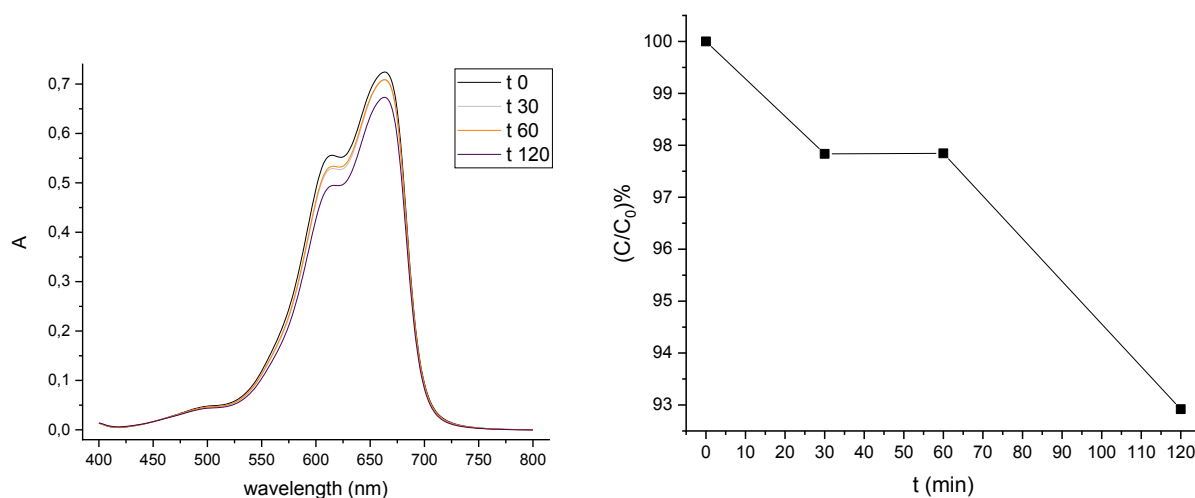
Figure 3.11 MB photodegradation without MM4 UV-Vis absorption spectra over time (left), alongside with the relative normalised concentration percentage values over time (right).

A photodegradation experiment with MM4 was performed even if the adsorption ratio of MB on the catalyst surface is extremely high. As expected, no photodegradation activity of MM4 on MB could be assessed. More accurate analyses of MM4-MB powders are needed.

Figure 3.12 MM4-MB photodegradation UV-Vis absorption spectra (left), alongside with the relative normalised concentration percentage values over time (right).

Even without evident photodegradation, an efficient physical removal of the dye from the solution still occurred: less than 5% of initial MB concentration remained in solution. Fig. 3.13 evidences the difference in the MB solution colour before and after the photodegradation experiment.

Figure 3.13 Cuvettes containing MB solution without catalyst (left) and MM4-MB solution at the end of the experiment (right).
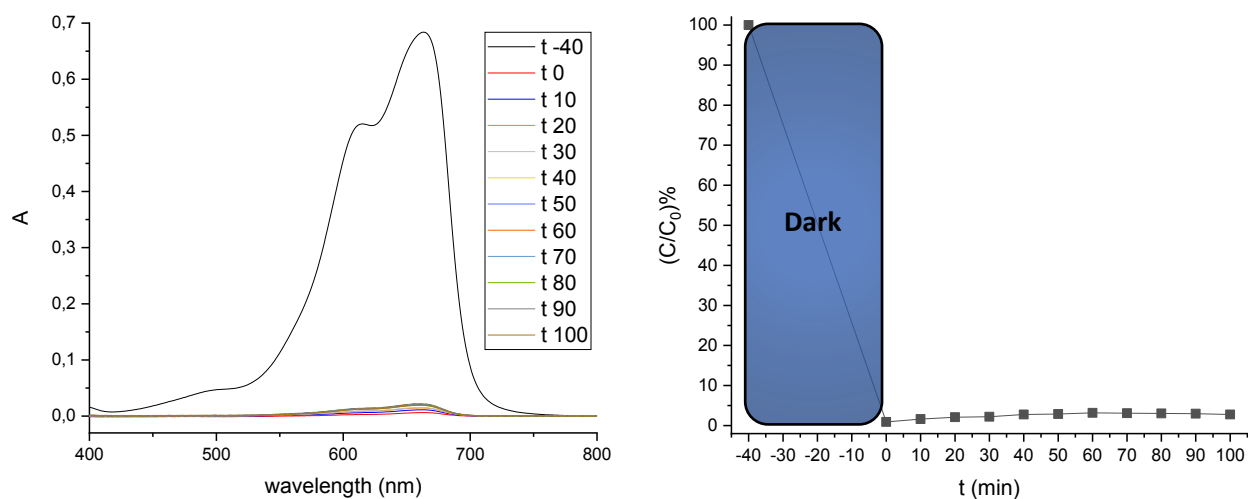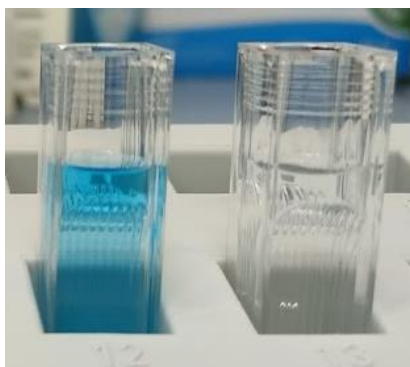
3.3. References

1. Liu, W., Fang, Y., Li, J. Copper Iodide Based Hybrid Phosphors for Energy-Efficient General Lighting Technologies. *Adv. Funct. Mater.* **28**, 1705593 (2018).

2. Hei, X & Li, J. All-in.one: a new approach towards robust and solution-processable copper halide hybrid semiconductors by integrating covalent, coordinate and ionic bonds in their structures. *Chem. Sci.* **12**, 3805-3817 (2021).

3. Wang, J.-J., Chen, C., Chen, W.-G., Yao, J.-S., Yang, J.-N., Wang, K.-H., Yin, Y.-C., Yao, M.-M., Feng, L.-Z., Ma, C., Fan, F.-J., Yao, H.-B. Highly Luminescent Copper Iodide Cluster Based Inks with Photoluminescence Quantum Efficiency Exceeding 98%. *J. Am. Chem. Soc.* **142**, 3686-3690 (2020).

4. Li, S.-L., Zhang, X.-M. Cu_3I_7 Trimer and Cu_4I_8 Tetramer Based Cuprous Iodide Polymorphs for Efficient Photocatalysis and Luminescent Sensing: Unveiling Possible Hierarchical Assembly Mechanism. *Inorg. Chem.* **53**, 8376-8383 (2014).

Chapter 4

Conclusions and perspectives

In this thesis work, a variety of new CuI-based hybrid materials has been synthesised and characterised, and their functional properties have been studied. Pyridine, caffeine, DABCO, and HMTA have been chosen as ligands in order to obtain at least one compound for each of the three classes of CuI hybrid materials. Functionalisation of those molecules via alkylation reaction have lead to the target ligands needed for the preparation of the target CuI-based hybrid compounds. Structural information about CuI hybrid species have been determined by XRD measurements. A variety of structural spatial groups, along with two different Cu atoms coordination geometry (distorted planar trigonal and most diffuse distorted tetrahedral) and crystal packing (given by ionic pairs, 0D clusters, and 1D linear polymeric chains), underlines how vast and peculiar this class of hybrid materials is. Depending on the choice of ligands and reaction conditions, other interactions can further stabilise CuI hybrid compound structures, ranging from π-stacking of aromatic rings to ordered disposition of inorganic modules around cationic centres of aggregation through electrostatic interactions. The preliminary luminescence properties of the obtained CuI-based hybrid materials have been assessed under UV lamp irradiation: three out of five hybrid species show no luminescence, while 0D-Cu_4I_6(me-DABCO)$_2$ possess an intense light blue luminesce under 254 UV light irradiation and 1D-Cu_2I_3(Bz-HMTA) displays an intense green luminescence at both 254 nm and 365 nm UV light irradiation.

1D-Cu_2I_3(Bz-HMTA) (MM4) has been then chosen as the model catalyst for photoremediation applications. Two organic dyes have been employed: Rhodamine B and Methylene Blue. MM4 was activated using a 375 nm LED close to its maximum absorption peak, UV-Vis spectra were registered over time intervals in order to monitor the photodegradation of the organic dyes. Data collected on MB shows an almost total dye adsorption on MM4 powder, thus indicating a very

efficient physical removal of the organic species from the solution. On the other hand, data obtained on RhB denote an excellent photodegradation activity of the AIO compound. At the end of the experiments, the residual concentration of both MB and RhB was less than 10% of its initial value. The interest towards multifunctional materials has continuously increased over the last few years. Materials capable of pollutant adsorption and degradation at the same time are highly desirable for environmental remediation strategies and these new AIO $Cu_xI_yL_n$ materials proved to be ideal candidates.

Future works will be oriented towards a more detailed study of luminescence properties and thermochromic behaviour of the obtained CuI-based hybrid materials. Moreover, non-successful synthesis will be studied more into detail to assess an efficient preparation strategy of the target AIO hybrid compounds. Finally, a morphological analysis of MM4 powder surface is needed to better understand both the different RhB adsorption value between 1st and 2nd synthetic batches and the diverse affinity of RhB and MB with the model photocatalyst.

Chapter 5

Experimental

Reagents were purchased from Merck and used as received.

Single crystal XRD data were collected using an Oxford Diffraction Gemini E diffractometer, equipped with a 2K × 2K EOS CCD area detector and sealed–tube Enhance (Mo) and (Cu) X–ray sources. A suitable single crystal has been sealed on the top of a nylon loop and measured at room temperature. Data have been collected by means of the ω-scans technique using graphite-monochromated radiation and Mo Kα (λ = 0.71073 Å) radiation or Cu Kα (λ = 1.54056 Å). The detector distance has been set at 45 mm. The diffraction intensities have been corrected for Lorentz/polarization effects as well as with respect to absorption. Empirical multi-scan absorption corrections using equivalent reflections have been performed with the scaling algorithm SCALE3 ABSPACK. Data reduction, finalization and cell refinement were carried out through the CrysAlisPro software. Accurate unit cell parameters were obtained by least squares refinement of the angular settings of strongest reflections, chosen from the whole experiment. The structures were solved with Olex2[2] by using ShelXT[3] structure solution program by Intrinsic Phasing and refined with the ShelXL[4] refinement package using least-squares minimization. In the last cycles of refinement, non-hydrogen atoms were refined anisotropically. Hydrogen atoms were included in calculated positions, and a riding model was used for their refinement.

Absorption spectra were recorded on a CARY5000 double-beam spectrophotometer in the 300-800 nm range, with a spectral bandwidth of 1 nm. The contribution due to the solvent was subtracted. Diffuse reflectance spectra in the range 250–800 nm were performed on a CARY5E spectrophotometer equipped with an internal diffuse reflectance accessory consisting of a poly(tetrafluoroethylene)-coated integration sphere. The spectra were acquired in reflectance mode

(R%) with a spectral band width of 4 nm and converted to absorbance by means of the Cary WinUV 3.00 software package.

5.1. Ligands synthesis

According to the targeted ligand, different synthetic procedures have been followed.

1-methyl-4-aza-1-azoniabicyclo[2.2.2]octane iodide ((me-DABCO)I) MM1L: 4-aza-1-azoniabicylo[2.2.2]octane (DABCO) (400.0 mg, 3.56 mmol) was mixed with EtOAc (5 mL) and cooled before use. The solution was colourless. Less than 1 equivalent of MeI (155.0 μL, 2.49 mmol) was added dropwise to the solution: an immediate formation of a white precipitate has been observed. The mixture was stirred at room temperature (r.t.) for 10 min. The thus formed precipitate was filtered, washed several times with petroleum ether (3 1 mL) and dried under reduced pressure at r.t. for 24 h to give 387.7 mg of (me-DABCO)I as a white solid. Yield: 61.2%.

^{1}H-NMR (300 MHz, CDCl$_3$, 22 °C): δ [ppm] = 3.69 (t, J = 7.62 Hz, 6 H, 3 CH$_2$), 3.40 (s, 3 H, CH$_3$), 3.24 (t, J = 7.62 Hz, 6 H, 3 CH$_2$). Solvent signal at 7.24 ppm.

N-benzylhexamethylenetetramine chloride ((Bz-HMTA)Cl)[1] MM3L: hexamethylenetetramine (HMTA) (1.6 g, 11.0 mmol) was dissolved in the CHCl$_3$ (5 mL): the resulting solution was colourless. An equimolar amount of benzyl chloride (Bz-Cl) (1.27 mL, 11.0 mmol) was added dropwise to the solution. The mixture was stirred at r.t. for 1 h. The resulting white precipitate was filtered, washed several times with chloroform (3 × 1 mL) and dried under reduced pressure at r.t. for 24 h to give 2.44 g of (Bz-HMTA)Cl as a white solid. Yield: 83.2%.

^{1}H-NMR (300 MHz, D$_2$O, 22 °C): δ [ppm] = 7.40 (m, 5 H, C$_6$H$_5$), 4.97 (s, 6 H, 3 CH$_2$), 4.57 (s, 6 H, 3 CH$_2$), 4.00 (s, 2 H, -CH$_2$-). Solvent signal at 4.68 ppm.

1-(2-methyl)naphtalene-4-aza-1-azoniabicyclo[2.2.2]octane bromide ((2-Nf-DABCO)Br) MM5L: DABCO (1.12 g, 10.0 mmol) and (2-bromomethyl)naphthalene (1.51 g, 6.8 mmol) were added to a 100 mL flask with CHCl$_3$ (17 mL). The colourless mixture was stirred at 70 °C for 16 h. After cooling to r.t., the solvent was removed under reduced pressure and give a white blocky solid. This white solid was washed with chloroform (3 × 5 mL) and dried under reduced pressure to give 1.42 g of (2-Nf-DABCO)Br as a white solid. Yield: 62.8%.

^{1}H-NMR (300 MHz, CDCl$_3$, 22 °C): δ [ppm] = 8.11 (s, 1 H, aromatic ring), 7.80 (m, 3 H, aromatic ring), 7.68 (m, 1 H, aromatic ring), 7.51 (m, 2 H, aromatic ring), 5.33 (s, 2 H, -CH$_2$-), 3.84 (t, J = 7.50 Hz, 6 H, 3 CH$_2$), 3.15 (t, J = 7.50 Hz, 6 H, 3 CH$_2$). Solvent signal at 7.26 ppm.

1-(1-methyl)naphtalene-4-aza-1-azoniabicyclo[2.2.2]octane chloride ((1-Nf-DABCO)Cl) MM6L: DABCO (1.12 g, 10.0 mmol) and (1-chloromethyl)naphthalene (1.24 g, 7.0 mmol) were added to a 100 mL flask with CHCl$_3$ (20 mL). The colourless mixture was stirred at 70 °C for 17 h. After cooling to r.t., the solvent was removed under reduced pressure and give a white blocky solid. This white solid was washed with chloroform (3 × 5 mL) and dried under reduced pressure to give 1.18 g of (1-Nf-DABCO)Cl as a white solid. Yield: 58.4%.

^{1}H-NMR (300 MHz, CD$_3$CN, 22 °C): δ [ppm] = 8.43 (m, 1 H, aromatic ring), 8.07 (m, 2 H, aromatic ring), 7.68 (m, 4 H, aromatic ring), 5.05 (s, 2 H, -CH$_2$-), 3.45 (t, J = 7.57 Hz, 6 H, 3 CH$_2$), 3.03 (t, J = 7.57 Hz, 6 H, 3 CH$_2$). Solvent signal at 1.94 ppm.

N-(2-methyl)naphtalenehexamethylenetetramine bromide ((2-Nf-HMTA)Br) MM10L: HMTA (845.7 mg, 6.0 mmol) and (2-bromomethyl)naphthalene (1.336 g, 6.0 mmol) were added to a 100 mL flask with CHCl$_3$ (20 mL). The colourless mixture was stirred at 70 °C for 45 min. After cooling to r.t., the solvent was removed under reduced pressure and give a white blocky solid. This white precipitate was washed with chloroform (3 × 5 mL) and dried under reduced pressure to give 1.64 g of (2-Nf-HMTA)Br as a white solid. Yield: 75.3%.

N-(1-methyl)naphtalenehexamethylenetetramine chloride ((1-Nf-HMTA)Cl) MM11L: HMTA (841.2 mg, 6.0 mmol) and (1-chloromethyl)naphthalene (1.065 g, 6.0 mmol) were added to a 100 mL flask with CHCl$_3$ (20 mL). The colourless mixture was stirred at 70 °C for 48 h. After cooling to r.t., the solvent was removed under reduced pressure and give a white blocky solid. This white precipitate was washed with chloroform (3 × 5 mL) and dried under reduced pressure to give 1.55 g of (1-Nf-HMTA)Cl as a white solid. Yield: 81.6%.

1-(4-methyl)pyridine-4-aza-1-azoniabicyclo[2.2.2]octane bromide ((mePy-DABCO)Br) MM14L: A pale yellow solution of 4-(bromomethyl)pyridine hydrobromide (253.7 mg, 1.0 mmol) in ethanol (EtOH) (20 mL) was neutralized with an aqueous solution of NaHCO$_3$ (1 equivalent). The salmon pink mixture was stirred at r.t. for 45 min. The solvent was evaporated under reduced pressure, the residue was dissolved in EtOH (30 mL), and the resulting red precipitate was filtered off. DABCO (112.3 mg, 1.0 mmol) was added to the filtrate. The solution turned from colourless to light violet. The reaction mixture was heated at 70 °C for 16 h, then the solvent was evaporated under reduced pressure. 187.1 mg of a salmon pink solid were obtained. NMR spectrum showed no reaction has occurred.

N-methylcaffeine iodide ((meCaf)I)[2] MM19L: The powder caffeine (Caf) (400.1 mg, 2.1 mmol) was taken in a 250 mL round bottom flask containing N,N-dimethylformamide (DMF) (25 mL) and was heated to 100 °C, followed by the addition of methyl iodide (meI) (0.64 mL, 10.3 mmol). The reaction mixture was stirred at 100 °C for 20 h. The solution turned from colourless to yellow after 5 min, and by the end of the reaction it became orange. The reaction mixture was then left to cool at r.t., and its colour turned back to yellow. An excess volume of ethyl acetate (EtOAc) (70 mL) was added to the solution to obtain light yellow precipitates. The flask was put in the freezer for one night to favour the precipitation of the solid product. The precipitates were washed three times with EtOAc (3 × 10 mL) to get pale yellow powder of (meCaf)I. The powder was dried under reduced pressure, and the desired product (359.6 mg) appeared as a yellowish-white solid. Yield: 50.9%.

^{1}H-NMR (300 MHz, D$_2$O, 22 °C): δ [ppm] = 4.17 (s, 3 H, CH$_3$), 4.11 (s, 3 H, CH$_3$), 3.79 (s, 3 H, CH$_3$), 3.35 (s, 3 H, CH$_3$), 3.16 (s, 1 H, H imidazole ring). Solvent signal at 4.79 ppm.

1-(1-methyl)pyrenyl-4-aza-1-azoniabicyclo[2.2.2]octane bromide ((mePyrn-DABCO)Br) MM24L: DABCO (84.2 mg, 0.75 mmol) was dissolved in CHCl$_3$ (3 mL), resulting in a colourless solution. (1-bromomethyl)pyrene (mePyrnBr) (149.9 mg, 0.51 mmol) were added to a 250 mL flask with CHCl$_3$ (80 mL): the solution was heated at 60 °C for 3h, turning from colourless to pale yellow. The solution of DABCO was added to the one containing mePyrnBr. The pale yellow mixture was stirred at 70 °C for 72 h. The reaction mixture appeared as a pale yellow suspension. After cooling to r.t., the reaction flask was put in the freezer for 72 h to favour the precipitation of the product; however, no changes have been observed. Then, the solvent was removed under reduced pressure and give 165.8 mg of (mePyrn-DABCO)Br in form of an olive green solid. NMR spectrum showed no reaction has occurred.

N-(1-methyl)pyrenylhexamethylenetetramine bromide ((mePyrn-HMTA)Br) MM26L: HMTA (35.7 mg, 0.25 mmol) was dissolved in CHCl$_3$ (5 mL), resulting in a colourless solution. (1-bromomethyl)pyrene (mePyrnBr) (149.8 mg, 0.51 mmol) were added to a 250 mL flask with CHCl$_3$ (80 mL): the solution was heated at 60 °C for 3h, turning from colourless to pale yellow. The solution of HMTA was added to the one containing mePyrnBr. The pale yellow mixture was stirred at 70 °C for 48 h. The reaction mixture appeared as a cloudy intense yellow suspension. After cooling to r.t., the reaction flask was left open for 48 h to favour the partial evaporation of the solvent and the precipitation of the product. The reaction mixture turned from intense yellow to pale yellow, and the formation of a pale yellow solid has been observed. Then, the solvent was

removed under reduced pressure and give 91.4 mg of (mePyrn-HMTA)Br in form of a yellow-orange solid. NMR spectrum showed no reaction has occurred.

1,4-diazabicyclo[2.2.2]octan-1-ium bromide ((H-DABCO)Br) MM28L: DABCO (336.6 mg, 3.0 mmol) was dissolved in EtOH (5 mL), resulting in a colourless solution. A solution of HBr (1.5 mL, 3.00 mmol) was added to the one containing DABCO. The reaction mixture was stirred at r.t. for 45 min. Then, the solvent was removed under reduced pressure and give 553.6 mg of (H-DABCO)Br as a white solid. Yield: 95.6%.

5.2. *Hybrid materials synthesis*

According to the desired physical phase of the products, two synthetic pathways have been followed: direct mixing of the inorganic and organic components for powder hybrid compounds; slow diffusion method for crystalline hybrid materials.

0D-Copper(I) iodide-pyridine tetramer (0D-Cu$_4$I$_4$(py)$_4$)[3] MM0: Copper(I) iodide (CuI) (191.1 mg, 1.0 mmol) was well dispersed in EtOH (20 mL) in a closed reaction vial. Excess pyridine (py) (326.0 μL, 4.0 mmol) was added directly in the reaction solution under magnetic stirring at r.t.. After 30 min, the precipitate was filtered out and washed three times with EtOH (3 × 5 mL). The white precipitate was then dried under reduced pressure to give 203.8 mg of Cu$_4$I$_4$(py)$_4$ as a white solid. Yield: 75.6%.

0D-Copper(I) iodide-1-methyl-4-aza-1-azoniabicyclo[2.2.2]octane molecular cluster (0D-Cu$_4$I$_6$(me-DABCO)$_2$) MM2: CuI (9.6 mg, 0.05 mmol) was first dissolved in KI saturated aqueous solution (1 mL) in a reaction vial. Acetonitrile (ACN) (1 mL) was added as another layer and then me-DABCO (12.8 mg, 0.05 mmol) in methanol (MeOH) (1 mL) was added slowly into the vial. The reaction mixture was kept undisturbed at r.t., and white single crystals formed in 1 day and were collected by filtration. Yield: 62.7%.

1D-Copper(I) iodide- N-benzylhexamethylenetetramine linear polymer (1D-Cu$_2$I$_3$(Bz-HMTA)):

Crystal compound MM4: CuI was first dissolved in KI saturated aqueous solution (1 mL) in a reaction vial. Acetonitrile (ACN) (1 mL) was added as another layer and then (Bz-HMTA)Cl in

methanol (MeOH) (1 mL) was added slowly into the vial. The reaction mixture was kept undisturbed at r.t., and white single crystals formed in 3 days and were collected by filtration.

Table7.1 shows the used quantities for the synthesis and the respective yields.

Table 5.1 *Amount of used reagents for the synthesis of MM4 and respective yields*

L:Cu ratio	Used L (mg)	Used Cu (mg)	Yield (%)
1:0.5	29.3 (0.11 mmol)	10.7 (0.056 mmol)	47.9
1:1	29.2 (0.11 mmol)	21.4 (0.11 mmol)	36.8
1:2	29.3 (0.11 mmol)	41.5 (0.22 mmol)	54.7
1:3	29.4 (0.11 mmol)	62.3 (0.33 mmol)	67.3
1:4	29.2 (0.11 mmol)	83.2 (0.44 mmol)	61.3
1:5	29.4 (0.11 mmol)	104.9 (0.55 mmol)	64.9

Powder compound MM7: CuI (190.9 mg, 1.0 mmol) was well dispersed in EtOH (20 mL) in a closed reaction vial. Excess (Bz-HMTA)Cl (1.07 g, 4.0 mmol) was added directly in the reaction solution under magnetic stirring at r.t.. After 1.5 h, the precipitate was filtered out and washed three times with EtOH (3 × 5 mL). The white precipitate was then dried under reduced pressure to give xx mg of Cu_2I_3(Bz-HMTA) as a white solid. Yield: 72.4%.

0D-Copper(I) iodide- 1-(2-methyl)naphtalene-4-aza-1-azoniabicyclo[2.2.2]octane molecular cluster (0D-Cu₃I₅(2-Nf-DABCO)₂) MM8: CuI was first dissolved in KI saturated aqueous solution (1 mL) in a reaction vial. ACN (1 mL) was added as another layer and then (2-Nf-DABCO)Br in MeOH (1 mL) was added slowly into the vial. The reaction mixture was kept undisturbed at r.t., and white single crystals formed in 4 days and were collected by filtration.

Table7.2 shows the used quantities for the synthesis and the respective yields.

L:Cu ratio	Used L (mg)	Used Cu (mg)	Yield (%)
5:1	92.1 (0.28 mmol)	10.45 (0.055 mmol)	65.3
1:1	18.7 (0.056 mmol)	20.6 (0.11 mmol)	-
1:5	18.7 (0.056 mmol)	52.6 (0.28 mmol)	42.1

No product formation has been observed in the 1:1 reaction vial.

0D-Copper(I) iodide- 1-(1-methyl)naphtalene-4-aza-1-azoniabicyclo[2.2.2]octane molecular cluster (0D-Cu$_x$I$_y$(1-Nf-DABCO)$_z$) MM9: CuI was first dissolved in KI saturated aqueous solution (1 mL) in a reaction vial. ACN (1 mL) was added as another layer and then (1-Nf-DABCO)Cl in MeOH (1 mL) was added slowly into the vial. The reaction mixture was kept undisturbed at r.t., and white single crystals formed in 5 days and were collected by filtration.

Table7.3 shows the used quantities for the synthesis.

L:Cu ratio	Used L (mg)	Used Cu (mg)	Yield (%)
5:1	159.0 (0.55 mmol)	21.5 (0.11 mmol)	-
1:1	34.0 (0.12 mmol)	21.0 (0.11 mmol)	-
1:5	33.0 (0.11 mmol)	104.1 (0.55 mmol)	-

No product formation has been observed in the 1:1 reaction vial. XRD analysis showed no product formation.

1D-Copper(I) iodide- N-(2-methyl)naphtalenehexamethylenetetramine linear polymer (1D-Cu$_x$I$_y$(2-Nf-HMTA)$_z$) MM12: CuI was first dissolved in KI saturated aqueous solution (1 mL) in a reaction vial. ACN (1 mL) was added as another layer and then (2-Nf-HMTA)Br in MeOH (1 mL) was added slowly into the vial. The reaction mixture was kept undisturbed at r.t., and white single crystals formed in 1 day and were collected by filtration.

Table7.4 shows the used quantities for the synthesis.

Table 5.4 Amount of used reagents for the synthesis of MM12 and respective yields

L:Cu ratio	Used L (mg)	Used Cu (mg)	Yield (%)
5:1	199.0 (0.55 mmol)	21.0 (0.11 mmol)	-
1:1	39.8 (0.11 mmol)	21.0 (0.11 mmol)	-
1:5	39.7 (0.11 mmol)	104.4 (0.55 mmol)	-

The first product formation has been observed in the 5:1 reaction vial after 12 h. The 5:1 reaction vial contained both the product and the unreacted ligand. The 1:5 reaction vial contained a considerable amount of unreacted CuI (red under UV lamp). XRD analysis showed no product formation.

1D-Copper(I) iodide- N-(1-methyl)naphtalenehexamethylenetetramine linear polymer (1D-Cu_xI_y(1-Nf-HMTA)$_z$):

MM13: CuI was first dissolved in KI saturated aqueous solution (1 mL) in a reaction vial. ACN (1 mL) was added as another layer and then (1-Nf-HMTA)Cl in MeOH (1 mL) was added slowly into the vial. The reaction mixture was kept undisturbed at r.t., and white single crystals formed in 1 day and were collected by filtration.

Table7.5 shows the used quantities for the synthesis.

Table 5.5 Amount of used reagents for the synthesis of MM13 and respective yields

L:Cu ratio	Used L (mg)	Used Cu (mg)	Yield (%)
5:1	58.3 (0.18 mmol)	7.1 (0.037 mmol)	-
1:1	34.8 (0.11 mmol)	21.0 (0.11 mmol)	-

The 1:5 ratio has not been prepared in order to avoid the contamination of the product due to the unreacted CuI. XRD analysis showed no product formation.

MM23: (1-Nf-HMTA)Cl (58.0 mg, 0.17 mmol) was first dissolved in water (1 mL) in a reaction vial. MeOH (1 mL) was added as another layer and then CuI (7.0 mg, 0.037 mmol) in ACN (1 mL) was added slowly into the vial. The reaction mixture was kept undisturbed at r.t.. A white cloudy suspension was formed in the MeOH interphase after few minutes. White single crystals formed in 2 days and were collected by filtration. XRD analysis showed no product formation.

0D-Copper(I) iodide- 1-(4-methyl)pyridine-4-aza-1-azoniabicyclo[2.2.2]octane molecular cluster (0D-Cu$_x$I$_y$(1-mePy-DABCO)$_z$)[8,9] MM16: CuI (7.0 mg, 0.037 mmol) was first dissolved in KI saturated aqueous solution (1 mL) in a reaction vial. ACN (1 mL) was added as another layer and then (1-mePy-DABCO)Br (31.5 mg, 0.11 mmol) in MeOH (1 mL) was added slowly into the vial. The L:Cu ratio was 3:1. The reaction mixture was kept undisturbed at r.t. for 7 days. Then, the vial was kept slightly opened to favour solvent concentration. White single crystals formed in 8 days and were collected by filtration. Yield: 43.5%.

N-methylcaffeine copper(I) iodide ([meCaf][CuI$_2$]) MM22: CuI (47.6 mg, 0.25 mmol) and (meCaf)I (83.4 mg, 0.25 mmol) were dissolved in ACN (15 mL), giving a pale yellow solution. The reaction mixture was stirred at 100 °C for 3.5 h. A white solid precipitated after a few minutes. At the end of the reaction, the solution had an intense yellow colour. The reaction mixture was left to cool at r.t. for 12 h. The precipitates were collected by filtration. Yield: 32.1%.

0D-Copper(I) iodide- 1-(1-methyl)pyrenyl-4-aza-1-azoniabicyclo[2.2.2]octane molecular cluster (0D-Cu$_x$I$_y$(mePyrn-DABCO)$_z$) MM25: (mePyrn-DABCO)Br (74.7 mg, 0.18 mmol) was first dissolved in CHCl$_3$ (2 mL) in a reaction vial. Dichloromethane (DCM) (2 mL) was added as another layer and then CuI (7.1 mg, 0.037 mmol) in ACN (2 mL) was added slowly into the vial. The L:Cu ratio was 5:1. A rapid formation of a white suspension was observed at the interphase. After 30 min, the interphase colour turned red. After 4 h, the reaction mixture was red at the bottom, and a good amount of a dark red precipitate had formed. The reaction mixture was kept undisturbed at r.t. for 6 days, and red crystals were collected by filtration. XRD analysis showed no product formation.

1D-Copper(I) iodide- N-(1-methyl)naphtalenehexamethylenetetramine linear polymer (1D-Cu$_x$I$_y$(mePyrn-HMTA)$_z$) MM27: (mePyrn-HMTA)Br (79.8 mg, 0.18 mmol) was first dissolved in CHCl$_3$ (3 mL) in a reaction vial and gave a dark yellow solution. DCM (2 mL) was added as another layer and then CuI (7.0 mg, 0.037 mmol) in ACN (2 mL) was added slowly into the vial. The L:Cu ratio was 5:1. After 5 min, a white precipitate was observed at the bottom of the vial. After 20 h, the reaction mixture was yellow, and a good quantity of white solid formed. The reaction

mixture was kept undisturbed at r.t. for 15 days, and white crystals were collected by filtration. XRD analysis showed no product formation.

0D-Copper(I) iodide- 1,4-diazabicyclo[2.2.2]octan-1-ium molecular cluster (0D-Cu$_x$I$_y$(H-DABCO)$_z$) MM29: CuI (9.6 mg, 0.05 mmol) was first dissolved in KI saturated aqueous solution (1 mL) in a reaction vial. ACN (1 mL) was added as another layer and then (H-DABCO)Br (48.3 mg, 0.25 mmol) in MeOH (1.5 mL) was added slowly into the vial. The L:Cu ratio was 5:1. The resulting mixture was colourless. After 15 min, the formation of a small amount of white precipitate was observed. The reaction mixture was kept undisturbed at r.t. for 3 days. The white single crystals were collected by filtration. Yield: 76.4%.

5.3. Photodegradation measurements setup

1D-Cu$_2$I$_3$(Bz-HMTA) **(**MM4**)** has been chosen as the model catalyst; Rhodamine B (RhB) and Methylene Blue (MB) were the two dyes selected as organic pollutants models in aqueous solution.

- **Adsorption experiments**

A beaker containing 40 mL of a 10^{-5} M solution of the selected dye was wrapped with tinfoil. A UV-Vis spectrum of the solution was measured. After that, 40 mg of MM4 were finely grinded for 30 s and then added to the previous solution. The obtained suspension was sonicated for 60 seconds and then magnetically stirred in the dark for 120 minutes: in order to verify that the adsorption equilibrium was reached, 1 mL of the suspension was taken at intervals (every 5 minutes in the first 20 minutes, then every 10 minutes) and analysed on a UV-Vis spectrophotometer.

- **Photodegradation experiments**

40 mg of finely grinded MM4 were added to 40 mL of a 10^{-5} M solution of RhB or MB. The suspension was sonicated for 60 seconds and then magnetically stirred in the dark for 40 minutes to ensure adsorption equilibrium and uniform dispersity. The solution was then exposed to UV irradiation from a LED lamp (M375D4), with the emission wavelength at 375 nm, kept at a distance of 1 cm from the beaker. The led was powered with a voltage of 3.6 V and a current of 1.0 A. After a given irradiation time (every 5 minutes in the first 20 minutes, then every 10 minutes), 1 mL of

the mixture was withdrawn, and the catalyst was separated from the suspensions. The filtrate was then analysed on a UV-Vis spectrophotometer in order to monitor the degradation process.

5.4. References

1. Minghu, W., Guichun, Y., Zuxing, C. Bis(1-Benzyl-3,5,7-Triaza-1-Azoniatricyclo[3.3.1.1^{3,7}] Decane) Peroxodisulfate: A Mild and Efficient Oxidation of Organic Compounds Under Anhydrous and Aprotic Conditions. *Synth. Comm.* **30** (17), 3127-3131 (2000).

2. Singh, G., Kaur, M., Kaur, H., Kang, T. S. Synthesis and complexation of a new caffeine based surface active ionic liquid with lysozyme in aqueous medium: Physicochemical, computational, and antimicrobical studies. *J. Mol. Liq.* **325**, 115156 (2021).

3. Fang, Y., Liu, W., Teat, S. J., Dey, G., Shen, Z., An, L., Yu, D., Wang, L., O'Carroll, D. M., Ling, J. A Systematic Approach to Achieving High Performance Hybrid Lighting Phosphors with Excellent Thermal- and Photostability. *Adv. Funct. Mater.* **27**, 1603444 (2017).

Appendix

- ## *Crystallographic tables*

  - ### Ligands

    - #### (2-Nf-DABCO)Br (MM5L)

Table A.1 Crystallographic table of MM5L.

Identification code	exp_276_auto
Empirical formula	$C_{51}H_{63}Br_3N_6$
Formula weight	999.80
Temperature/K	296.1(6)
Crystal system	orthorhombic
Space group	$Pca2_1$
a/Å	19.8174(6)
b/Å	20.0813(7)
c/Å	11.9073(3)
$\alpha/°$	90
$\beta/°$	90
$\gamma/°$	90
Volume/Å^3	4738.6(2)
Z	4
ρ_{calc}g/cm^3	1.401
μ/mm^{-1}	3.466
F(000)	2064.0
Crystal size/mm^3	$0.45 \times 0.21 \times 0.05$
Radiation	Cu Kα (λ = 1.54184)
2Θ range for data collection/°	8.806 to 130.176
Index ranges	$-23 \leq h \leq 23, -12 \leq k \leq 23, -14 \leq l \leq 13$
Reflections collected	20786
Independent reflections	6614 [R_{int} = 0.0595, R_{sigma} = 0.0478]
Data/restraints/parameters	6614/487/542
Goodness-of-fit on F^2	0.995
Final R indexes [I>=2σ (I)]	R_1 = 0.0601, wR_2 = 0.1901
Final R indexes [all data]	R_1 = 0.1157, wR_2 = 0.2629
Largest diff. peak/hole / e Å^{-3}	0.58/-0.57
Flack parameter	-0.04(3)

- **(1-Nf-HMTA)Cl (MM11L)**

Table A.2 Crystallographic table of MM11L.

Identification code	exp_298_auto
Empirical formula	$C_{17}H_{21}IN_4$
Formula weight	408.28
Temperature/K	297.20(14)
Crystal system	orthorhombic
Space group	$P2_12_12_1$
a/Å	6.4203(2)
b/Å	7.3818(2)
c/Å	34.7495(11)
α/°	90
β/°	90
γ/°	90
Volume/Å^3	1646.89(9)
Z	4
ρ_{calc}g/cm^3	1.647
μ/mm^{-1}	15.286
F(000)	816.0
Crystal size/mm^3	0.21 × 0.14 × 0.11
Radiation	Cu Kα (λ = 1.54184)
2Θ range for data collection/°	10.182 to 137.13
Index ranges	-7 ≤ h ≤ 7, -8 ≤ k ≤ 8, -41 ≤ l ≤ 41
Reflections collected	7887
Independent reflections	2785 [R_{int} = 0.0704, R_{sigma} = 0.0626]
Data/restraints/parameters	2785/189/188
Goodness-of-fit on F^2	1.070
Final R indexes [I>=2σ (I)]	R_1 = 0.0674, wR_2 = 0.1724
Final R indexes [all data]	R_1 = 0.0702, wR_2 = 0.1756
Largest diff. peak/hole / e Å^{-3}	2.32/-1.06
Flack parameter	0.22(2)

- CuI-based hybrid materials

- 1D-Cu$_2$I$_3$(Bz-HMTA) (MM4)

Table A.3 Crystallographic table of MM4.

Identification code	exp_264_auto
Empirical formula	C$_{15}$H$_{22}$Cu$_2$I$_3$N$_5$
Formula weight	780.15
Temperature/K	296.5(3)
Crystal system	triclinic
Space group	P-1
a/Å	8.9200(2)
b/Å	10.1896(3)
c/Å	12.8567(4)
α/°	99.517(2)
β/°	91.155(2)
γ/°	106.258(2)
Volume/Å^3	1103.66(6)
Z	2
ρ_{calc}g/cm^3	2.348
μ/mm^{-1}	6.131
F(000)	728.0
Crystal size/mm^3	? × ? × ?
Radiation	Mo Kα (λ = 0.71073)
2Θ range for data collection/°	7.23 to 52.744
Index ranges	-11 ≤ h ≤ 11, -12 ≤ k ≤ 12, -16 ≤ l ≤ 16
Reflections collected	8959
Independent reflections	4147 [R$_{int}$ = 0.0297, R$_{sigma}$ = 0.0421]
Data/restraints/parameters	4147/202/226
Goodness-of-fit on F^2	1.069
Final R indexes [I>=2σ (I)]	R$_1$ = 0.0329, wR$_2$ = 0.0766
Final R indexes [all data]	R$_1$ = 0.0401, wR$_2$ = 0.0818
Largest diff. peak/hole / e Å^{-3}	0.66/-1.19

- 0D-Cu$_3$I$_4$(2-Nf-DABCO)$_2$ (MM8)

Identification code	exp_285_auto
Empirical formula	C$_{34}$H$_{42}$Cu$_3$I$_5$N$_4$
Formula weight	1331.83
Temperature/K	296.1(3)
Crystal system	monoclinic
Space group	P2$_1$/n
a/Å	16.5414(8)
b/Å	10.0022(13)
c/Å	25.8920(7)
α/°	90
β/°	103.996(4)
γ/°	90
Volume/Å^3	4156.7(6)
Z	4
ρ_{calc}g/cm^3	2.128
μ/mm^{-1}	31.149
F(000)	2504.0
Crystal size/mm^3	0.34 × 0.09 × 0.05
Radiation	Cu Kα (λ = 1.54184)
2Θ range for data collection/°	7.218 to 137.3
Index ranges	-19 ≤ h ≤ 19, -11 ≤ k ≤ 6, -30 ≤ l ≤ 31
Reflections collected	19545
Independent reflections	7537 [R$_{int}$ = 0.0419, R$_{sigma}$ = 0.0465]
Data/restraints/parameters	7537/6/425
Goodness-of-fit on F^2	0.867
Final R indexes [I>=2σ (I)]	R$_1$ = 0.0511, wR$_2$ = 0.1381
Final R indexes [all data]	R$_1$ = 0.0618, wR$_2$ = 0.1524
Largest diff. peak/hole / e Å^{-3}	1.45/-0.91

- **[CuI₃(H-DABCO)]K   (MM16)**
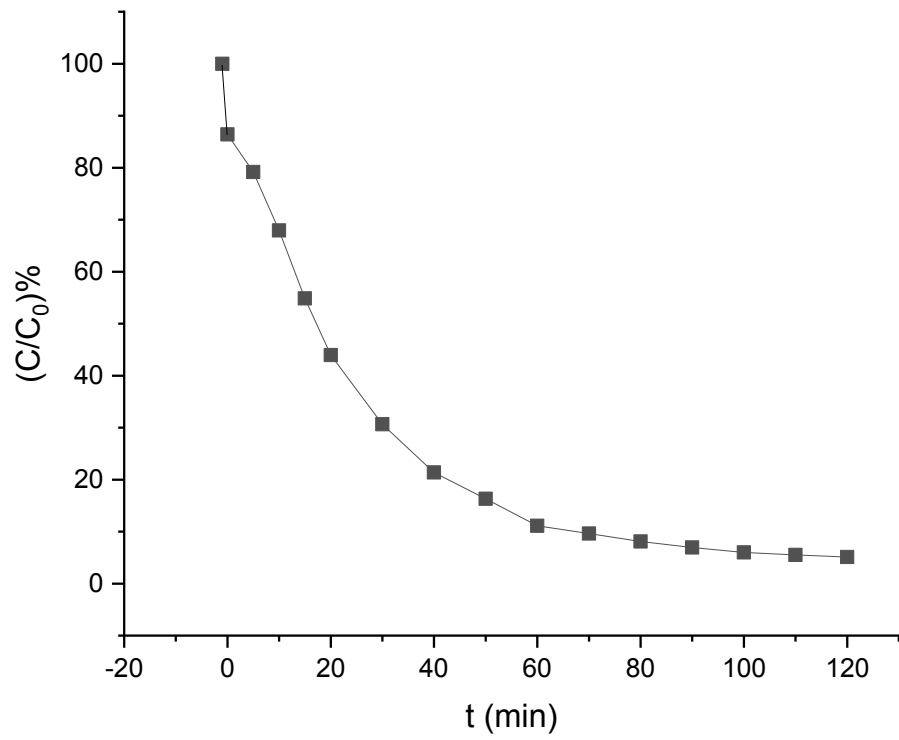
Table A.5 Crystallographic table of MM16.

Identification code	exp_346_auto
Empirical formula	$C_6H_{13}CuI_3KN_2$
Formula weight	596.52
Temperature/K	299.1(3)
Crystal system	orthorhombic
Space group	$P2_12_12_1$
a/Å	9.6743(2)
b/Å	10.2220(2)
c/Å	13.7802(3)
α/°	90
β/°	90
γ/°	90
Volume/Å³	1362.73(5)
Z	4
ρ_{calc}g/cm³	2.908
μ/mm⁻¹	58.079
F(000)	1080.0
Crystal size/mm³	0.12 × 0.05 × 0.01
Radiation	Cu Kα (λ = 1.54184)
2Θ range for data collection/°	10.776 to 136.85
Index ranges	-10 ≤ h ≤ 11, -10 ≤ k ≤ 12, -16 ≤ l ≤ 16
Reflections collected	3559
Independent reflections	2190 [R_{int} = 0.0472, R_{sigma} = 0.0592]
Data/restraints/parameters	2190/63/119
Goodness-of-fit on F^2	1.061
Final R indexes [I>=2σ (I)]	R_1 = 0.0752, wR_2 = 0.2020
Final R indexes [all data]	R_1 = 0.0764, wR_2 = 0.2051
Largest diff. peak/hole / e Å⁻³	3.64/-3.23
Flack parameter	0.29(3)

- **[meCaf][CuI₂]   (MM22)**

*Table A.6 Crystallographic table of **MM22**.*

Identification code	exp_414_auto
Empirical formula	$C_{18}H_{26}Cu_2I_4N_8O_4$
Formula weight	1053.15
Temperature/K	297.9(3)
Crystal system	monoclinic
Space group	$P2_1/n$
a/Å	8.8429(3)
b/Å	12.8436(4)
c/Å	13.2582(4)
α/°	90
β/°	100.949(3)
γ/°	90
Volume/Å³	1478.39(8)
Z	2
ρ_{calc}g/cm³	2.366
μ/mm⁻¹	5.653
F(000)	984.0
Crystal size/mm³	$0.25 \times 0.21 \times 0.18$
Radiation	Mo Kα (λ = 0.71073)
2Θ range for data collection/°	6.89 to 58.738
Index ranges	$-11 \leq h \leq 11, -17 \leq k \leq 17, -16 \leq l \leq 17$
Reflections collected	15055
Independent reflections	3503 [R_{int} = 0.0234, R_{sigma} = 0.0202]
Data/restraints/parameters	3503/0/167
Goodness-of-fit on F^2	1.064
Final R indexes [I>=2σ (I)]	R_1 = 0.0310, wR_2 = 0.0637
Final R indexes [all data]	R_1 = 0.0418, wR_2 = 0.0689
Largest diff. peak/hole / e Å⁻³	1.09/-1.20

− **[CuI₃(H-DABCO)]K (MM29)**

Table A.7 Crystallographic table of MM29.

Identification code	exp_485_auto
Empirical formula	$C_6H_{13}CuI_3KN_2$
Formula weight	596.52
Temperature/K	299(1)
Crystal system	orthorhombic
Space group	$P2_12_12_1$
a/Å	9.6630(4)
b/Å	10.1941(4)
c/Å	13.7522(6)
α/°	90
β/°	90
γ/°	90
Volume/Å³	1354.66(9)
Z	4
ρ_{calc}g/cm³	2.925
μ/mm⁻¹	8.721
F(000)	1080.0
Crystal size/mm³	0.12 × 0.11 × 0.1
Radiation	Mo Kα (λ = 0.71073)
2Θ range for data collection/°	7.148 to 58.56
Index ranges	-12 ≤ h ≤ 10, -12 ≤ k ≤ 8, -17 ≤ l ≤ 18
Reflections collected	8875
Independent reflections	3161 [R_{int} = 0.0236, R_{sigma} = 0.0275]
Data/restraints/parameters	3161/0/118
Goodness-of-fit on F^2	0.969
Final R indexes [I>=2σ (I)]	R_1 = 0.0194, wR_2 = 0.0403
Final R indexes [all data]	R_1 = 0.0210, wR_2 = 0.0409
Largest diff. peak/hole / e Å⁻³	0.44/-0.87
Flack parameter	-0.018(19)

- ## *UV-Vis spectra*
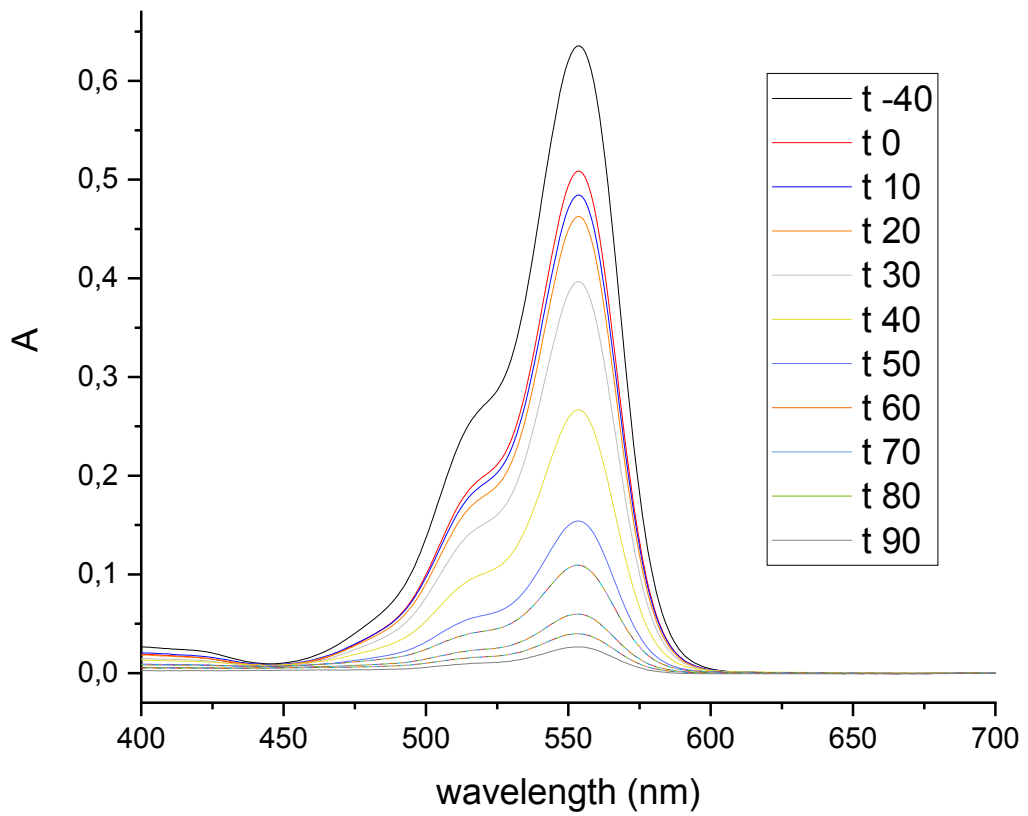
  - **MM4-RhB adsorption kinetics**
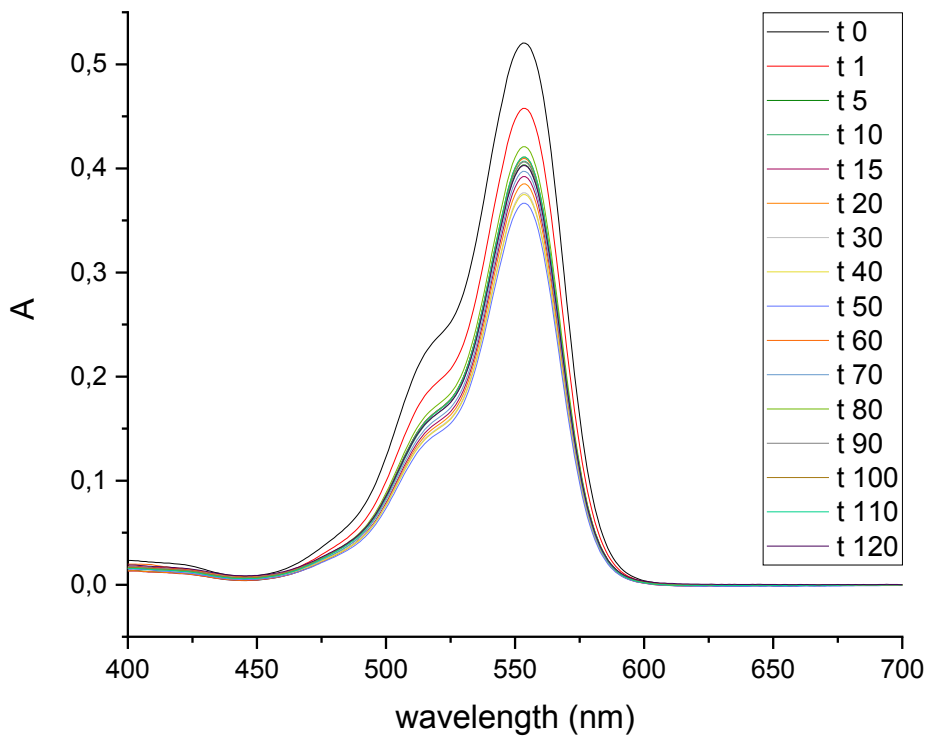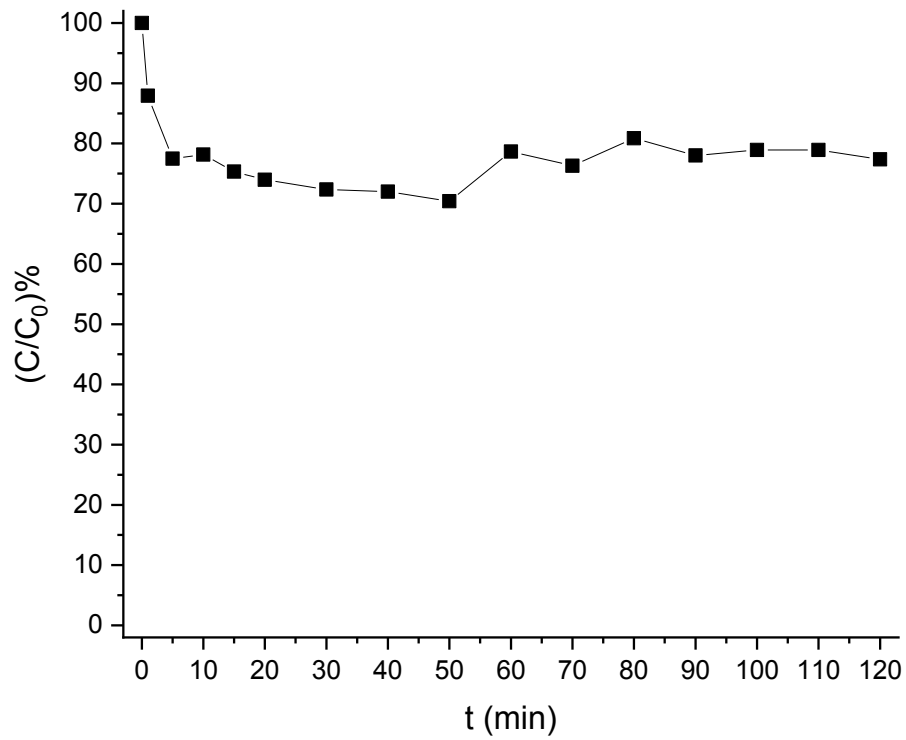
- **MM4-MB adsorption kinetics, test 1**
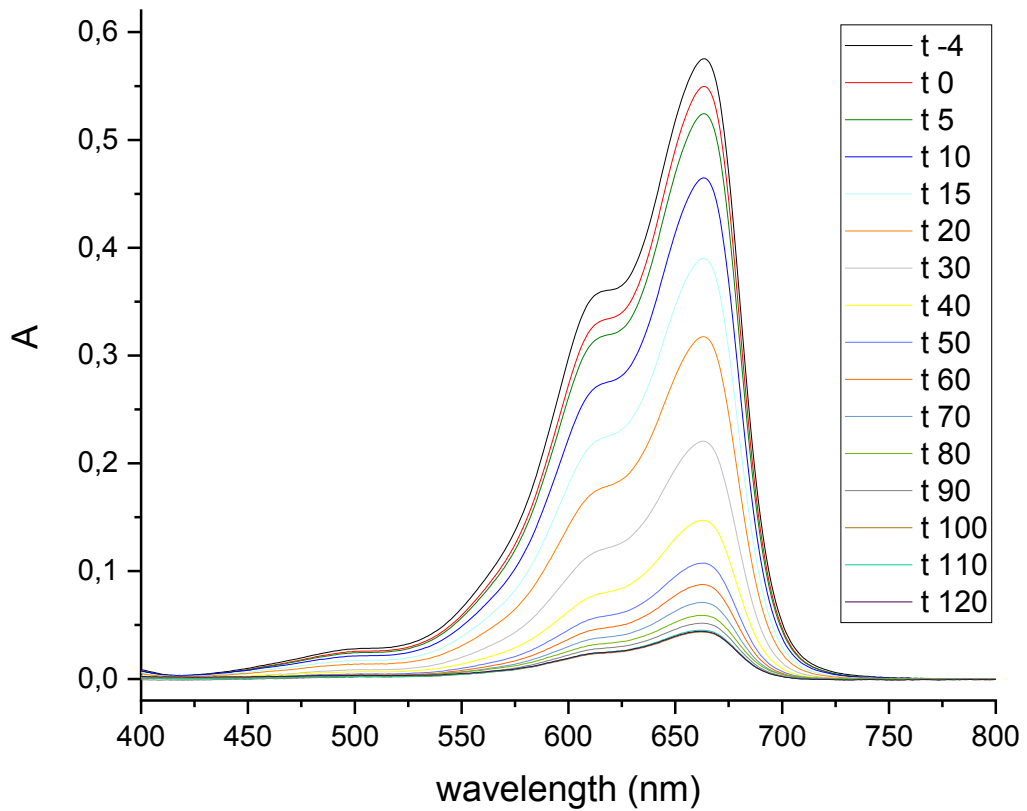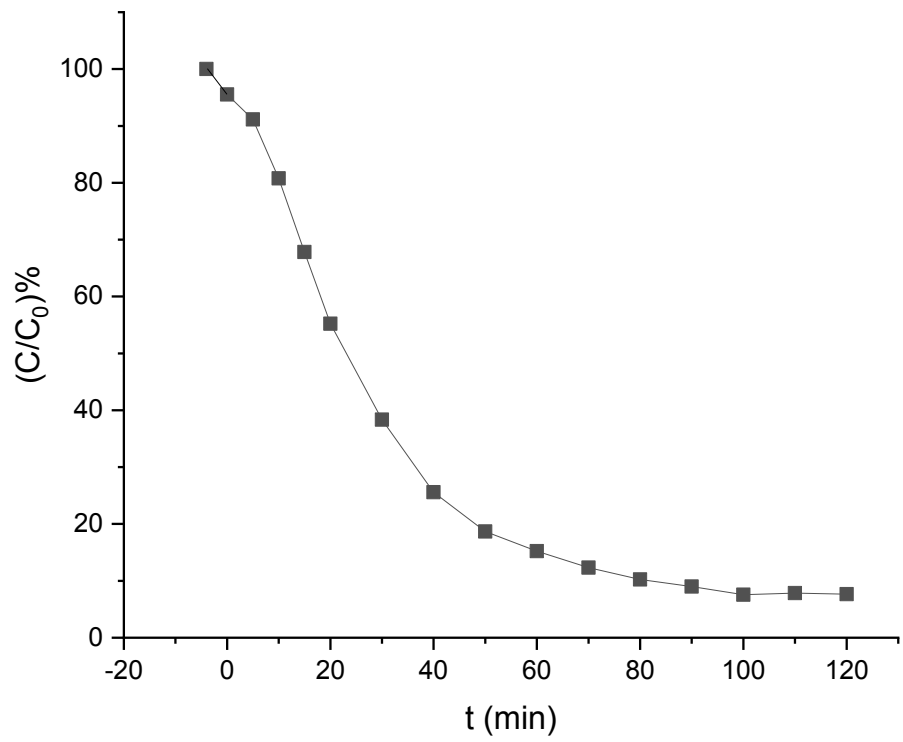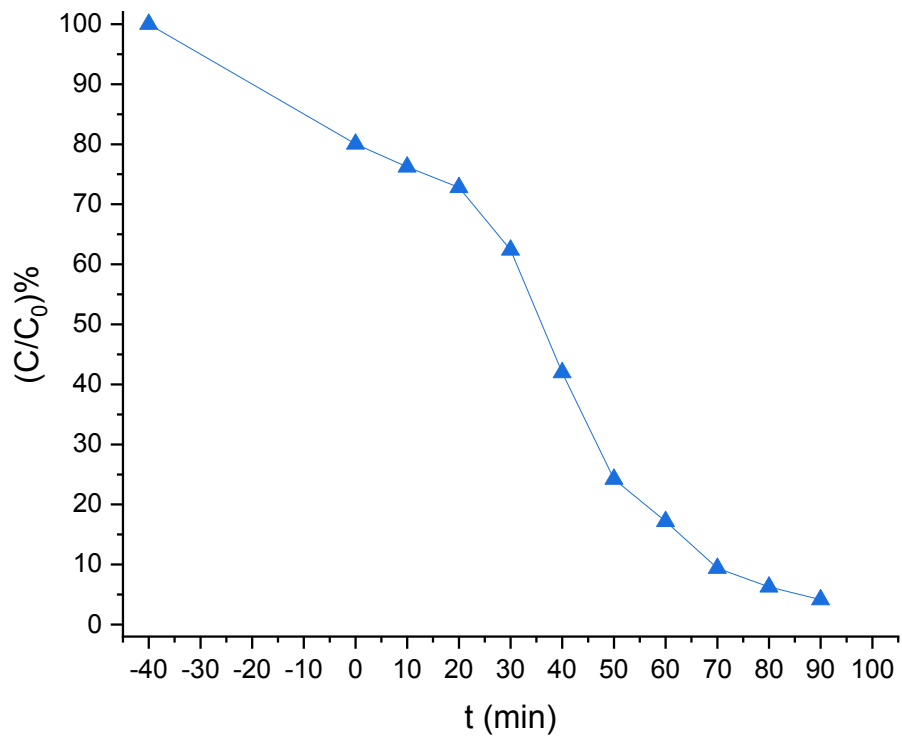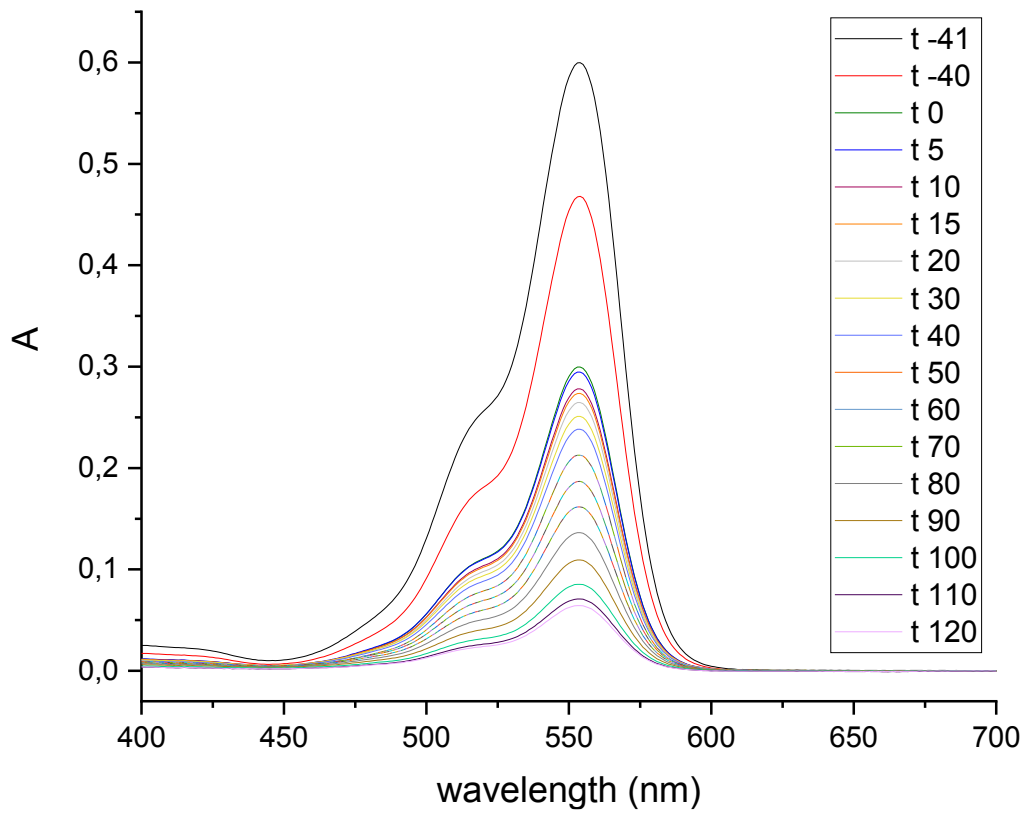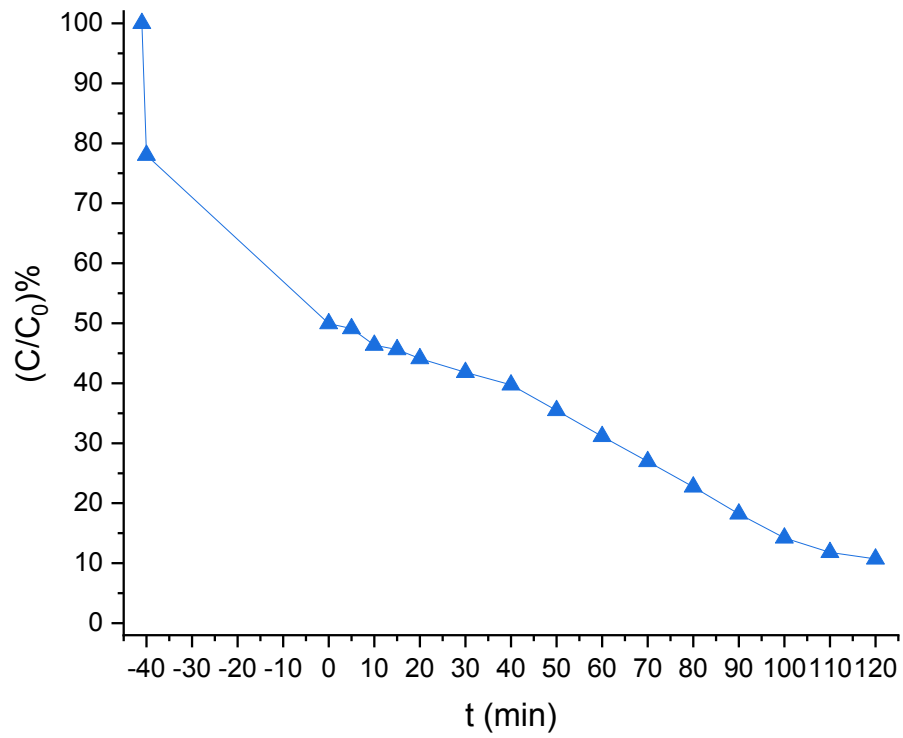
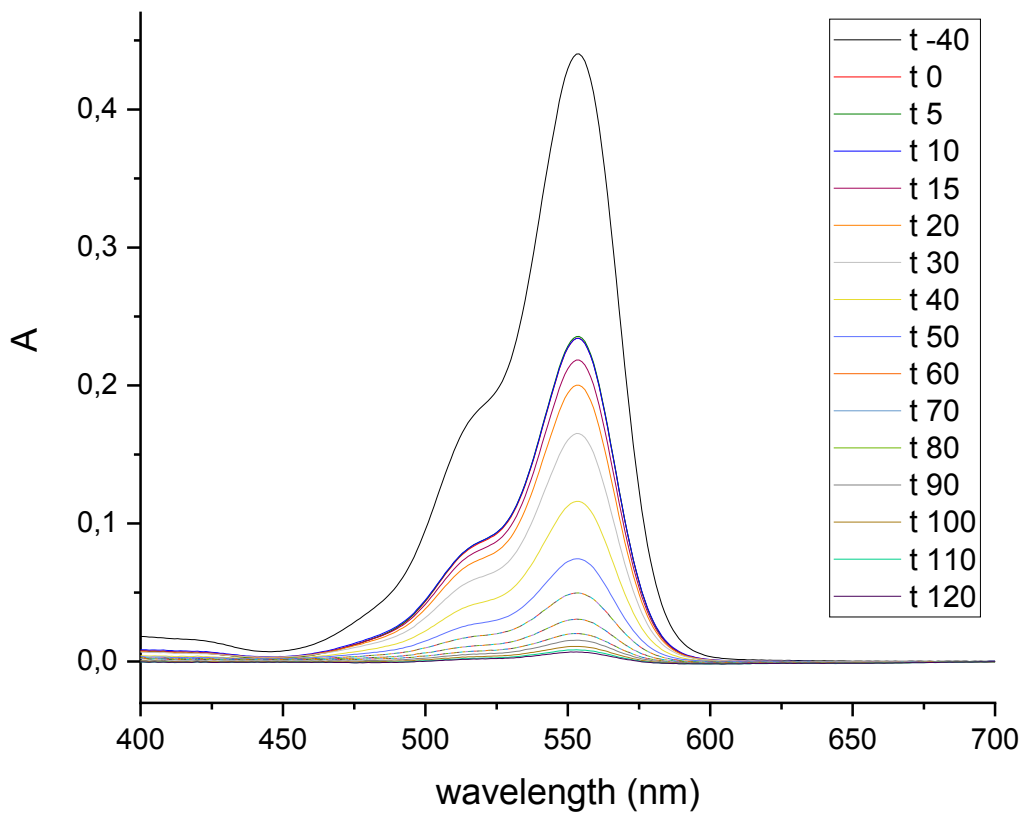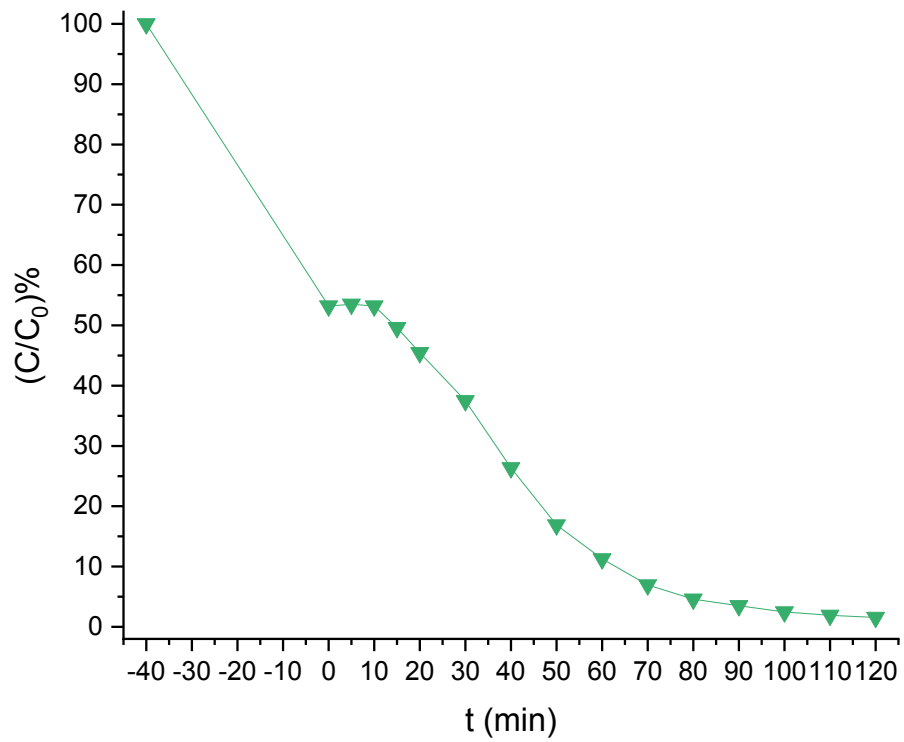- **MM4-RhB photodegradation kinetics, test 1 (1st batch)**
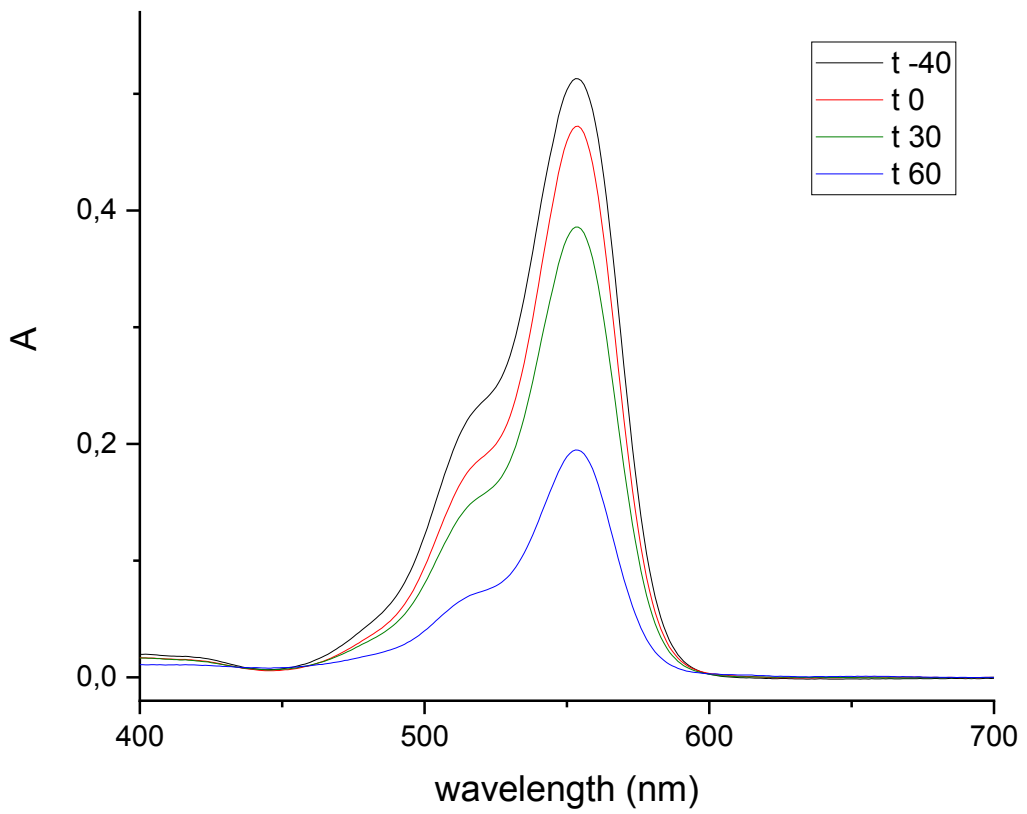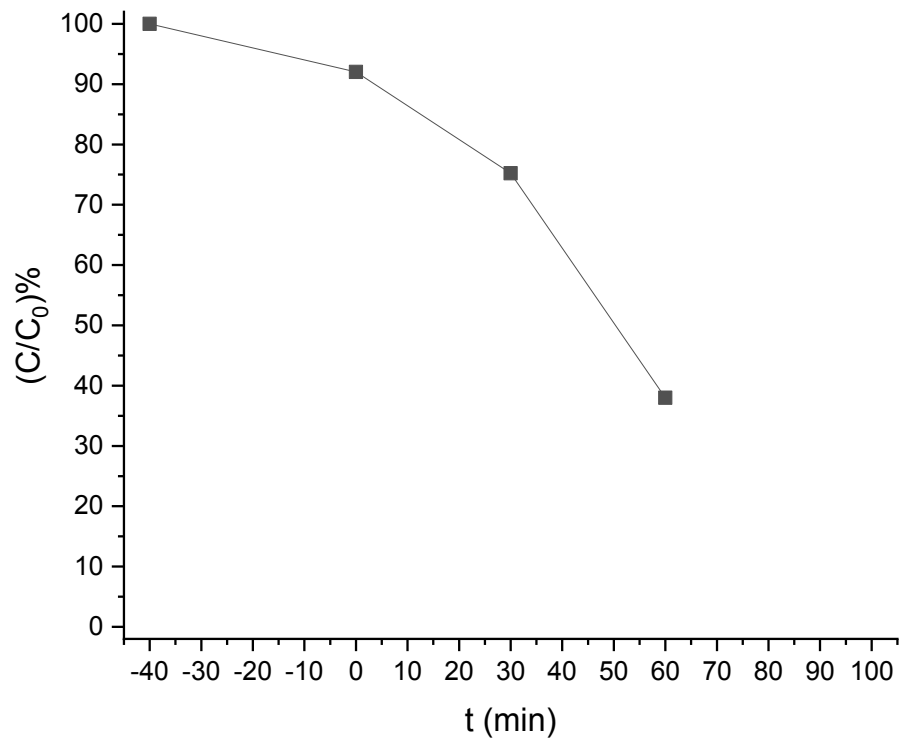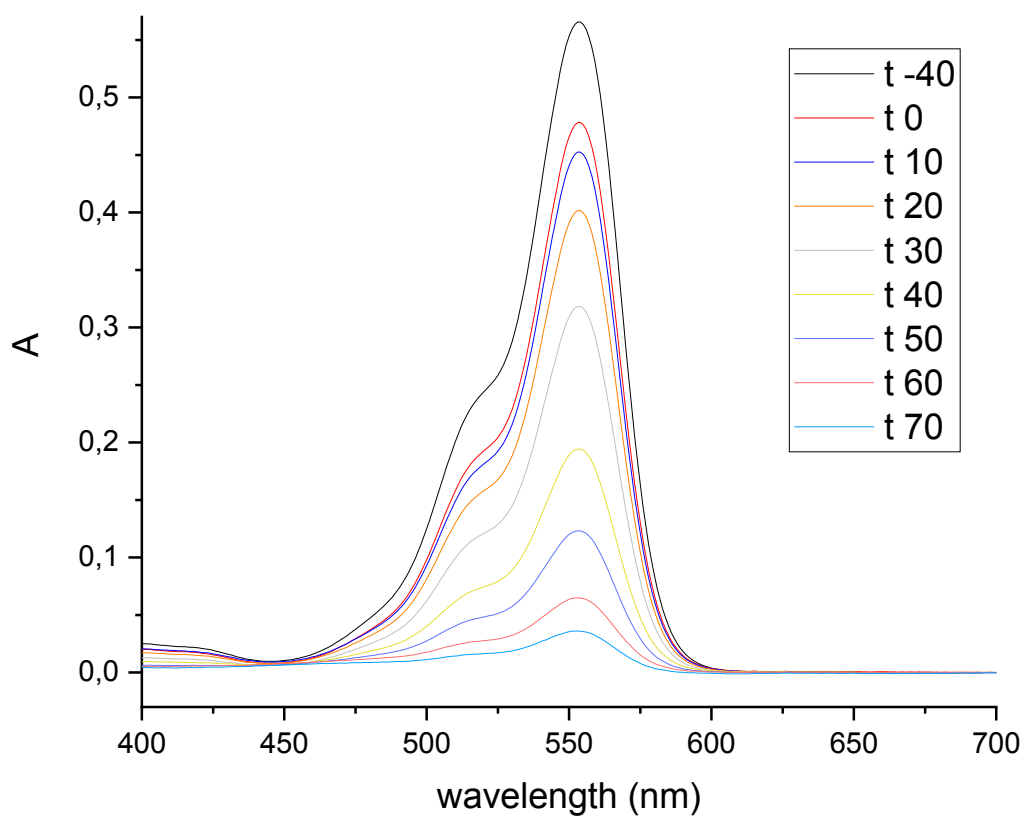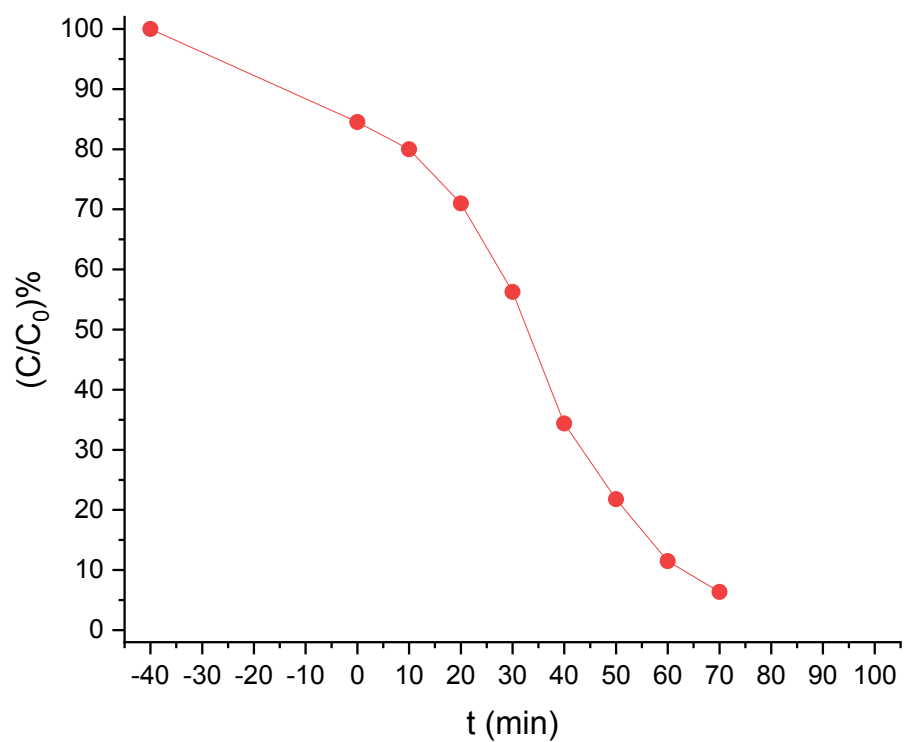
– **MM4-RhB photodegradation kinetics, test 3 (1st batch)**

– **MM4-RhB photodegradation kinetics, test 5 (2nd batch)**

- **MM4-MB photodegradation kinetics**